# Preparation of protein-based bionanocomposites and evaluation of their physico-chemical properties

*A Thesis submitted for the award of degree of*

**Doctor of Philosophy**

*Submitted by:*

**Shreya Sharma**
(Registration no. 901909033)

THAPAR INSTITUTE
OF ENGINEERING & TECHNOLOGY
(Deemed to be University)

*Under the supervision of*

**Dr. Bonamali Pal**
**Professor**
**DCBC**

**Dr. Niranjan Das**
**Professor**
**DBT**

**Department of Chemistry and Biochemistry**
**Thapar Institute of Engineering and Technology**
**Patiala-147004, India**

**June, 2026**

# Certificate

This is to certify that the work incorporated in this thesis entitled **"Preparation of protein-based bionanocomposites and evaluation of their physico-chemical properties"**, submitted by Shreya Sharma to the Department of Chemistry and Biochemistry, Thapar Institute of Engineering and Technology, Patiala, in fulfilment of the requirements for the award of the Degree of Doctor of Philosophy, embodies the authentic research work carried out by the candidate under my supervision and guidance. We certify that this work is original and has not been submitted to any other University or Institution in part or whole for the award of any degree or diploma.

**Dr. Bonamali Pal**
(Professor and Supervisor)
Department of Chemistry and Biochemistry

**Dr. Niranjan Das**
(Professor and Supervisor)
Department of Biotechnology

**Dr. Manmohan Chhibber**
(Professor and Head)
Department of Chemistry and Biochemistry

# Candidate's Declaration

I, hereby declare that the work presented in the thesis entitled **"Preparation of protein-based bionanocomposites and evaluation of their physico-chemical properties"**, in fulfilment of the requirement for the award of the Degree of Doctor of Philosophy, submitted to the Department of Chemistry and Biochemistry, Thapar Institute of Engineering and Technology, Patiala is an authentic record of my work carried out under the supervision of Dr. Bonamali Pal (Professor and Former Head, Department of Chemistry and Biochemistry, Thapar Institute of Engineering and Technology, Patiala, India) and Dr. Niranjan Das (Professor, Department of Biotechnology, Thapar Institute of Engineering and Technology, Patiala, India). The matter embodied in this thesis has not been submitted in part or whole to any other university or institute for the award of any degree in India or abroad.

**Shreya Sharma**

**Dr. Bonamali Pal**
(Professor and Supervisor)
Department of Chemistry and Biochemistry

**Dr. Niranjan Das**
(Professor and Supervisor)
Department of Biotechnology

# Acknowledgment

I express my sincere gratitude to the Almighty God for His constant blessings and guidance. His teachings provided direction and motivation throughout my research journey, and His grace remained a continual source of strength that enabled me to successfully complete this work.

The completion of this thesis was made possible through the invaluable support and encouragement of numerous individuals. I am sincerely grateful to all who contributed in different ways, and I acknowledge that words alone cannot adequately convey my appreciation for their guidance and support.

I would like to express my sincere appreciation to my research supervisors, **Prof. Bonamali Pal** and **Prof. Niranjan Das**, for their invaluable guidance and continuous support throughout this research work. I am deeply grateful for their insightful feedback, constructive suggestions, and patient mentorship at every stage of the study, from the initial conceptual framework to experimental planning and execution. Their encouragement and commitment have been a constant source of motivation, and without their dedicated supervision, the objectives of this research could not have been successfully accomplished.

I would also like to convey my sincere gratitude to **Dr. Padamkumar Nair**, Honourable Director; **Prof. R.S. Kaler**, Dean (Research & Development Cell); and **Prof. Manmohan Chhibber**, Head of the Department of Chemistry and Biochemistry at Thapar Institute of Engineering and Technology, Patiala, for providing me with the opportunity to pursue my doctoral research. I am deeply thankful to my doctoral committee members—**Prof. Soumen Basu**, **Dr. Mily Bhattacharya**, and **Prof. Bhupendrakumar Chudasama**—for their timely guidance, valuable insights, and constructive suggestions throughout the course of this work.

I also extend my sincere appreciation to **Prof. Satnam Singh** for kindly granting me access to his laboratory facilities, which greatly supported the progress of my research. I am truly grateful for the resources and encouragement provided, which played a significant role in advancing this study. Furthermore, I would like to acknowledge the continuous cooperation and assistance of **Mr. Chander Thakur**, **Mr. Hemant Kumar**, and **Mr. Mayank** from DCBC, as well as **Mr. Ram Nawal**, **Mr. Lallan Prashad**, and **Mr. Surinder** from DBT. Their support and dedication were invaluable during the course of my research work.

A special thanks to **Dr. Ashish Sharma** for his valuable guidance and support during the initial phase of my research. His insights and direction played a significant role in shaping the foundation of this work and helped orient my research in its early stages.

I would like to sincerely acknowledge my seniors **Dr. Yadveer**, and **Dr. Deepika** for their guidance. I am also thankful to my labmates **Davinder**, **Mehak**, **Riddhima**, **Sukhandeep**, **Jemini**, **Priti**, **Kirti**, and **Samridhi** for their cooperation, assistance, and supportive working environment. Additionally, I am grateful to my friends from other research groups—**Saurabh**, **Sunidhi**, **Santosh**, and **Neha** for their help throughout the course of this work.

I extend special thanks to my friends **Dipti Sharma**, **Arashdeep Kaur**, and **Sahil Vashisht** for their constant encouragement, motivation, and unwavering support during challenging times. Their emotional support and belief in me were instrumental in helping me persevere and successfully complete this journey.

I express my heartfelt gratitude and deep appreciation to my family, **Smt. Indra Sharma** and **Sh. Lalit Mohan**, for their unwavering encouragement and support in pursuing my aspirations. Their countless sacrifices and continued belief in me provided constant motivation and guidance throughout this journey. I am also thankful to my brother, **Dr. Nishant Sharma**, and my sister-in-law, **Dr. Shabnam**, for their love, encouragement, and emotional support. I lovingly acknowledge my nephew, **Vivaan Sharma**, whose presence and affection brought joy, positivity, and a sense of fulfilment during this journey. Lastly, I would like to express my deepest gratitude to my husband, **CA Sharad Sharma**, for his constant encouragement, and unwavering support. His belief in my abilities, understanding during challenging times, and continuous motivation played a vital role.

I gratefully acknowledge the support provided by external institutions and laboratories, including **SAI Labs**, the **Avantha Centre for Industrial Research and Development, TIET**, and **SPRINT Testing Solutions, Mumbai**. Their technical support and access to facilities were helpful in carrying out specific analyses.

In addition, I sincerely thank everyone who, directly or indirectly, contributed to the successful completion of this work through their support and encouragement.

Shreya Sharma

Dedicated to my Family

# Table of Contents



# Chapter 1

## *Introduction and Literature Review*

# Chapter 2

## *Preparation, structural characterization, and performance assessment of SPI/Mg–Al LDH bionanocomposite films*



# Chapter 3

## *Biodegradable wheat gluten/nanoclay films for food packaging applications*

# Table of Contents



# Chapter 1

## *Introduction and Literature Review*

# Chapter 2

## *Preparation, structural characterization, and performance assessment of SPI/Mg–Al LDH bionanocomposite films*



# Chapter 3

## *Biodegradable wheat gluten/nanoclay films for food packaging applications*

# Chapter 4

## *SPI/ZnAl LDH biocomposites for rapid tartrazine adsorption and evaluation of their antimicrobial activity*

# Abbreviations

| | |
|---|---|
| µm | Micrometre |
| a.u | Arbitrary unit |
| KNm/g | Kilo Newton metre per gram |
| mg | Milligram |
| g | Gram |
| min | Minute |
| h | Hour |
| SPI | Soy protein isolate |
| LDH | Layered double hydroxide |
| WG | Wheat gluten |
| C30B | Cloisite 30B |
| XRD | X ray diffraction |
| FESEM | Field emission scanning electron microscopy |
| SEM | Scanning electron microscopy |
| AFM | Atomic force microscopy |
| EDS | Energy dispersive X-ray spectroscopy |
| BNC | Bionanocomposite |
| ATR-FTIR | Attenuated Total reflectance-Fourier transform infrared spectroscopy |
| IS | Indian standard |
| TS | Tensile strength |
| EB | Elongation at break |
| C | Celsius |
| UV | Ultraviolet |
| Vis | Visible |
| BET | Brunauer Emmett Teller |
| DI | Deionized |
| Tr | Tartrazine |
| TGA | Thermogravimetric analysis |

| | |
|---|---|
| NaOH | Sodium hydroxide |
| NaCl | Sodium chloride |
| $H_2SO_4$ | Sulphuric acid |
| FDs | Food dyes |
| PSO | Pseudo second order |
| IPD | Intraparticle diffusion |
| D-R | Dubinin Raushkevich isotherm model |
| NaOCl | Sodium hypochlorite |
| MC | Moisture content |
| WCA | Water contact angle |
| LB | Luria broth |
| LA | Luria Agar |
| YI | Yellow index |
| S | Water solubility |
| Amp | Ampicillin |
| PZC | Point of zero charge |
| Mg | Magnesium |
| Zn | Zinc |
| Al | Aluminium |

# Symbols

| | |
|---|---|
| % | Percentage |
| α | Initial rate constant |
| β | Desorption process constant |
| $\lambda_{max}$ | Wavelength of maximum absorption |
| θ | Theta |
| Wt % | Weight percentage |
| R | Gas constant |
| $C_0$ | Initial concentration |
| $C_t$ | Concentration at time t |
| $K_L$ | Langmuir constant |
| k | Equilibrium constant |
| $q_e$ | Adsorption capacity at equilibrium |
| $q_t$ | Adsorption capacity at time t |
| $K_f$ | Freundlich constant |
| € | Polanyi constant |
| E | Mean free adsorption energy |
| OH | Hydroxyl |
| $R_L$ | Dimensionless constant |
| $K_{di}$ | Intraparticle constant |
| W | Weight |
| V | Volume |
| ° | Degree |

# Abstract

The increasing accumulation of non-biodegradable plastics and the growing concerns related to environmental pollution and water contamination have created an urgent need for sustainable and multifunctional materials. In response to these challenges, the present research was undertaken to develop protein-based bionanocomposites (BNCs) with improved physicochemical characteristics for applications in biodegradable food packaging and adsorption-based environmental remediation. The detailed understanding of the structural characteristics, preparation approaches, applications, advantages, and existing limitations of bionanocomposite systems, which helped identify key research gaps and establish the foundation for the experimental work. Particular emphasis was placed on the utilization of renewable protein sources in combination with suitable nanofillers to improve the functional performance of biopolymer-based materials**.**

Initially, SPI has emerged as a promising material in recent years because of its availability, sustainability, low cost, and favorable film-forming and processing characteristics. In the present work, novel SPI-based bionanocomposite films were fabricated by incorporating Mg–Al layered double hydroxide (LDH) at varying loadings (0%, 2%, 5%, and 9% w/w) through a straightforward solution-casting technique. The Mg–Al LDH was synthesized using a co-precipitation route with a molar ratio of 2:1. Structural and morphological characterization using Fourier transform infrared spectroscopy (FTIR), X-ray diffraction (XRD), field-emission scanning electron microscopy (FE-SEM), and thermogravimetric analysis (TGA) confirmed the intercalation and partial exfoliation of Mg–Al LDH layers within the SPI matrix. The extent of LDH particle agglomeration increased as the filler loading was raised from 0% to 9% (w/w). The resulting BNC films exhibited enhanced thermal stability. Their mechanical performance and biodegradation behavior were also evaluated. Tensile strength of the films containing 0%, 2%, 5%, and 9% w/w LDH were measured as 2.12 ± 0.25, 1.60 ± 0.15, 1.64 ± 0.08, and 1.58 ± 0.06 KN m $g^{-1}$, respectively. Notably, the SPI–Mg/Al LDH film with 5% loading demonstrated optimal mechanical properties; moreover, it was efficiently degraded in non-sterile soil.

Building upon these findings, novel wheat gluten (WG)/Cloisite 30B (C30B) organoclay-based bionanocomposite films were fabricated using a solution-casting technique with varying C30B loadings (5%, 10%, and 15%). Structural and morphological analyses using XRD and FESEM

confirmed the intercalation and partial exfoliation of C30B layers within the WG matrix. Among the prepared films, the WG–C30B 10% composition exhibited notable improvements in physicochemical properties, including reduced surface roughness, enhanced water barrier performance, and increased surface hydrophobicity. This BNC film demonstrated superior thermal stability. Mechanical testing revealed a significant enhancement in tensile strength, increasing from 0.70 ± 0.02 for neat WG films to 1.11 ± 0.01 for WG–C30B 10% films. Such films effectively inhibited the growth of some bacteria namely, *Staphylococcus aureus* and *Salmonella enterica* clearly indicating antibacterial properties. Shelf-life studies on green grapes were conducted under refrigerated (4 °C), ambient, and elevated temperature (42 °C) conditions. It was shown that the WG–C30B 10% film was effective in extending the shelf life up to 18 days under ambient conditions as compared to dip coated with WG-C30B 10% solution. Biodegradation studies demonstrated that over 50% of the BNC films were decomposed in agricultural soil within two weeks, while complete degradation occurred rapidly in sewage sludge soil. The prepared WG–C30B 10% film exhibited promising physicochemical, antibacterial, and biodegradation properties, clearly showing its potential for use in biodegradable food packaging applications.

To expand the scope of practical application, protein-based biocomposites were further explored as adsorbent systems for contaminant removal. A sensitive UV–visible spectroscopic technique was successfully employed to detect tartrazine (Tr), an azo dye, in commercially available food products. The study evaluated the adsorption performance of soy protein isolate (SPI)/ZnAl layered double hydroxide (LDH)-based biocomposites for effective Tr removal. ZnAl LDH with a 3:1 molar ratio and SPI/ZnAl LDH biocomposites containing varying SPI loadings (0.25–3 g) were synthesized using a co-precipitation approach. Several techniques namely, XRD, FTIR, SEM, EDS, TGA, DSC, and BET analyses were used in order to characterize the BNC films in a comprehensive manner. The crystallinity index of the 2:1 SPI/ZnAl LDH biocomposite was determined to be 53.8 ± 0.416%. FTIR analysis confirmed the presence of characteristic amide I (C=O stretching at 1621 $cm^{-1}$) and amide II (N–H bending at 1521 $cm^{-1}$) functional groups, indicating successful incorporation of SPI. Under optimized conditions i.e. initial dye concentration of 18 mg $L^{-1}$, pH 2.0, adsorbent dosage of 5.0 mg, and contact time of 60 min, the 2:1 SPI/ZnAl LDH biocomposite remained effective in achieving 99.85% dye removal at ambient temperature. Thermodynamic and adsorption parameters revealed a spontaneous process ($\Delta G = -2.72$ kJ $mol^{-1}$), with a maximum adsorption capacity (q_max) of 49.01 mg $g^{-1}$ and an adsorption equilibrium constant of 0.162 g $mg^{-1}$ $min^{-1}$.

The adsorption behavior was aptly described by both Langmuir ($R^2$ = 0.9935) and Freundlich ($R^2$ = 0.9959) isotherm models, along with pseudo-second-order kinetics. The biocomposite demonstrated efficient Tr removal from commercial samples, achieving removal efficiencies of 81.43% for Mountain Dew, 79.21% for yellow candy, 77.85% for custard powder, and 75% for food dye wastewater. Moreover, the adsorbent retained approximately 73% efficiency after five regeneration cycles, indicating good reusability. Antimicrobial activity against *Listeria* species and *Acinetobacter calcoaceticus* was also observed. The SPI–LDH hybrid system showed potential for the removal of hazardous dyes from food products and wastewater.

Overall, the findings of this work demonstrate that the integration of proteins with layered nanofillers offers an effective strategy for developing multifunctional bionanocomposites possessing improved thermal, mechanical, antimicrobial, biodegradable, and adsorption characteristics. These materials show strong potential as sustainable alternatives for food packaging and environmental applications.

# Chapter- 1

## *Introduction and Literature Review*

## 1.1 Introduction

### 1.1.1 Bionanocomposites (BNCs)

In the wake of ever-increasing environmental as well as health issues, including accumulation of non- biodegradable (conventional) plastics, overexploitation of earth's non-renewable sources, and large-scale usage of synthetic food dyes, the primary anticipation about bionanocomposites (BNCs) is undoubtedly rooted in the need to tackle such problems. These are regarded as a new generation of nanocomposites (NCs) which are emerging as a group of nanostructured hybrid materials in combination of nanotechnology, material sciences, and life sciences [1]. BNCs are non-conventional bioplastics derived from the bio-based or renewable resources from past decades to minimize the conventional waste. They are biodegradable materials made up from various biopolymers such as proteins, starch, heteropolysaccharides, cellulose, lipids) along with nano-sized organic/inorganic fillers like nanoclays, layered double hydroxides (LDHs), graphene, silica, etc, with at least one dimension in the range of 1–100 nm [2]. The large surface to volume ratio of the nanofillers enhances interactions between polymer matrix and filler leading to overall improvement of material performance [3]. However, when applied, the nanomaterials must be safe for food contact, biodegradable, not lead to adverse environmental effects, and economically feasible. A general schematic view of formation of BNCs is shown in **Scheme 1.1**. BNCs show advantages over conventional materials in context to their low cost, high dispersion in aqueous medium, transparency with better surface properties, biodegradability and ease of recyclability [4,5]. Even at low concentration nanofillers achieve better compatibility which is typically difficult with conventional composites that require higher proposition of fillers. They also provide various desirable attributes like heat retention, thermal stability, mechanical strength, adsorptive and barrier properties alongwith antimicrobial activities. In turn, the longevity and quality attributes of the materials formed by these composites get augmented. For instance, Sanusi et al [6] demonstrated that by incorporating montmorillonite and multi-walled carbon nanotubes into PLA had improved its thermal properties. Yanat et al [7] studied that chitin nanocrystals enhanced the mechanical strength of prepared films and showed antioxidant properties. Jiang et al [8] observed significant selective separation of oil/water in both aqueous and oil/water

combinations by using multipurpose organic-inorganic composite aerogel based on gelatin. The remarkable separation was resulted from their amphiphilic surface and hierarchical porous structure

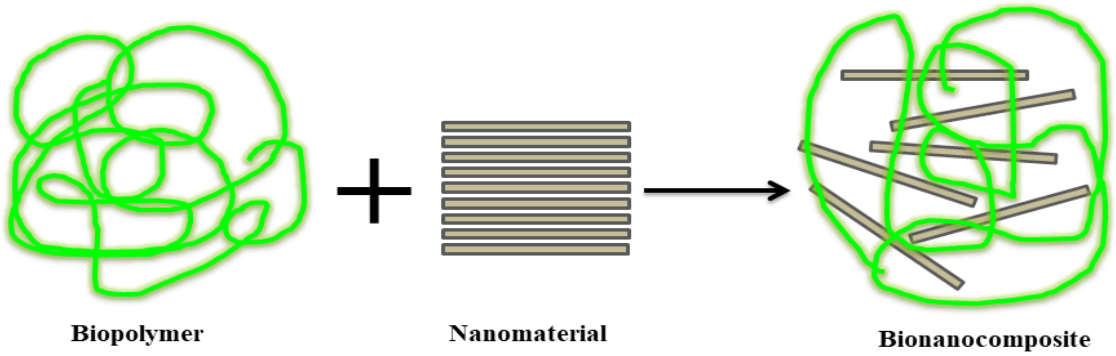


**Scheme 1.1** A general schematic representation showing formation of bionanocomposites

## 1.1.2 BNCs applications

### 1.1.2.1 BNCs as biodegradable packaging material

Most of the societies across the globe are associated with plastic materials for a long time due to the desired characteristics of various plastic products. Usually, basic packaging materials, such as paper and paperboard, plastic, glass, metal, and a combination of materials of various chemical natures and physical structures fulfil the functions and requirements of packaging for food and non-food materials depending on their types [9]. They also control humidity and useful in extending shelf life of the products. Some of the common packaging is presented in **Scheme 1.2a**. Conventional i.e., fossil-based plastics such as Polyethylene tetraphthalate (PET or PETE), High density polyethene (HDPE), Polyvinyl chloride (PVC), Polystyrene (PS) are widely used for the last many decades because of their low cost, strength, flexibility, versatility and durability along with desirable physico-chemical attributes [10,11]. Approximately 40% of the plastic produced worldwide is used for packaging, and because of its slow breakdown, a large portion of it winds up in the environment where it remains for centuries [12]. Usually, these non-biodegradable plastics are not eco-friendly as they keep on accumulating in the environment, as shown in **Scheme 1.2b.** Moreover, they do not mineralize over the time by biological processes like microbial degradation. Considering their widespread usage in various fields such as food packaging, clothes, shelter, communication, transportation, construction, health care, and the leisure industries, plastics are very important materials**.** These can be made biodegradable with the addition of certain chemicals that can alter the structure of the polymers.


**Scheme 1.2 (a)** Examples of common conventional packaging and **(b)** Accumulation of plastic waste

BNCs are regarded as an eco-friendly alternative to conventional fossil-based plastics [13]. They are widely accessible since they can be obtained from a variety of waste materials or by products of agrifood items. Because of their renewability, BNCs are now considered as a sustainable choice [14,15]. However, there are some shortcomings with regard to usage of biopolymers for developing these materials. They show weak mechanical properties, are brittle in nature and have high gas and water permeability [16,17]. Also, the conditions required for fast and complete degradation of bionanocomposites are rarely met in the natural environments; e.g., undegraded or partially-degraded bioplastics residues are hazardous to marine lives [18]. BNCs are synthesised by different methods such as solution casting, melt intercalation; *in-situ* intercalative polymerization and template synthesis, amongst them solution casting is the most adopted method [19]. During the past few decades, BNCs are being widely used in packaging industries. Abdollahi et al. [20] examined the influence of montmorillonite (MMT) and rosemary essential oil (REO) on chitosan-based films and reported an overall enhancement of physico-chemical properties exceeding 50%. Structural analyses using XRD and FTIR confirmed MMT exfoliation and strengthened interactions between the chitosan matrix and the nanoclay. In addition, films containing 1.55% (v/v) REO demonstrated notable antimicrobial activity. Schmid et al. [21] reported that coatings derived from whey proteins exhibited excellent oxygen barrier performance, with OTR values below 2 $cm^3(STP)/(m^2 \cdot d \cdot bar)$ when normalized to a thickness of 100 µm, comparable to those of ethylene vinyl alcohol copolymers. The coatings demonstrated good adhesion to substrates along with sufficient flexibility and mechanical robustness. Balakrishnan et al [22] studied the

effect of cellulose nanofibers (CNF) extracted from pineapple leaves on potato starch. 3 wt% of CNF increased the water contact angle to 51.77° from 41.25° and the water vapor permeability decreases from 7.32 to $5.68 \times 10^{-2}$ g $min^{-1}$ $m^{-2}$. The BNC films were UV resistant. Yadav et al [23] investigated improvement in alginate-based BNC films after the incorporation of cellulose nanocrystals and silver. The tensile strength was increased by 39-57%, whereas, water vapour permeability decreased by 17-36%. Li et al [24] studied the effect of multifunctional nanocomposite synthesized with protein zein nanoparticles (ZNs) and bacterial cellulose nanofibrils (BCNs). The nanocomposites showed improved mechanical properties and thermal stability alongwith better antimicrobial activity. Roufegarinejad [25] studied that 1% CuO and $TiO_2$ nanoparticles (NPs) lowered down the water vapor permeability, moisture content and water solubility of SPI-based films. They also enhanced the antioxidant properties of the films. Gunaki et al [26] revealed that CuO nanoparticles (CuO NPs)/chitosan (CS)/hydroxypropyl cellulose (HPC) based bio-nanocomposites showed improved tensile strength (33 MPa), significant UV-blocking ability and high decrease in moisture adsorption (5.27%) alognwith water vapour and oxygen permeability (2.47% and 1.39%, respectively). The composite was biodegradable in nature. It also exhibited antimicrobial and antioxidant effect against *B. subtilis, S. aureus, P. aeruginosa, E. coli, and C. albicans.* A considerable increase in the shelf life of jamun fruit was also observed. Arora and Saini [27] reported that BNC films based on pectin extracted from Malta peel (*Citrus sinensis*) with montmorillonite (MMT) nanoparticles showed greater tensile strength and decrease in water vapour permeability than films made of pectin only. Films were thermally stable. Farokhnasab et al [28] demonstrated antibacterial effect of chitosan/$TiO_2$/carbon quantum dots-based coatings. The experiment was conducted against 7 gram positive and gram negative bacteria using was assessed through disk diffusion, minimum inhibitory concentration (MIC), and minimum bactericidal concentration (MBC). Results indicated that the material poses strong antibacterial effects against gram negative bacteria than gram positive bacteria. In the study by Ghosh and Katiyar [29], the addition of edible nanochitosan to functionalized starch–guar gum biocomposites improved their physicochemical characteristics, leading to a hydrophobicity of about 114° and a noticeable extension in the shelf life of apples. According to Kumari et al. [30], incorporating 5 wt% grape seed oil and 0.7 wt% MgO nanoparticles provided UV-shielding and antioxidant functionality and suppressed bacterial growth, thereby increasing the shelf life of white button mushrooms to six days under ambient conditions. Tanwar et al [31] developed antioxidant films composed of PVA, corn starch, coconut shell extract, and sepiolite clay. The presence of sepiolite clay enhanced the physicochemical characteristics of the films,

whereas coconut shell extract imparted strong antioxidant activity, reaching nearly 80%. These films were effective in improving the oxidative stability of soybean oil when used as PVA–starch-based sachets.

In conclusion, bionanocomposites have emerged as promising alternatives to conventional packaging materials by combining sustainability with improved functional performance. The incorporation of nanofillers into biopolymer matrices enhances mechanical strength, thermal stability, barrier efficiency, antimicrobial activity, and shelf-life extension of packaged products. Despite certain limitations related to degradation behaviour and mechanical performance, continued advancements in formulation and processing make BNCs strong candidates for future eco-friendly packaging applications.

#### 1.1.2.2 BNCs as adsorbents

Industrial growth, urbanization and over exploitation of natural and man-made resources are becoming major concern for the environment. With the world's population growing at an accelerated rate and natural resources becoming less accessible, people are searching for sustainable development to meet both current and future expectations [32]. A global goal is to ensure proper disposal and elimination of hazardous chemicals with minimal negative impact on human health and natural resources. Among various pollutants released into the aquatic ecosystem, dyes are the major contributors which originate as effluents from multiple industries such as paints, paper, textiles, leather, resins, medicines, cosmetics, plastics, food, and industrial dyes [33]. The continuous release of dye containing wastewater may adversely affect human health due to its toxicity, potential carcinogenicity, bioaccumulation in aquatic biota, and mutagenicity [34]. It is estimated that, more than 10,000 types of dyes are available internationally, with an annual output of approximately 700,000 tons [35]. Bio-based materials are emerging as potential possibilities for water purification. They possess some desirable attributes such as hydrophilic nature to prevent fouling alongwith strong mechanical and chemical stability and ease of chemical modification. Biopolymers have considered showing potential in eliminating wide variety of pollutants from water [36]. Bio-based materials offer several significant advantages over conventional water treatment materials: i) natural abundance, (ii) ability to selectively remove trace heavy metals, (iii) biodegradable and (iv) cost-effective and energy efficient. These characteristics make them suitable for use as adsorbents in water purification [37]. Despite the numerous advantages of these materials, certain challenges still need to be resolved. Due to inadequate utilization of low-cost feedstocks

such as lignocellulosic biomass, the production cost of these materials remains too high for large-scale manufacturing. Furthermore, their intrinsic properties must be adjusted to match specific target chemicals [38]. The synthesis techniques, nature of the pollutant, kinetics, removal mechanism and recyclability are some of the crucial concepts for studying these materials [39,40]. Various techniques such as advance oxidative degradation, electrocoagulation, membrane filtration, biochemical degradation, flocculation, chemical precipitation, reverse osmosis, electrodialysis, and ion-exchange methods have been used to separate pollutants from water [41,42]. Due to their expensive and difficult handling, adsorption is regarded as the most promising technique. It is an economical, efficient and versatile method for removing toxic pollutants from the aquatic ecosystem [43]. Adsorption is a surface phenomenon that usually occurs through intermolecular interactions between adsorbate and adsorbent. For instance, Adqam et al [44] demonstrated that the whey protein concentrates nanofibrils and montmorillonite-based BNCs were used for adsorption of Chrysoidine-G, Bismarck brown-R, reactive black-5, reactive orange-16, acid red-88, acid red-114 and direct violet-51, Congo red dyes. It was observed that 93% of Chrysoidine-G was adsorbed over a broad range of dye concentration and pH. Pseudo second order and intraparticle diffusion models were best fitted. Ren et al [45] revealed that out of selected dyes the removal percentage of acid fuchsin (AF) and methyl orange (MO) was between 80.0 and 93.3% with maximum adsorption capacities of 1111 mg/g and 667 mg/g, respectively by using gelatin/chitosan/β-cyclodextrin hydrogel (GEL/CS/β-CD) as adsorbent. Adsorption was spontaneous, following Langmuir isotherm and pseudo second order kinetic models. Ma et al [46] investigated adsorptive performance of Hierarchical mesoporous $TiO_2$/starch-based microparticles for methyl orange (MO) and crystal violet (CV). The maximum adsorption capacities were found to be 85.8 mg/g and 103.8 mg/g for MO and CV, respectively. 80% of the composite was regenerated. Al-Raimi et al [47] reported removal of methylene blue (MB) and safranin O (SO) by silver-micro cellulose nanocomposite. Maximum removal efficiency was observed at pH 10 for MB and 6.0 for SO with adsorption capacities of 17.99 mg/g for MB and 14.90 mg/g for SO. The composite followed Langmuir and pseudo-second-order models. The process was exothermic and physisorption. Alenezi et al [48] demonstrated removal of cationic and anionic dyes by oxidized sodium alginate/silica hybrid. 78.6 mg/g and 192.7 mg/g of adsorption capacities were found for methylene blue (MB) and methyl orange (MO), respectively. Adsorption was spontaneous and endothermic; it followed Langmuir isotherm model. Oruganti et al [49] demonstrated that algal–bacterial consortia offer an environmentally sustainable approach to wastewater treatment. These systems operate through synergistic

interactions such as metabolic exchange, cell-to-cell communication, and quorum sensing mechanisms, providing a viable alternative to conventional treatment technologies.

Bio-based adsorbent materials have emerged as sustainable and efficient alternatives for wastewater treatment due to their biodegradability, cost-effectiveness, and strong adsorption performance. Their ability to remove diverse pollutants through multiple adsorption mechanisms highlights their potential for environmental remediation, although further improvements in scalability, selectivity, and regeneration are necessary for large-scale applications.

### 1.1.3 Preferred biopolymer and nanofillers

#### 1.1.3.1 Proteins as biopolymer

Biopolymers such as proteins, starch, chitosan, cellulose, lignin, etc are being used in making bioplastics which potentially offer a better solution for both food packaging and waste disposal in comparison to the conventional plastics [50–55]. Out of these different biopolymers, proteins occupy a pivotal position in preparing BNCs. They possess 3-D structure and has a linear hetero-bioploymer. More than 100 amino acid residues are present in a protein molecule. Usually, it comprised of 20 amino acids that are joined together by amide linkages known as polypeptides [56]. They are broadly classified into plant proteins, such as soy protein, wheat gluten, zein, and pea protein. The animal proteins include gelatin, collagen, casein, and whey protein. Among these, soy protein, wheat gluten, zein, gelatin, casein, and whey proteins are most frequently explored for films and coatings due to their availability and ability to form cohesive networks through hydrogen bonding, hydrophobic interactions, disulfide linkages, and electrostatic interactions. Compared with polysaccharides, protein-based films generally show better oxygen-barrier properties and greater functional tunability; however, they often suffer from poor water resistance, brittleness, weak mechanical stability, and sensitivity to humidity. These limitations have been partly addressed through plasticization, cross-linking, blending with polysaccharides or lipids, and incorporation of nanofillers such as nanoclays, ayered double hydroxides (LDHs), layered silicates, cellulose nanocrystals, and metal oxide nanoparticles.

The availability of different functional groups in the amino acids of protein chains brings out a great deal for the production of bioplastics compared to other polysaccharides or biopolymers. The functional properties of protein depend upon nature and composition of amino acids. The

interaction capability of amino acid side groups plays a decisive role in forming both intra- and intermolecular associations among polypeptide chains, which ultimately define protein architecture. Weak intermolecular forces, including hydrogen bonding and van der Waals interactions, are primarily responsible for stabilizing the three-dimensional configuration of proteins. In protein-based BNCs, the resulting mechanical and barrier characteristics are largely influenced by the interaction strength and compatibility between the protein matrix and the nanofiller phase [57]. These material properties can be further tailored through careful control of processing and fabrication parameters. For instance, Koshy et al [58] observed that soy protein isolate (SPI) BNC films blended with magnesium oxide nanoparticles (MgO NP) and chitin nanowhisker (CNW) showed significantly higher thermal stability, water barrier properties and antibacterial activites. MgO NPs were synthesized by sol-gel method. Rabee et al [59] revealed that when 5 wt% of biosynthesized magnesium nanoparticles (MgO NPs) was blended with poly(vinyl alcohol) (PVA) and gelatin (Ge) then the prepared films showed significantly higher tensile strength (22.10 MPs) as compared to only poly(vinyl alcohol) (PVA) and gelatin (Ge)-based films. Also, PVA/Ge-1% MgO NPs sensor had higher sensitivity over a broad range of relative humidity from (7–97% RH) and at 100 Hz. Sharma et al [60] demonstrated the extension of shelf-life of paneer by wrapping them with films based on montmorillonite (MMT)/starch nanocrystals (SNCs) on gluten-loaded chitosan. The freshness was preserved upto 12 days. Bhavya and Raman [61] revealed that refined carrageenan (RC)/ nanocellulose (NC)/ soy protein (SP)0.4 BNC films showed better tensile strength (36.5 MPa) compared to semi refined carrageenan (SRC)/NC/SP0.4 films (19.7 MPa). The water vapour transmission rate was considerably high in case of only RC films (1677 g $m^{-2}$ 24 $h^{-1}$) which was reduced to almost 50% in RC/NC/SP films. The films were prepared by solution casting method. Panthi et al [62] reported that incorporation of curcumin into wheat gluten (WG) matrix enhances the UV-barrier capacity, mechanical and antioxidant properties of the films. The films were hydrophobic in nature with decreased water vapor permeability. Ghanavati Nasab et al [63] studied that hydroxyapatite nanoparticles loaded on Zein (Zein/nHAp) adsorb the congo red dye from aqueous solutions. The maximum removal percentage of 99.48% was obtained under the optimum condition with maximum adsorption capacity of 416.66 mg/g. The process was spontaneous and endothermic. Ren et al [64] revealed that gelatin hydrogel (GH) showed significant adsorption for selected dyes. The maximum adsorption capacities for crystalline violet (CV), methyl orange (MO), acid fuchsin (AF), congo red (CR), malachite green (MG), and methylene blue (MB) were 138.89 mg/g, 72.63 mg/g, 66.29 mg/g, 64.84 mg/g, 64.64 mg/g, and 60.32 mg/g, respectively. Nearly 60 % of GH was recovered after five

consecutive adsorption–desorption cycles. Vadivel et al [65] observed removal of rhodamine B dye by casein-surfactant complexes. Sodium dodecyl sulfate (SDS), cetyltrimethylammonium bromide (CTAB) and Triton X-100 were used as model surfactants. Triton X-100 improved the dye removal efficiency of casein upto 84% with a contact time of 5 min. The adsorption process followed Freundlich isotherm and pseudo second order kinetics models. Revadekar et al [66] studied the significant adsorption of methyl blue (MB) dye on soy protein isolate (SPI)/sodium alginate (ALG)/polyethyleneimine (PEI) aerogel. The adsorption capacity for MB was 106.3 mg/g. The composite followed Langmuir isotherm model and pseudo-second-order kinetic model. Approximately 80% of the adsorbent was recovered in the fourth regenerative cycle. Abu Elella et al [67] investigated effect of gelatin crosslinked poly(acrylamide-*co*-itaconic acid)/montmorillonite nanocomposites on adsorption of malachite green. The composite followed Langmuir isotherm model with maximum adsorption capacities of 950.5 mg/g using 350 mg/L of MG dye at pH 9 within 45 min.

Proteins are widely used in both food and non-food sectors because of their nutritional value and functional versatility. In food applications, proteins primarily serve as nutritional ingredients and perform technological functions such as emulsification, gelation, foaming, and texture enhancement. Common examples include soy protein, whey protein, casein, gelatin, wheat gluten, and zein, which are extensively used in processed foods and beverages. However, increasing interest in sustainable materials has expanded the utilization of proteins beyond food systems into packaging applications. All proteins does not equally possess suitability for packaging applications. The selection depends on factors such as availability, cost, film-forming ability, barrier performance, processability, and environmental compatibility. For instance, SPIs and wheat gluten have received considerable attention because of their abundance and ability to form continuous films, whereas whey protein and zein exhibit excellent oxygen barrier characteristics. Nevertheless, limitations including moisture sensitivity, brittleness, and moderate mechanical strength continue to restrict large-scale commercialization. Therefore, combining proteins with nanofillers and applying suitable modification strategies provides an effective route to improve their functional performance and broaden their applicability in sustainable packaging systems.

In conclusion, proteins represent highly promising biopolymers for the development of BNCs owing to their structural diversity, functional adaptability, and compatibility with nanofillers. Their properties can be effectively tailored to improve mechanical, barrier, thermal, antimicrobial, and adsorption performance. However, challenges such as moisture sensitivity

and limited large-scale applicability still remain, highlighting the need for continued material optimization for sustainable packaging and environmental applications.

### 1.1.3.2 Layered double hydroxides (LDHs) and nanoclays as nanofiller

Layered double hydroxides are inorganic compounds having both natural as well as synthetic origin. These are generally referred to as hydrotalcite having chemical formula $[Mg_6Al_2\ (OH)_{16}]CO_3.4H_2O$ with rhombohedral crystallinity and structural properties comparable to those of brucite $Mg(OH)_2$. The general chemical composition of layered double hydroxides is: $M(II)_{1-X}M(III)_X(OH)_2(A^{n-})_{x/n}.mH_2O$, where $M^{2+}$ is divalent cation (e.g., $Ca^{2+}$, $Mg^{2+}$, $Sr^{2+}$ etc.); $M^{3+}$ is trivalent cation (e.g., $Al^{3+}$, $V^{3+}$, $Cr^{3+}$ etc) and $A^{n-}$ is the exchangeable anion intercalated between the positively charged metal hydroxide layers, x is the layer charge density. The molar ratio of $[M^{3+}/(M^{2+}+M^{3+})]$ usually comes in the range 0.2–0.33, m is the number of $H_2O$ molecules suited in the region between two brucite like layers alongside anions [68]. The $M^{2+}$ ions are uniformly distributed throughout the brucite layers, with some of them partially replaced by $M^{3+}$ ions, which have ionic radii that are less than those of $M^{2+}$ ions. For instance, Elhalil et al [69] synthesized ZnAl LDH, where $Zn^{2+}$ ions with ionic radii of 0.74 nm were partially replaced by smaller $Al^{3+}$ ions (0.53 nm).

Mixed metal hydroxides are formed when six $OH^-$ ions octahedrally encircle the divalent and trivalent cations. By sharing the edges of the $MO_6$ octahedron, these octahedral units create infinite metal hydroxide brucite-like layers of general composition $[M^{2+}_{(1-x)}M^{3+}_{(x)}(OH)_2]^{x+}$ that assemble on top of each other. The O–H bond is located at a right angle to the plane of the brucite-like layers. A positive charge is imparted to the brucite-like layers by the fractional substitution of $M^{3+}$ ions for $M^{2+}$. The structure is kept electroneutral by the negatively charged intercalated anions counteracting the positive charge of the brucite-like layers [70,71]. The general structure of layered double hydroxide has shown in **Scheme 1.3**. The interlayer anion exchangeable capability of LDHs serves as inorganic matrices for encapsulating functional biomolecules with negative charge in aqueous media. Almost all type of anions can be adjusted into their structural composition with respect to positively charged brucite like layers and interlayer region possessing weak interlayer bonding [72]. LDHs show several desirable properties like enhanced adsorptive properties [73] thermostability [74], antimicrobial [75], catalysis [76].

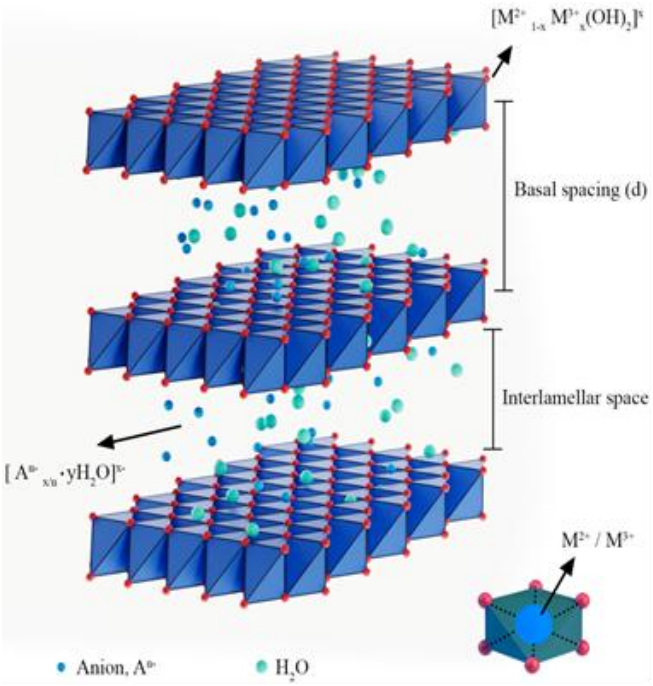


**Scheme 1.3** Structure of a layered double hydroxide (LDH)

Nowadays, polymer-clay nanocomposites have significantly received attention as a substitute for conventional plastics, because of their ability for nano-scale dispersion. They vastly improve the mechanical and physical properties of BNCs as compared to only biopolymer composites. Clays have become useful in the packaging industries due to their availability, low cost and ease of processability. The first successful biopolymer-clay hybrid was made at Toyota Central Research Laboratories in 1986 [77]. The system comprised a nylon–clay hybrid, in which the clay minerals exhibit a characteristic stacked configuration of negatively charged silicate layers with a thickness of nearly 1 nm and lateral dimensions of around 100 μm. Nanoclays constitute a diverse group of naturally occurring inorganic minerals, essentially composed of nanoscale layered silicate structures [78]. Based on their structural characteristics, they are categorized into several classes, including smectite, chlorite, kaolinite, and halloysite [79]. They shows various properties such as enhancing mechanical strength, allow surface modifications and act as heat insulators, act as good hosts for loading and controlled release of materials, show antimicrobial activity and exhibit better adsorbent properties for removal of pollutants. General chemical structure of C30B has shown in **Scheme 1.4**.

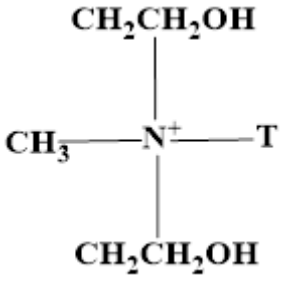


**Scheme 1.4** Chemical structure of Cloisite 30B (C30B)

We can conclude that, LDHs and nanoclays have emerged as versatile nanofillers due to their layered structure, ion-exchange capability, and ease of incorporation into polymer matrices. Their ability to enhance mechanical, thermal, antimicrobial, and adsorptive properties makes them highly promising materials for advanced bionanocomposite, packaging, and environmental applications.

## 1.2 Research Gaps

Protein-based BNCs, for instance SPI/MMT and Wheat gluten blends, have been studied but their commercial use remains limited due to poor moisture resistance, brittleness, moderate mechanical strength, weak long-term stability, and non-uniform nanofiller dispersion. Therefore, specific improvements are required, including better interfacial compatibility, reduction in water sensitivity, enhancement of tensile strength and flexibility, improved thermal performance, and retention of biodegradability. These limitations may be addressed through, surface modification, cross-linking, plasticizer optimization, and blending with suitable nanofiller selection to support wider practical applications. Certain nanofillers can be added to enhance the properties such as protection against UV-radiation, prevent food oxidation and can do adsorption and desorption. Currently, LDHs are being widely used because of their availability, high stability, compatibility and ease of blending with biopolymers. It is apparent that LDHs-based BNCs are quite promising to prepare packaging materials with desirable features. Therefore, a scope is there in preparing and modifying protein-based BNCs with some novel features. At present government authorities of many countries have taken initiatives in regulating the usage of these materials. In fact, there is a considerable progress with regard to various processes and products but for packaging of both food and non-food materials suitable biodegradable BNCs are still lacking.

.

## 1.3 Objectives

- Preparation and characterisation of Mg-Al and Zn-Al LDH micro/nano composites
- Fabrication of protein-Mg-Al/Zn-Al LDH and protein-nanoclay bionanocomposites for evaluation physico-chemical properties
- To investigate their thermal, antimicrobial, adsorption-desorption properties

## 1.4 Methodology

### 1.4.1 Synthesis of layered double hydroxides (LDHs)

LDHs can be synthesised by various methods like co-precipitation, urea hydrolysis and hydrothermal synthesis. Among these, co-precipitation is the most common method used for LDHs synthesis. Briefly, a thoroughly mixed metal solution of M(II) and M(III) salts was dropwise added to base solution of NaOH/$Na_2CO_3$ and then the reaction mixture was kept on agitation. The resultant slurry was washed several times and then dried in conventional oven for overnight. In order to obtain pure LDH with high chemical homogeneity, the pH is kept constant by adding base solution side by side throughout the reaction. Details are given in the Chapter-2 and 4 under the heading, "synthesis of Mg-$CO_3$-Al layered double hydroxide (LDH)" and "synthesis of SPI/ZnAl biocomposites", respectively. A schematic representation of co-precipitation method is shown in **Scheme 1.5**.

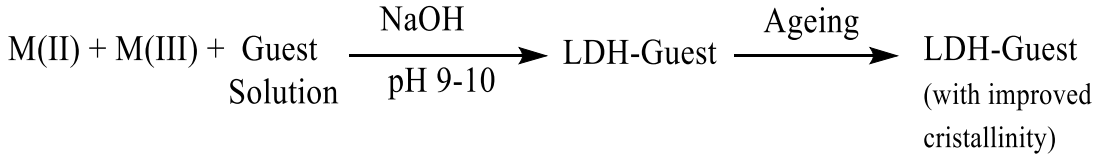


**Scheme 1.5** Schematic representation of co-precipitation method

### 1.4.2 Preparation of BNC films

The BNC films were prepared by solution casting method. It is usually a low temperature process and provides films with uniform thickness, optical purity, low haze, and isotropy. Basically, the casting from aqueous medium is the easiest and most straightforward route to produce bio-based nanocomposites as the nano reinforcements under consideration are most stable in aqueous medium. In this case, the matrix phase used should be water-soluble or

dispersive polymers. The spreading of inorganic layered particles introduces the macromolecules of polymer into its interlayer. Further, precipitation of the blend (polymer + nanofiller) takes place after the evaporation of remaining solvent. Details are given in the Chapter-2 and 3 under the heading, "Preparation of SPI/Mg-Al LDH films" and "Preparation of WG-C30B bionanocomposite films". A schematic representation of solution casting method is shown in **Scheme 1.6**.

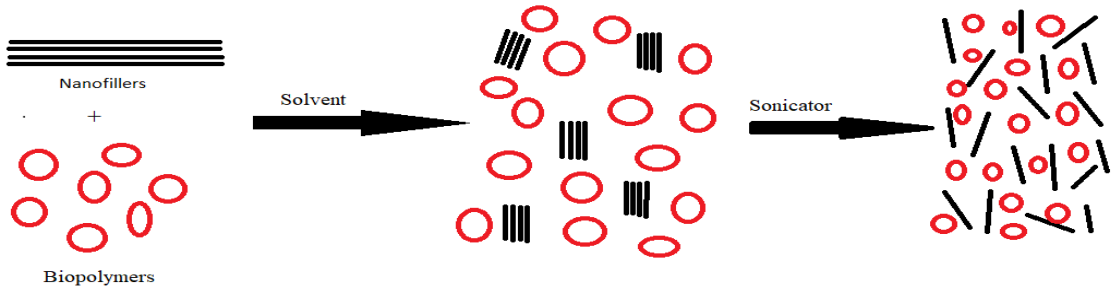


**Scheme 1.6** Schematic representation of solution casting method

## 1.5 Characterization techniques

Some common, eco-friendly and cost-effective methods were employed to synthesize pristine MgAl and ZnAl LDHs and BNC films with varying weight percentages of LDH as well as proteins (experimental details are mentioned in respective chapters). Various characterization techniques to study structural, functional, morphological, physico-chemical properties of these materials are discussed below:

### 1.5.1 X-ray diffraction (XRD)

The crystalline structure, phase purity, and diffraction patterns of all the synthesized materials were analyzed via X-ray powder diffraction technique using a PANalytical-Xpert-Pro diffractometer with Cu K-α (λ = 0.154 nm) radiations, and the data were taken at 2θ = 5°–80° (with step size = 0.01°).

### 1.5.2 Fourier transform infrared spectroscopy (FTIR)

To study the presence of functional groups in the synthesised materials, Shimadzu, IRTracer-100 Fourier Transform Infrared Spectrophotometer with ATR mode was used. The wavelength range was set at 400-4000 $cm^{-1}$ and spectral resolution of 2 $cm^{-1}$.

### 1.5.3 Morphological analysis

Surface morphology of the prepared materials was examined by (i) Field emission scanning electron microscopy (FESEM, Carl Zeiss Sigma 500, Germany), alongwith energy dispersive spectroscopy (EDS, Bruker, USA) for elemental composition analysis, (ii) Scanning electron microscopy (SEM, JSM, 65101v JEOL, Japan) and (iii) Atomic force microscopy (AFM, model: NT-MDT Solver NEXT, Russia).

### 1.5.4 Surface area determination

The surface area, pore size and pore volume were analyzed by Brunauer-Emmett-Teller (BET) analysis using Quantachrome Touchwin v1.24 surface analyzer from Quantachrome Instruments, USA.

### 1.5.5 Thermal properties

Thermal analysis of the samples was conducted by using (i) Thermogravimetric analyzer was used to analyze the thermal stability of the samples (TGA, NETZSCH STA 449 F3 Jupiter®-Thermal Analysis System, Germany) and (ii) Differential scanning calorimeter (DSC, Linseis high-temperature DSC PT-1600).

### 1.5.6 Physico-chemical properties of BNC films

(i) Mechanical properties of the prepared films was studied using a Tensile Strength Tester (Digital vertical model, Angels Instruments, India) based on a standard method IS 1060–1 (Indian Stand ard, Part 1), (ii) The thickness of BNC films was measured with a micrometer thickness gauge (L&W Micrometer, Switzerland), (iii) Surface color of the films was determined by using a brightness tester (L&W Elrepho Brightness Tester, Switzerland), (iii) Water contact angle (WCA) was measured by goniometer contact angle measuring device (Apex Instruments Co. Pvt. Ltd., India) in a static contact angle mode, alongwith moisture content (MC) and water solubility.

## 1.6 Antimicrobial Activity and Shelf-life extension

The antimicrobial activities of the prepared BNC films and bioadsorbent were examined by Agar disc diffusion method. Shelf-life extension was studied by using method of dip coating and wrapping with BNC films.

## 1.7 Biodegradability test

Biodegradability test for BNC films was conducted by composting method using (i) normal soil (ii) agricultural soil and (iii) Sewage sludge soil.

## 1.8 Adsorption studies

The adsorption of Tartrazine (food dye) (shown in **Table 1.1**) by synthesised bioadsorbent was assessed under dark conditions. A required amount of bioadsorbent was added to different test tubes containing the aqueous dye solutions. These dispersions were stirred under dark conditions, and the solutions were collected after fixed time intervals and ultracentrifuged to separate out the bioadsorbent. The remaining dye concentrations were assessed using a UV-visible spectrophotometer (JASCO V-750) to measure the changes in absorption spectra before and after the adsorption process. The fitting of reaction parameters into Langmuir, Freundlich, Dubinin Raushkevich (D–R) and Temkin isotherm models were examined for insights into the adsorption mechanism. Pseudo-second-order (PSO), Elovich and Intraparticle diffusion kinetic (IPD) kinetic models were implemented to forecast the reaction kinetics. The corresponding chapters provide a detailed explanation of the intricate processes and formulas.

**Table 1.1** Model food dye chosen for the adsorption studies using the prepared bioadsorbent

| Chosen food dye | Chemical formula | Chemical structure | Hazardous impacts |
|---|---|---|---|
| Tartrazine | $C_{16}H_9N_4Na_3O_9S_2$ | 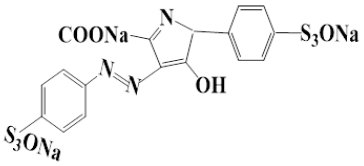 | Triggers dermatitis, eczema and irritation or depression [80]. Allergic symptoms, including urticaria and asthma [81] |

### References


1. Ozin GA, Arsenault A (2015) Nanochemistry: a chemical approach to nanomaterials. Royal Soc Chem
2. Zhao R, Torley P, Halley PJ (2008) Emerging biodegradable materials: starch-and protein-based bio-nanocomposites. J Mater Sci 43:3058–3071.

3. Supova M, Martynkova GS, Barabaszova K (2011) Effect of nanofillers dispersion in polymer matrices: a review. Science of advanced materials. 3:1–25. https://doi.org/10.1166/-sam.2011.1136.
4. Saini RK, Bajpai AK, Jain E (2017) Fundamentals of bionanocomposites. Biodegradable and biocompatible polymer composites: Processing, properties and applications. 351–377.
5. Kendre PN, Chaudhari PD (2018) Effect of amphiphilic graft co-polymer-carrier on physical stability of bosentan nanocomposite: Assessment of solubility, dissolution and bioavailability. Eur J Pharm Biopharma 126:177–186. https://doi.org/10.1016/-j.ejpb.2017.06.024.
6. Sanusi OM, Benelfellah A, Papadopoulos L, Terzopoulou Z, Malletzidou L, Vasileiadis IG, Hocine NA (2021) Influence of montmorillonite/carbon nanotube hybrid nanofillers on the properties of poly (lactic acid). Appl Clay Sci 201:105925. https://doi.org/10.1016/-j.clay.2020.105925.
7. Yanat M, Colijn I, De Boer K, Schroen K (2023) Comparison of the degree of acetylation of chitin nanocrystals measured by various analysis methods. Polym 15:294. https://doi.org/10.3390/polym15020294.
8. Jiang J, Zhang Q, Zhan X, Chen F (2019) A multifunctional gelatin-based aerogel with superior pollutants adsorption, oil/water separation and photocatalytic properties. Chem Eng J 358:1539–1551. https://doi.org/10.1016/j.cej.2018.10.144.
9. Rhim JW, Park HM, Ha CS (2013) Bio-nanocomposites for food packaging applications. Prog Sci 38:1629–1652. https://doi.org/10.1016/j.progpolymsci.2013.05.008.
10. Millican JM, Agarwal S (2021) Plastic pollution: a material problem? Macromol 54:4455–4469. https://doi.org/10.1021/acs.macromol.0c02814.
11. Kouloumpis V, Pell RS, Correa-Cano ME, Yan X (2020) Potential trade-offs between eliminating plastics and mitigating climate change: an LCA perspective on polyethylene terephthalate (PET) bottles in Cornwall. Sci Total Environ 727:138681. https://doi.org/10.1016/-j.scitotenv-.2020.138681.
12. Plastics Europe Plastics, The Facts 2022, Plastics Europe Association of Plastics Manufacturers, 2022.
13. Ghasemlou M, Barrow CJ, Adhikari B (2024) The future of bioplastics in food packaging: an industrial perspective, Food Packag. Shelf Life 43:101279. https://doi.org/10.1016/-j.fpsl.2024.101279.
14. Colijn I, Postma E, Fix R, van der Kooij HM, Schro¨ en K (2024) Particle dispersion governs nano to bulk dynamics for tailored nanocomposite design. J Col Inter Sci 658:354–361. https://doi.org/10.1016/j.jcis.2023.12.071.
15. Baraketi S, Khwaldia K (2024) Nanoparticles from Agri-food by-products: green technology synthesis and application in food packaging. Curr Opin Green Sustain Chem 100953. https://doi.org/10.1016/-j.cogsc.2024.100953.

16. Pandey JK, Reddy KR, Kumar AP, Singh RP (2005) An overview on the degradability of polymer nanocomposites. Polym Degrad Stabl 88:234–250. https://doi.org/10.1016/-j.polymdegradstab.2004.09.013.
17. Tang XZ, Kumar P, Alavi S, Sandeep KP (2012) Recent advances in biopolymers and biopolymer-based nanocomposites for food packaging materials Critical Reviews in Food Sci Nutr 52:426–442. https://doi.org/10.1080/10408398.2010.500508.
18. Lambert S, Wagner M (2017) Environmental performance of bio-based and biodegradable plastics: the road ahead Chem Soc Rev 46:6855–6871. 10.1039/c7cs00149e.
19. Zhao R, Torley P, Halley PJ (2008) Emerging biodegradable materials: starch-and protein-based bio-nanocomposites. J Mater Sci 43:3058–3071. https://doi.org/10.1007/ s10853-007-2434-8.
20. Abdollahi M, Rezaei M, Farzi G (2012) A novel active bionanocomposite film incorporating rosemary essential oil and nanoclay into chitosan. J. Food Eng 111(2):343–350. https://doi.org-/10.1016/j.jfoodeng.2012.02.012
21. Schmid M, Dallmann K, Bugnicourt E, Cordoni D, Wild F, Lazzeri A, Noller K (2012) Properties of whey-protein-coated films and laminates as novel recyclable food packaging materials with excellent barrier properties. Inter J Polym Sci 2012(1):562381. https://doi.org/10.1155/-2012/562381
22. Balakrishnan P, Gopi S, MS S, Thomas S (2018) UV resistant transparent bionanocomposite films based on potato starch/cellulose for sustainable packaging, Starch-Starke. 70:1700139. https://doi.org/10.1002/star.201700139.
23. Yadav M, Liu YK, Chiu FC (2019) Fabrication of cellulose nanocrystal/silver/alginate bionanocomposite films with enhanced mechanical and barrier properties for food packaging application. Nanomaterials 9:1523. https://doi.org/10.3390/nano 9111523.
24. Li Q, Gao R, Wang L, Xu M, Yuan Y, Ma L, Wan Z, Yang X (2020) Nanocomposites of bacterial cellulose nanofibrils and zein nanoparticles for food packaging. ACS Appl Nano Mater 3:2899–2910. https://doi.org/10.1021/acsanm.0c00159.
25. Roufegarinejad L (2022) Development and characterization of the reinforced soy protein isolate-based nanocomposite film with CuO and $TiO_2$ nanoparticles. J Polym Environ 30:2507–2515. https://doi.org/10.1007/s10924-022-02374-9.
26. Gunaki MN, Masti SP, D'souza OJ, Eelager MP, Kurabetta LK, Chougale RB, Kadapure AJ, Kumar SP (2024) Fabrication of CuO nanoparticles embedded novel chitosan/hydroxypropyl cellulose bio-nanocomposites for active packaging of jamun fruit. Food Hydrocoll 152:109937. https://doi.org/10.1016/j.foodhyd.2024. 109937.
27. Arora D, Saini CS (2025) Bio-Nanocomposite Film Based on Pectin From Citrus sinensis Peel Reinforced With Montmorillonite With Improved Mechanical and Barrier Properties, Future Postharvest and Food. https://doi.org/10.1002/fpf2.70026.

28. Farokhnasab O, Moghadam A, Eslamifar Z, Moghadam AH (2025) Fabrication and characterization of chitosan-based bionanocomposite coating reinforced with $TiO_2$ nanoparticles and carbon quantum dots for enhanced antimicrobial efficacy. Inter J Biol Macromol 296 :139648. https://doi.org/10.1016/j.ijbiomac.2025.139648.
29. Ghosh T, Katiyar V (2022) Nanochitosan functionalized hydrophobic starch/guar gum biocomposite for edible coating application with improved optical, thermal, mechanical, and surface property. Inter J Biol Macromol 211:116–127. https://doi.org/10.1016/-j.ijbiomac.2022.05.079
30. Kumari SVG, Pakshirajan K, Pugazhenthi G (2024) Development and characterization of active poly (3-hydroxybutyrate) based composites with grapeseed oil and MgO nanoparticles for shelf-life extension of white button mushrooms (Agaricus bisporus). Inter. J. Biol. Macromol. 260:129521. https://doi.org/10.1016/j.ijbiomac.2024.129521
31. Tanwar R, Gupta V, Kumar P, Kumar A, Singh S, Gaikwad KK (2021) Development and characterization of PVA-starch incorporated with coconut shell extract and sepiolite clay as an antioxidant film for active food packaging applications. Inter. J. Biol. Macromol. 185:451-461.https://doi.org/10.1016/j.ijbiomac.2021.06.179
32. Blum C, Bunke D, Hungsberg M, Roelofs E, Joas A, Joas R, Blepp M, Stolzenberg HC (2017) The concept of sustainable chemistry: Key drivers for the transition towards sustainable development. Sustain Chemi Pharm 5:94–104. https://doi.org/10.1016/j.scp.2017.01.001.
33. Ranjbar D, Raeiszadeh M, Lewis L, MacLachlan MJ, Hatzikiriakos SG (2020) Adsorptive removal of Congo red by surfactant modified cellulose nanocrystals: A kinetic, equilibrium, and mechanistic investigation. Cellulose 27:3211–3232. https://doi.org/10.1007/s10570-020-03021-z.
34. Gao Y, Deng SQ, Jin X, Cai SL, Zheng SR, Zhang WG (2019) The construction of amorphous metal-organic cage-based solid for rapid dye adsorption and time-Dependent dye separation from water. Chem Eng J 357:129–139. https://doi.org/10.1016/j.cej.2018.09.124.
35. Elgarahy AM, Elwakeel KZ, Elshoubaky GA, Mohammad SH (2019) Untapped Sepia Shell–Based Composite for the Sorption of Cationic and Anionic Dyes. Water Air Soil Poll 230:1–23. https://doi.org/10.1007/s11270-019-4247-1.
36. Sheikh MS, Rahman MM, Rahman MS, Yildirim K, Maniruzzaman M (2023) Fabrication of nano composite membrane filter from graphene oxide (GO) and banana rachis cellulose nano crystal (CNC) for industrial effluent treatment. J Ind Eng Chem 128:196–208. https://doi.org/10.1016/-j.jiec.2023.07.048.
37. Yu Y, Zhou X, Jiang Y, Ji Y, Fang X, Zhang Y (2023) Synthesis of eco-friendly lignin-betaine and its application for dye wastewater treatment. Ind Crops Prod 192:116014. https://doi.org/10.1016/-j.indcrop.2022.116014.

38. Mansoori S, Davarnejad R, Matsuura T, Ismail AF (2020) Membranes based on non-synthetic (natural) polymers for wastewater treatment. Polym Test 84:106381. https://doi.org/10.1016/-j.polymertesting.2020.106381.
39. Cambie D, Bottecchia C, Straathof NJ, Hessel V, Noel T (2016) Applications of continuous-flow photochemistry in organic synthesis, material science, and water treatment. Chem Rev 116:10276–10341. https://doi.org/10.1021/acs.chemrev.5b00707.
40. Buglioni L, Raymenants F, Slattery A, Zondag SD, Noel T (2021) Technological innovations in photochemistry for organic synthesis: flow chemistry, high-throughput experimentation, scale-up, and photoelectrochemistry. Chem Rev 122:2752–2906. https://doi.org/10.1021/-acs.chemrev.1c00332.
41. Mahmoodi NM, Taghizadeh A, Taghizadeh M, Abdi J (2019) In situ deposition of Ag/AgCl on the surface of magnetic metal organic framework nanocomposite and its application for the visible-light photocatalytic degradation of Rhodamine dye. J Hazard Mater 378120741. https://doi.org/10.1016/-j.jhazmat.2019.06.018.
42. Ranjbari S, Ayati A, Tanhaei B, Al-Othman A, Karimi F (2022) The surfactant-ionic liquid bi-functionalization of chitosan beads for their adsorption performance improvement toward Tartrazine. Environ Res 204:111961. https://doi.org/10.1016/j.envres.2021.111961.
43. Elgarahy AM, Elwakeel KZ, Mohammad SH, Elshoubaky GA (2020) Multifunctional eco-friendly sorbent based on marine brown algae and bivalve shells for subsequent uptake of Congo red dye and copper(II) ions. J Envirom Chem Eng 8:103915. https://doi.org/10.1016/-j.jece.2020.103915.
44. Aqdam SR, Otzen DE, Mahmoodi NM, Morshedi D (2021) Adsorption of azo dyes by a novel bio-nanocomposite based on whey protein nanofibrils and nano-clay: Equilibrium isotherm and kinetic modelling. J Coll Inter Sci 602:490–503. https://doi.org/10.1016/-j.jcis.2021.05.174.
45. Ren J, Li M, Wang X, Li R, Wang H, Yang W (2022) Adsorption behaviors of dyes on a biodegradable gelatin/chitosan/β-cyclodextrin hydrogel from an aqueous solution. Coll Polym Sci 300:785–800. https://doi.org/10.1007/s00396-022-04988-w.
46. Ma S, Xu K, Zhu X, Liu M, Xu Y, Luo K (2024) Hierarchical mesoporous TiO2/starch-based microparticles used as an efficient and reusable adsorbent for removal of water-soluble dye. Inter J Biol Macromol 274 133380. https://doi.org/10.1016/j.ijbiomac.2024.133380.
47. Al-Raimi DS, Alghanmi RM, Aljeddani GS, Hamouda RA (2025) Eco-Friendly Synthesis of Silver–Cellulose Nanocomposite Adsorbent from Agricultural Residues for Binary Dye System Remediation. Polym 17:2555. https://doi.org/10.3390/polym17182555.
48. Alenezi H, Gad ES, Albassami NA, Alatawi IS, Alshareef SA, Aljowni MA, El-Din B, Saleh AK (2025) Development of oxidized sodium alginate/silica hybrid as efficient adsorbent for anionic and cationic dyes: mechanism and thermodynamic studies. Biomass Conv Bioref 15:18247–18261. https://doi.org/10.1007/s13399-024-06329-z.

49. Oruganti RK, Katam K, Show PL, Gadhamshetty V, Upadhyayula VKK, Bhattacharyya D (2022) A comprehensive review on the use of algal-bacterial systems for wastewater treatment with emphasis on nutrient and micropollutant removal. Bioeng. 13(4):10412–10453. https://doi.org/10.1080/-21655979.2022.2056823
50. Jacob J, Haponiuk JT, Thomas S, Peter G, Gopi S (2018) Use of ginger nanofibers for the preparation of cellulose nanocomposites and their antimicrobial activities. Fibres 6:79. https://doi.org/-10.3390/fib6040079.
51. Shankar S, Kasapis S, Rhim JW (2018) Alginate-based nanocomposite films reinforced with halloysite nanotubes functionalized by alkali treatment and zinc oxide nanoparticles. Inter J Biol Macromol 118:1824–1832. https://doi.org/10.1016/j.ijbiomac.2018.07.026.
52. Zhou X, Jin C, Liu G, Wu G, Huo S, Kong Z (2021) Functionalized lignin-based magnetic adsorbents with tunable structure for the efficient and selective removal of Pb (II) from aqueous solution. Chem Eng J 420:130409. https://doi.org/10.1016/j.cej.2021.130409.
53. Balakrishnan A, Appunni S, Chinthala M, Jacob MM, Vo DVN, Reddy SS, Kunnel ES (2023) Chitosan-based beads as sustainable adsorbents for wastewater remediation: a review. Environ Chem Lett 21:1881–1905. https://doi.org/10.1007/s10311-023-01563-9.
54. Luo Y, Lin J, Wang X, Yeerken A, Ma H (2023) Study on Flocculation Performance of New Cationic Starch-Based Sludge Wastewater Flocculant. Starch-Stake 75:2200226. https://doi.org/10.1002/-star.202200226.
55. Singh P, Kaur G, Singh A, Kaur P (2023) Starch based bio-nanocomposite films reinforced with montmorillonite and lemongrass oil nanoemulsion: development, characterization and biodegradability. J Food Meas Charac 17:527–545. https://doi.org/10.1007/s11694-022-01635-4.
56. Nur Hanani ZA, Roos YH, Kerry JP (2014) Use and applica tion of gelatin as potential biodegradable packaging materials for food products. Inter J Biol Macromol 71:94–102.
57. Angellier-Coussy H, Gastaldi E (2012) Protein/clay nano-biocomposites. In Environmental silicate nano-biocomposites. 323–343. London: Springer London.
58. Koshy RR, Reghunadhan A, Mary SK, Pothen LA, Thomas S (2022) MgONP/Chitin nanowhisker-based hybrid filler bound soy protein thin films for bioactive packaging applications. Inter J Food Sci Technol 57:5650–5662. https://doi.org/10.1111/ijfs.15805.
59. Rabee M, Elmogy SA, Morsy M, Lawandy S, Zahran MAH, Moustafa H (2023) Biosynthesis of MgO nanoparticles and their impact on the properties of the PVA/gelatin nanocomposites for smart food packaging applications. ACS Appl Bio Mater 6:5037–5051. https://doi.org/10.1021/-acsabm.3c00723.
60. Sharma T, Kaur G, Singh A, Kaur P, Dar BN, Kaur A (2023) An emerging sustainable approach for development and characterization of gluten-based nanocomposite films reinforced with starch nanocrystals in conjugation with chitosan. Sustain Chem Pharm 36:101338. https://doi.org/10.1016/j.scp.2023.101338.

61. Bhavya EP, Raman M (2025) κ-Carrageenan based bio-nanocomposite films containing soy protein and nanocellulose: mechanical and thermal characteristics J Appl Phycol 1–14. https://doi.org/10.1007/s10811-025-03531-y.
62. Panthi KP, Shahi DK, Sharma ML, Li Z, Pandey LM, Joshi MK (2025) Gluten-based composite film for smart food packaging applications. Food Bioproc Technol 18:2882–2898. https://doi.org/10.1007/s11947-024-03642-3.
63. Ghanavati Nasab S, Semnani A, Teimouri A, Kahkesh H, Momeni Isfahani T, Habibollahi S (2018) Removal of Congo red from aqueous solution by hydroxyapatite nanoparticles loaded on zein as an efficient and green adsorbent: response surface methodology and artificial neural network-genetic algorithm. J Polym Environ 26:3677–3697. https://doi.org/10.1007/s10924-018-1246-z.
64. Ren J, Wang X, Zhao L, Li M, Yang W (2021) Effective removal of dyes from aqueous solutions by a gelatin hydrogel. J Polym Environ 29:3497–3508. https://doi.org/10.1007/-s10924-021-02136-z.
65. Vadivel M, Jayakumar S, Philip J (2022) Rapid removal of rhodamine dye from aqueous solution using casein-surfactant complexes: role of casein-surfactant interaction. J Dis Sci Technol 43:928–943. https://doi.org/10.1080/01932691.2020.1845963.
66. Revadekar CC, Godiya CB, Park BJ (2024) Novel soy protein isolate/sodium alginate-based functional aerogel for efficient uptake of organic dye from effluents. J Environ Manag 352:120011. https://doi.org/10.1016/j.jenvman.2023.120011.
67. Abu Elella MH, Aamer N, Abdallah HM, Lopez-Maldonado EA, Mohamed YM, El Nazer HA, Mohamed RR (2024) Novel high-efficient adsorbent based on modified gelatin/montmorillonite nanocomposite for removal of malachite green dye. Sci Rep 14:1228. https://doi.org/10.1038/-s41598-024-51321-2.
68. Peng Z, Xin Y, Dong X, Quan Z (2014) Facile synthesis of CoAl-LDH/$MnO_2$ hierarchical nanocomposites for high-performance supercapacitors. Ceram Int 40:2115–2120. https://doi.org/10.1016/j.ceramint.2013.07.127.
69. Elhalil A, Farnane M, Machrouhi A, Mahjoubi FZ, Elmoubarki R, Tounsadi H, Mohamed A, Barka N (2018) Effects of molar ratio and calcination temperature on the adsorption performance of Zn/Al layered double hydroxide nanoparticles in the removal of pharmaceutical pollutants. J Sci Adv Mater Dev 3:188–195. https://doi.org/10.1016/-j.jsamd.2018.03.005.
70. Jiang H, Katsumata K, Hong J, Yamaguchi A, Nakata K, Terashima C, Matsushita N, Miyauchi M, Fujishima A (2018) Photocatalytic reduction of $CO_2$ on $Cu_2O$-loaded Zn-Cr layered double hydroxides. Appl Catal B Environ 224:783–790. https://doi.org/10.1016/-j.apcatb.2017.11.011.
71. N Baig, Sajid M (2017) Applications of layered double hydroxides based electrochemical sensors for determination of environmental pollutants A review, Trends Environ Anal Chem 16:1–15. https://doi.org/10.1016/j.teac.2017.10.003.

72. Prasanna SV, Kamath PV (2009) Anion-Exchange Reactions of Layered Double Hydroxides Interplay between Coulombic and H-Bonding Interactions. Ind Eng Chem Res 48:6315–6320. https://doi.org/10.1021/ie9004332.
73. Nait-Merzoug A, Guellati O, Djaber S, Habib N, Harat A, El-Haskouri J, Begin D, Guerioune M (2021) Ni/Zn layered double hydroxide (LDH) micro/nanosystems and their azorubine adsorption performance. Appl Sci 11(19):8899. https://doi.org/10.3390/app11198899.
74. Swain SK, Barik S, Pradhan GC, Behera L (2018) Delamination of Mg-Al layered double hydroxide on Starch: Change in Structural and Thermal properties. Polym PlastTech Eng 57:1585−1591. https://doi.org/10.1080/03602559.2017.1410844.
75. Mishra G, Dash B, Pandey S (2018c) Layered double hydroxides: a brief review from fundamentals to application as evolving biomaterials. Appl Clay Sci 153:172–186. https://doi.org/10.1016/-j.clay.2017.12.021.
76. Grzegorska A, Wysocka I, Głuchowski P, Ryl J, Karczewski J, Zielinska-Jurek (2022) A Novel composite of Zn/Ti-layered double hydroxide coupled with MXene for the efficient photocatalytic degradation of pharmaceuticals. Chemosphere 308:136191. https://doi.org/10.1016/-j.chemosphere.2022.136191.
77. Kawasumi M (2004) The discovery of polymer-clay hybrids. J Polym Sci Part A Polym Chem 42:819–824. https://doi.org/10.1002/pola.10961.
78. SM Lee, D Tiwari (2012) Organo and inorgno-organo-modified clays in the remedation of aqueous solutions: An overview. Appl Clay Sci 59:84–102. https://doi.org/10.1016/-j.clay.2012.02.006.
79. Nazir MS, Kassim MHM, Mohapatra L, Gilani MA, Raza MR, Majeed K (2016) Characteristic properties of nanoclays and characterisation of nanoparticulates and nanocomposites. In Nanoclay Reinf Polym Compo 35−55. https://doi.org/10.1007/978-981-10-1953-1_2
80. Atterbury RJ, Connerton PL, Dodd CE, Rees CE, Connerton IF (2003) Application of host-specific bacteriophages to the surface of chicken skin leads to a reduction in recovery of Campylobacter jejuni. Appl Environ Microbiol 69:6302–6306. https://doi.org/10.1128/-AEM.69.10.6302-6306.2003.
81. Chequer FMD, Lizier TM, de Felicio R, Zanoni MVB, Debonsi HM, Lopes NP, Marcos R, de Oliveira DP (2011) Analyses of the genotoxic and mutagenic potential of the products formed after the biotransformation of the azo dye Disperse Red Toxicol in Vitro 25:2054–2063. https://doi.org/10.1016/j.tiv.2011.05.033.

# Chapter- 2

## *Preparation, structural characterization, and performance assessment of SPI/Mg–Al LDH bionanocomposite films*

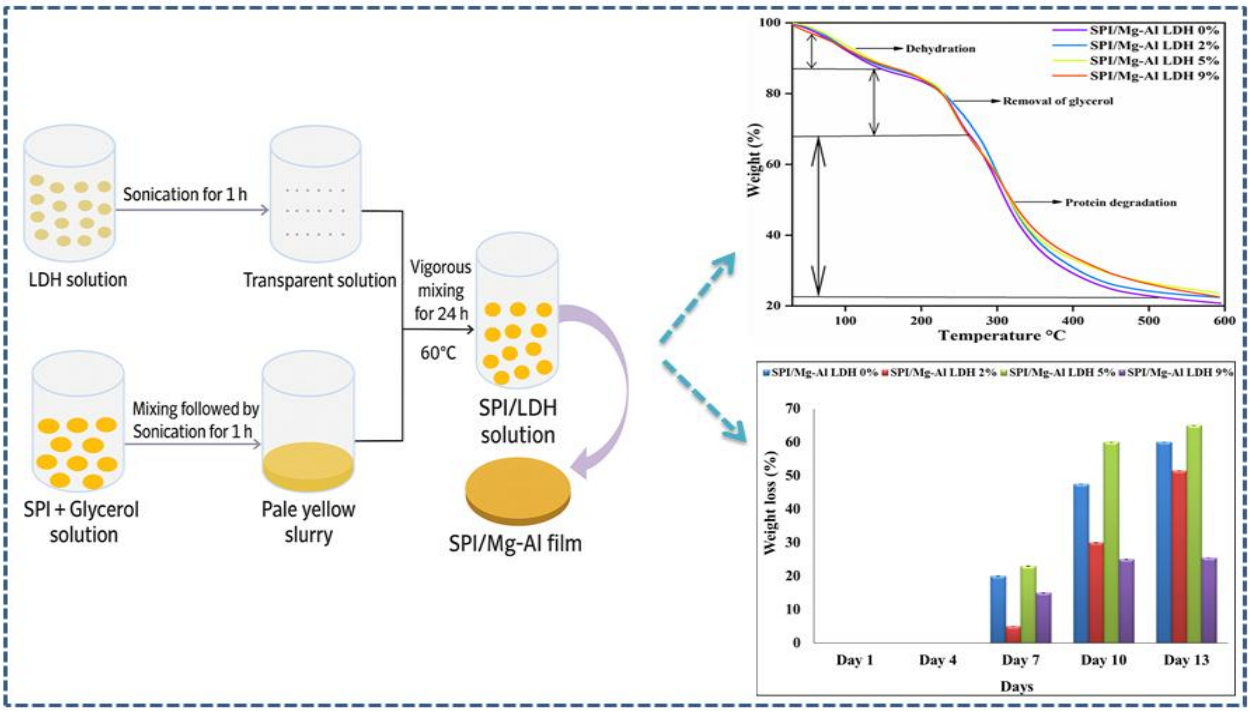


### Schematic Outline:

In this chapter, SPI/Mg–Al LDH bionanocomposite films were prepared by solution casting method. The thermal behaviour of the synthesized films was investigated. Biodegradation studies indicated that approximately 70% of the film containing 5% Mg–Al LDH underwent degradation in normal soil within a period of 14 days.

## 2.1 Introduction

Bionanocomposites (BNCs) are rapidly emerging as eco-friendly bioplastics during the recent decades in order to minimize hydrocarbon-based plastic wastes. BNCs are also referred to as 'biocomposites', 'green composites', and 'biohybrids' as these are derived from renewable bioresources. Bionanocomposites are regarded as the new generation nanocomposites (NCs). Basically, BNCs are a group of nanostructured hybrid materials developed mainly by the applied aspects of nano, material and life sciences [1]. Biopolymers such as starch materials along with other homo and heteropolysaccharides, proteins, chitosan, lipids are being frequently used in making various bioplastics which potentially offer a better and cost-effective solution for both packaging and waste disposal. Biopolymer-based materials are significantly gaining importance due to their biodegradability, and compatibility with the pharmaceuticals, processed food products and diverse agricultural produce [2]. As reported in the literature, bio-based packaging materials find multiple applications with regard to containment, food safety, maintaining sensory quality, and displaying product details for consumers. A number of different proteins having distinct biochemical properties namely serum albumin, egg white, collagen, gelatin, myofibrils, casein, whey protein, wheat gluten, corn zein and some other proteins from plant sources such as soybean, sesame, peanut, cottonseed, sunflower and rice bran were used in preparing the BNCs as potential film-forming materials [3,4].

Proteins are linear hetero-biopolymers, and extremely diverse with regard to three-dimensional (3-D) structures and biological activities. The presence of different functional groups in the constituent amino acid residues of the individual polypeptide chains can form bonds at different positions of a particular protein [5]. The secondary, tertiary and quaternary structures of proteins are involved in various types of intra- and intermolecular interactions [6]. All these attributes could potentially be exploited in preparing the bioplastics with desirable physico-chemical properties. Usually, films, casings and coatings made of proteins and polysaccharides effectively act as barriers against oxygen ($O_2$), carbon dioxide ($CO_2$) and low polarity small molecules. Protein films show relatively lower $O_2$ and $CO_2$ permeability as compared to other biopolymers [7,8]. For producing protein-based films with suitable mechanical properties, dissolution-solvent evaporation or thermo-mechanical methods are adopted [9].

Soy proteins are extracted from soybean seeds and composed of a mixture of albumins and globulins representing mostly storage proteins with globular structure, consisting of 7S (β-conglycinin) and 11S (glycinin) subunits [10]. Aspartic acid (Asp) and Glutamic acid (Glu) predominantly occur in soy proteins [11]. Commercially, three different forms of soy proteins

namely soy flour (SF), soy protein concentrate (SPC) and soy protein isolate (SPI) having 54%, 66%, 90% protein contents on a moisture-free basis, respectively [12]. SPI represents a purified form of soy protein made from defatted soy flour [13]. It shows a higher film-forming ability because of more protein content. Importantly, SPI is a preferred biopolymer in preparing softer, transparent and flexible films [14].

Currently, soy protein isolates (SPIs) are significantly gaining importance due to multiple uses in non-formaldehyde wood adhesives, agriculture, bio-based films which are biodegradable and exhibit barrier properties effectively to oxygen, aromas, and lipids under low to intermediate moisture conditions [15-18]. SPIs also have some shortcomings; for example, in native form, they show poor heat resistance limiting their uses for product developments in many sectors [19]. Because of inherent hydrophilicity, criteria of their required mechanical and/or water vapour barrier properties are compromised. Despite of some drawbacks, many laboratories use eco-friendly SPIs for preparing BNCs since they are suitable in terms of regeneration, biocompatibility, and biodegradability. This explains SPIs are used in making materials such as hydrogels, adhesives, plastics, films, coatings and emulsifiers [20,21].

Currently polymer-clay nanocomposites are gaining importance because of improved thermal and physical properties. They have become a substitute for conventional plastics and biopolymer-based composites. Moreover, such types of materials are relatively non-hazardous and easily prepared in a cost-effective manner [22]. Synthetic inorganic materials are being used in preparing various types of composites. Out of several types of lamellar solids, layered double hydroxides (LDH) represent a class of nano-fillers for biopolymers. These anionic clays could intercalate and/or exfoliate into polymer matrices [23,24,25]. LDH are natural minerals, formed as by-products of the metabolism of certain bacteria and also from corrosion of metal objects. These layered crystal structures widely vary with regard to nature of cations, M(II)/M(III) molar ratios, and the type of exchangeable anions [26]. These brucite type layers comprising divalent and trivalent cations are represented by the general formula: $[(M^{+2})_{1-x}(M^{+3})_x(OH)_2]^{x+}(A^{n-}_{x/n}).mH_2O$, where $M^{2+}$ is divalent cation (e.g., $Ca^{2+}$, $Mg^{2+}$, $Sr^{2+}$ etc.); $M^{3+}$ is trivalent cation (e.g., $Al^{3+}$, $V^{3+}$, $Cr^{3+}$ etc.); and $An^-$ is the exchangeable anion. Unlike layered silicates, the hydroxide layers have a positive surface charge counterbalanced by anions which remain associated with polar water molecules between the adjacent layers [27,28]. Such edge-sharing octahedral structures accommodate the metal cations in the centres; six surrounding $OH^-$ ions for each cation remain pointed towards the corners in the sheets [24]. Uniform distribution of the $M^{2+}$ and $M^{3+}$ cations are considered to be important structural characteristics

of LDH materials. The interlayer anion exchangeable capability of LDHs serves as inorganic matrices for encapsulating functional biomolecules with a negative charge in aqueous media. Significant progress has been made with regard to the synthesis of innovative LDH materials. Such materials have new compositions and characteristic morphologies allowing improved and wider applications in many areas [26]. These LDH materials were prepared by a number of possible compositions and metal-anion combinations. Additionally, they exhibit some other characteristics in terms of biocompatibility, high chemical stability, pH dependent solubility, [29]. LDHs show several desirable properties like enhanced, thermostability, antimicrobial and adsorptive properties. These are extensively used in gene therapy. They also act as catalysts, acid residue scavengers, ion-exchange materials, and are useful in drug delivery and as additives to plastics [30-33]. The general structure of layered double hydroxide is already shown in **Scheme 1.3**.

Here, we report on SPI-Mg/Al LDH-based bionanocomposite films as such types of protein/LDH-based recyclable materials were not reported earlier. The major focus was to study the effects of synthesized Mg-Al LDH on thermal stability, mechanical strength, crystallinity, and microstructure of SPI-based bionanocomposite films. The aim was to develop biodegradable films mostly for packaging purposes.

## 2.2 Experimental

### 2.2.1 Chemicals

Soy protein isolate (SPI, 90% total protein content) was purchased from AS-IT-IS, Medizen Pvt. Ltd. (Bengaluru, India). Glycerol and Aluminium nitrate nonahydrate [$Al(NO_3)_3.9H_2O$] were taken from Qualigens Fine Chemicals, India. Magnesium nitrate hexahydrate [$Mg(NO_3)_2.6H_2O$], and Sodium Hydroxide (NaOH) were procured from Loba Chemie, India. Sodium Carbonate anhydrous ($Na_2CO_3$) was purchased from Central Drug House (P) Ltd. (New Delhi, India). Deionized water was purchased from Organo Biotech Laboratories Pvt. Ltd. (New Delhi, India).

**Instrumentation**

The thickness was measured with a micrometer thickness gauge (L&W Micrometer). Four measurements were taken at random locations for each film. The average of four measurements represents the thickness of each film.

Powdered LDH and SPI-based films were examined by FTIR analyses using a Shimadzu IRTracer-100 Fourier Transform Infrared Spectrophotometer with ATR mode. The wavelength range was set at 400-4000 $cm^{-1}$, with a scan range of 16 and a spectral resolution of 2 $cm^{-1}$.

XRD pattern of powdered LDH and film samples was obtained by using a PANalytical-Xpert-Pro diffractometer with Cu K-α (λ = 0.154 nm) radiations. The XRD pattern was taken at 2θ = 5°–65° (with step size = 0.01°).

The cross-sectional morphology of the film specimens was examined using FE-SEM (Carl Zeiss Sigma 500). A cross-sectional area of each film was taken. For imaging, the film samples were cut into 1 cm×1 cm pieces and sputter-coated with gold layer. The surface morphology of Mg-Al LDH was studied.

The L & W Tensile Tester was used to determine the tensile strength (TS) and elongation at break (EB) of the film samples based on the method IS 1060-1 (Indian Standard, Part 1). Each film sample was cut into rectangular strips (11 cm × 1.5 cm). Samples were held in place between the grips. The initial grip separation was kept at 90 mm with a 20 mm/min speed. Each sample was measured in triplicate to get the average value.

The thermogravimetric analyzer was used to test the thermal stability of the film samples and powdered LDH (STA 6000 Perkin Elmer). MgAl powder (approximately 20 mg of each sample was taken for analysis). The heating rate was kept at 10 °C/min from 10°C/min from 28°C to 600°C under a nitrogen atmosphere.

### 2.2.3. Synthesis of Mg-$CO_3$-Al layered double hydroxide (LDH)

The synthesis of LDH was carried out by a simple co-precipitation technique [34]. The Mg/Al ratio was kept at 2:1. An alkaline solution having 3.5 M NaOH and 0.94 M $Na_2CO_3$ was prepared in deionized water. A thoroughly mixed metal solution of 1.0 M $Mg(NO_3)_2.6H_2O$ and 0.5 M $Al(NO_3)_3.9H_2O$ was dropwise added to the alkaline solution and the reaction aggregates were kept on vigorous stirring for 24 h at 60°C. The resulting white slurry was centrifuged at 25°C, the precipitate was collected and dried at 110°C in an oven for 3-4 h. The dried samples were stored in glass vials at room temperature for further use.

### 2.2.4. Preparation of SPI/Mg-Al LDH films

For film preparation, the solution casting method was followed as shown in **Fig. 2.1**. 4.0 g of SPI was dissolved in 40 mL of deionized water, followed by addition of glycerol (30% w/w of SPI weight) at ambient temperature. The pH of this solution was adjusted slightly alkaline by dropwise addition of 1 M NaOH with continuous stirring for 1 h in order to prepare only

SPI-based film. LDH suspensions at varying concentrations i.e., 0%, 2%, 5% and 9% (w/w of SPI weight) were prepared by dispersing in 20 mL of deionized water. Individual LDH suspensions and SPI solutions were magnetically stirred for 1 h, followed by ultra-sonication for the same duration. To prepare composite film solution, the dispersed LDH suspension was added to the SPI solution, and the reaction mixture was stirred overnight at 60°C. The film-forming solutions were evenly spread onto a Teflon-coated pan (19.5 cm×19.5 cm) and allowed to dry for 2 days at 20°C. The films were peeled off and stored at 25±3°C for further characterization.

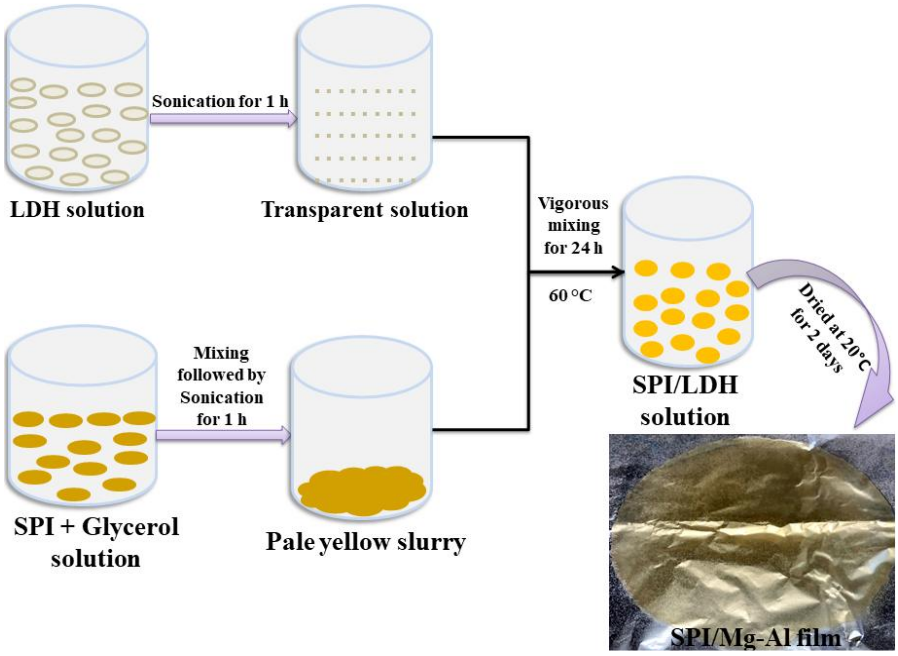


**Fig. 2.1** Schematic representation of preparation of SPI/Mg-Al LDH films

## 2.2.5. Biodegradability test

The composting method was adopted for biodegradability test using both non-sterile and sterile soil samples. The soil samples were uniformly mixed with grasses, cow manure and water (pH ~7.5); the sterile soil was produced by heating in a muffle furnace at 550°C for 3 h [35]. The non-sterile soil sample was conditioned at 55°C to promote the growth of thermophilic microorganisms [36]. For biodegradability test, approx. 0.2 g of the film sample was taken and completely buried in 60 g of soil sample at ambient temperature (35±2°C). The soil-treated film samples were taken out and oven-dried at 40°C for 4 h; adhering soil particles were removed prior to taking their weights. This test was repeated with a gap of 3 days and continued

upto Day 14. Each test was done in triplicate to get the average value. The weight loss (%) of film sample was calculated by using the following equation:

$$\text{Weight loss (\%)} = \frac{\text{initial weight} - \text{final weight}}{\text{initial weight}} \times 100$$

## 2.3. Results and discussion

### 2.3.1. Characterization

The thickness of SPI/Mg-Al based BNCs with varying LDH concentrations i.e., 0%, 2%, 5% and 9% were found to be 245±6.7, 228±8.4, 262±10.0 and 260±11.0 µm, respectively. The data suggested that LDH had a non-significant impact on the thickness of the prepared SPI-based films **Table 2.1**. There was a significant difference ($p$ = 0.001). Very likely, it could be due to the replacement of water molecules by LDH particles once they were inserted into the SPI domains [16,37]. Pristine SPI films were found to be flexible, transparent, and pale-yellowish; whereas, the SPI/Mg-AL LDH films were distinctly yellowish and translucent in appearance mostly contributed by Mg-Al LDH concentrations.

**Table 2.1** Physical and mechanical properties of film samples (mean±standard deviation)

| Film samples | Thickness (µm) | Tensile Strength (KNm/g) | Elongation at break (%) |
|---|---|---|---|
| **SPI/Mg-Al LDH 0%** | 245±6.7 | 2.12±0.25 | 13.2±3.48 |
| **SPI/Mg-Al LDH 2%** | 228±8.4 | 1.60±0.15 | 6.9±5.46 |
| **SPI/Mg-Al LDH 5%** | 262±10.0 | 1.64±0.08 | 5.6±0.74 |
| **SPI/Mg-Al LDH 9%** | 260±11.0 | 1.58±0.06 | 3.5±0.4 |

ATR-FTIR analysis was used to investigate distinct functional groups present in the prepared materials as shown in **Fig. 2.2**. The spectra of Mg-Al LDH exhibited characteristic absorption peaks at 3386, 1641, and 1351 $cm^{-1}$ corresponding to ─OH stretching vibrations, bending vibrations of the interlayered water molecules and asymmetric stretching vibrations of the interlayered $CO_3^{2-}$ anions, respectively [38,39]. The lower frequency region of 946–446 $cm^{-1}$ corresponded to stretching modes of the metal-oxygen bond [43]. The absorption peak at 2347 $cm^{-1}$ corresponds to stretching vibrations probably due to the presence of atmospheric $CO_2$. In

the pristine SPI, characteristic absorption peaks at 1630, 1519, and 1233 $cm^{-1}$ corresponded to amide I C=O stretching, amide II N-H bending, and amide III C─N and N─H stretching, respectively [40]. The peaks at 3272, 2926, and 1037 $cm^{-1}$ represented ─OH vibrations, ─$CH_2$ asymmetric stretching, and C─O stretching of glycerol [41]. In the SPI based films with 2%, 5%, and 9% LDH loadings, the absorption peaks at the lower frequency region of 946–446$cm^{-1}$ were observed indicating the presence of Mg-Al LDH in the SPI matrix, and provided supporting evidence regarding formation of SPI/Mg-Al LDH bionanocomposites. LDH-specific absorption peaks of SPI/Mg-Al LDH 5–9% films were only slightly visible at the lower frequency region; whereas, the corresponding peaks in the case of 2% LDH loading were invisible. Probably, it was due to interactions between SPI and LDH in the films.

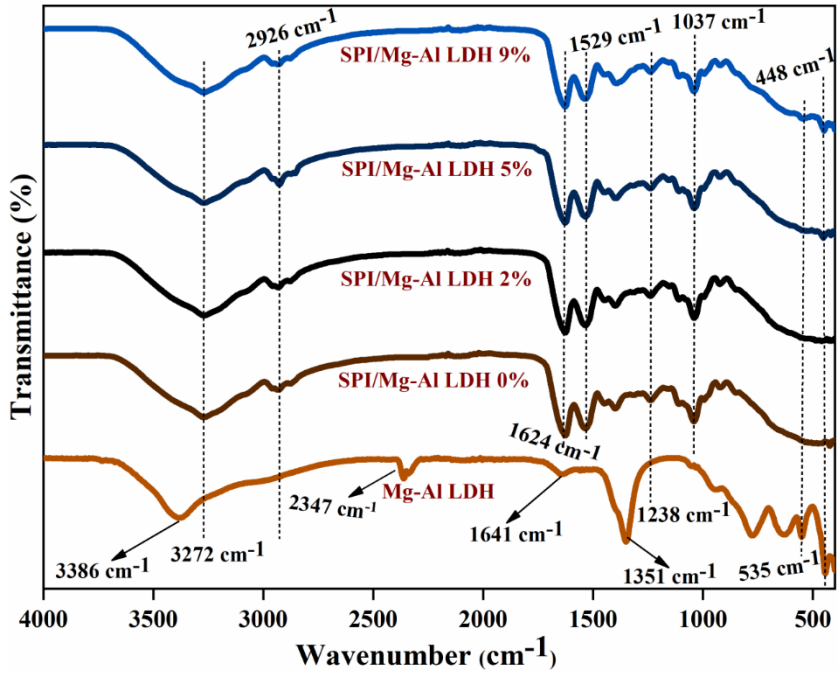


**Fig. 2.2** FTIR spectra of Mg-Al LDH and SPI-based films

XRD is a powerful technique commonly used to detect the intercalating and exfoliating properties of sheet-like LDH structures. The XRD patterns of Mg-Al LDH and SPI-based films are shown in **Fig. 2.3a and b**. The synthesized Mg-Al LDH material exhibited distinctive peaks at 2θ=11.6°, 23.4°, 34.6°, and 35.5° which corresponded to the reflections (0,0,3), (0,0,6), (0,0,9), and (0,1,2), respectively clearly indicating the material's crystalline structure [42]. The pristine SPI film showed a characteristic amorphous protuberance at 2θ=8.8° and 19.6° corresponding to the α-helix and β-sheets of SPI secondary structure, respectively [43]. The diffractograms of SPI-based films with 5%, and 9% LDH loadings indicated prominent peaks

of Mg-Al LDH at 2θ=11.6°, 23.4°, and 34.6°. The increase in intensity was found to be dependent on the concentration of Mg-Al LDH. Apparently, the SPI matrix had no considerable effect on crystallinity of the LDH as its layered structure remained intact in the prepared BNCs. In contrast, such peaks were absent in 2% SPI/Mg-Al LDH. This observation clearly suggested that LDH particles were uniformly dispersed into the SPI matrix at a lower concentration indicating reduced crystallinity of LDH particles. At higher LDH concentrations i.e., 5% and 9%, the SPI polypeptide chains possibly assumed altered conformations due to agglomerated LDH particles. The latter could regain their crystallization ability as evident from appearance of the distinct diffraction peaks [44,45].

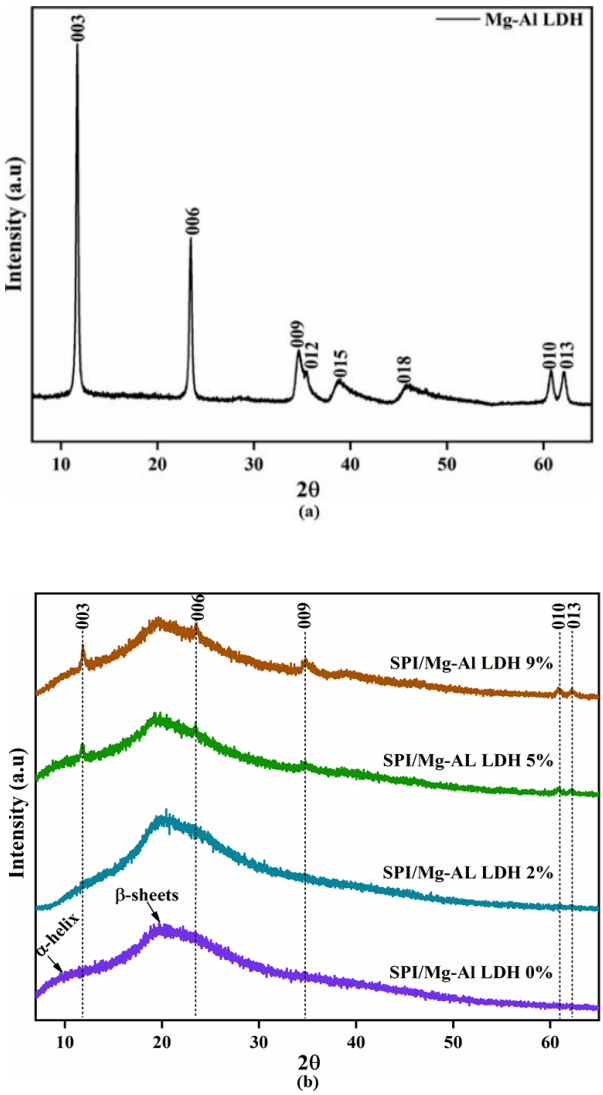


**Fig. 2.3** XRD spectra of **(a)** Mg-Al LDH, and **(b)** SPI-based films

Microstructures of the synthesized Mg-Al LDH and SPI-based films were examined by FE-SEM imaging as shown in **Fig. 2.4**. Surface morphology of the former revealed formation of an asymmetric mass of small particles. The cross-sectional view of SPI-based film with 0% LDH loading showed the presence of coarse and rough surfaces with multiple holes [46]. An increase in concentration of Mg-Al LDH from 2% to 9% facilitated more agglomeration which could alter the nature of interfacial interactions. This result was consistent with the XRD and FTIR data of the study.

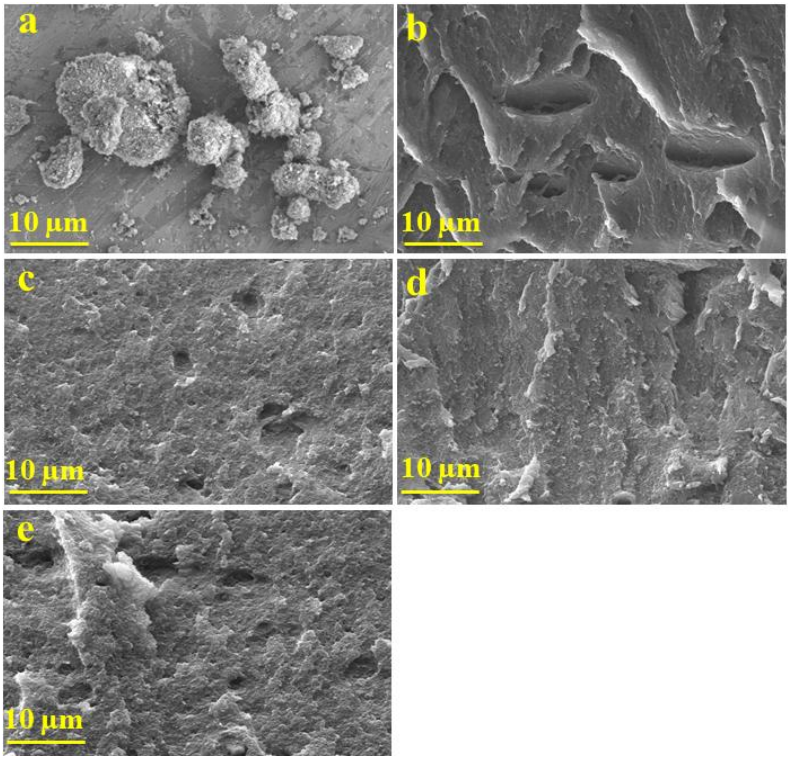


**Fig. 2.4** FE-SEM image of **(a)** Mg-Al LDH, Cross-section view of **(b)** SPI/Mg-Al LDH 0%, **(c)** SPI/Mg-Al LDH 2%, **(d)**SPI/Mg-Al LDH 5%, and **(e)** SPI/Mg-Al LDH 9%

The effect of Mg-Al LDH on the mechanical properties of prepared SPI-based films was studied as shown in **Table 2.1** and **Fig. 2.5**. There was a significant difference ($p$ = 0.000). In the case of 0% to 2% LDH loading, the tensile strength (TS) got considerably reduced from 2.12 KNm/g to 1.60 KNm/g; whereas, 2% to 5% loading led to only a slight increase of TS i.e., 1.60 KNm/g to 1.64 KNm/g. Further increase in the concentration of Mg-Al LDH resulted in the decrease of tensile strength (1.58 KNm/g). Possibly, the addition of Mg-Al LDH caused weakening of hydrogen bonds present in protein structure which in turn showed plasticizing effect in terms of their strength, stiffness with higher strain at break. The agglomeration also

led to a decrease in tensile strength. Usually, inorganic/organic composites with inorganic fillers were known to be stiff and more brittle. Therefore, decrease in tensile strength with increasing LDH loading can be attributed to changes in filler dispersion and polymer–filler interactions within the SPI matrix. At lower LDH concentrations, uniform dispersion facilitates efficient stress transfer and maintains mechanical strength. However, higher LDH loading promotes particle agglomeration and structural heterogeneity, creating stress concentration points that weaken the films. Elongation at break also reduced with an increase in Mg-Al LDH concentration. The mechanical properties of the BNCs of the study were more or less consistent with the earlier reports. According to the studies on LDH-based composites, LDH component was recognized as stress concentrators [47,48].

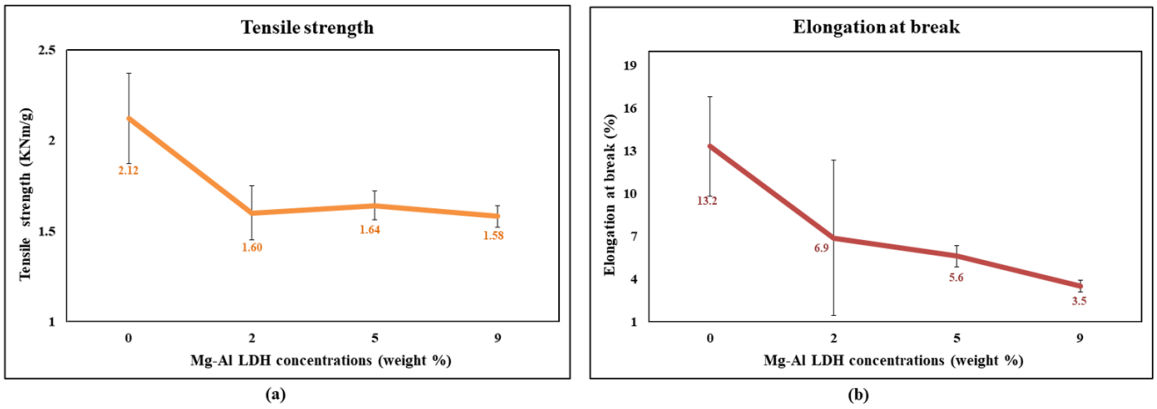


**Fig. 2.5** Effect of Mg-Al LDH concentration on **(a)** tensile strength, and **(b)** elongation at break (mean± standard deviation)

Thermal stability of SPI-based films was analysed by thermogravimetric analysis (TGA) shown in **Fig. 2.6**. The thermogram of LDH showed a distinct weight loss curve reflecting various processes occurring at different ranges of temperature: a) evaporation of interlayer water molecules from 28 to 231°C, b) elimination of interlayer $CO_3^{2-}$ ions and/or dehydroxylation from 231 to 412°C and c) formation of metal oxides, decarbonatation and dehydroxylation from 412 to 600°C [42]. The weight loss of pristine SPI at different temperatures shown in the thermogram was due to dehydration (28–143°C), removal of glycerol (143–270°C) and degradation of protein structure (270–493°C) [49]. The weight loss curves of the SPI-based films with 2%, 5% and 9% LDH loadings exhibited an elevation in residual weight with drop-in rate of degradation. Stability of the BNCs at higher temperatures was due to milder degradation of the SPI matrix impacted by the barrier effect of the exfoliated LDH sheets. Interactions between SPI and nano-filler contributed to the better thermostability of SPI/Mg-Al LDH composites than pristine SPI.

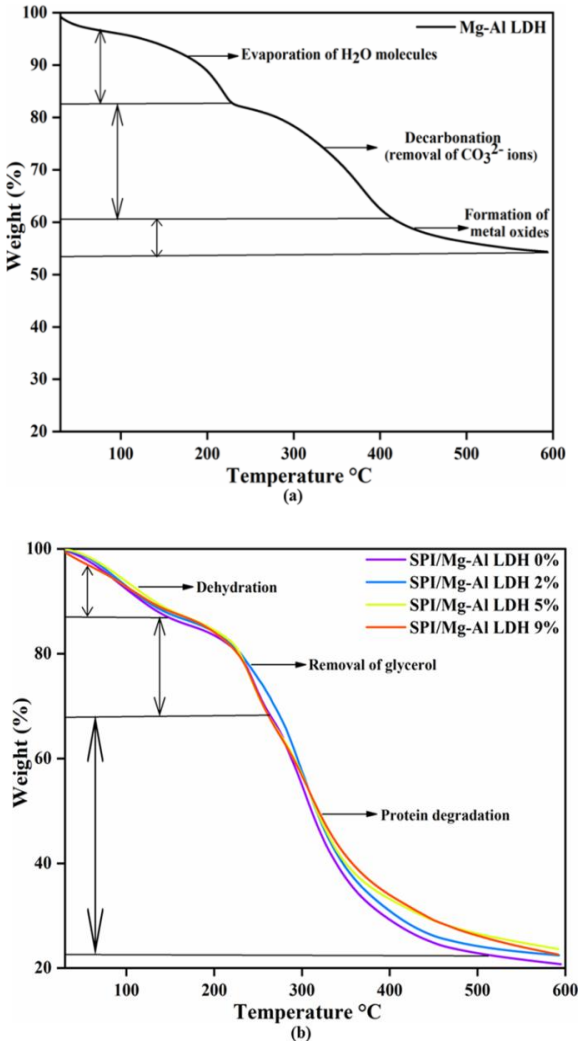


**Fig. 2.6** TGA of **(a)** Mg-Al LDH, and **(b)** SPI-based films

## 2.3.2. Biodegradability Test

Both non-sterile and sterile soil samples were used for biodegradability test as presented in Fig. **Fig. 2.7**. The findings of the biodegradability test revealed that the extent of degradation remained negligible in the case of sterile soil in comparison to non-sterile soil samples as shown in **Fig. 2.8**, also refer to **Fig. 2.9**. There was a significant difference ($p = 0.000$). The data clearly indicated that degrading properties of the sterile soil was markedly affected due to lack of microorganisms, moisture and other necessary soil components. In contrast, various factors like moisture, microbial loads, pH and organic matters either singly or in combination effectively contributed to process of degradation of the buried films. Loss of weight remained an indicator of degradation. Weight loss was noticed on the eighth day after burial in non-sterile soil, and the process continued over time. The overall weight loss percent for the SPI-

based films with varying LDH loadings as mentioned earlier were found to be 60%, 51.5%, 65%, and 25.5%, respectively. The weight loss percentage was maximum in the case of 5% LDH loading which could be a preferred material over others in terms of biodegradability of the BNCs.


**Fig. 2.7** Type of soil used in burying process of films **(a)** non-sterile soil, and **(b)** sterile soil

In this study, the SPI-based films with 5% LDH loading appeared to be more biodegradable in non-sterile soil in comparison to 0%, 2% and 9% LDH loadings; however, the underlying molecular mechanisms of biodegradation for the individual cases are yet to be understood through corroborative experimental approaches. [35] reported similar biodegradation patterns for the starch-based bioplastics. In fact, degradation of BNCs and various polymer-based composites in non-sterile soil is a complex process that depends on multiple factors such as mechanical and other physico-chemical properties of the materials; action of enzymes from various microbial species including bacteria, fungi and yeasts, aerobic/anaerobic conditions, light, moisture, pH, temperature, and different inorganic/organic constituents. Similar views were also proposed earlier for the biodegradable polymers [50]. LDH was also known to exhibit antimicrobial activity due to the presence of OH groups [51]. Therefore, LDH component could have an impact on biodegradation process of the SPI-based films.

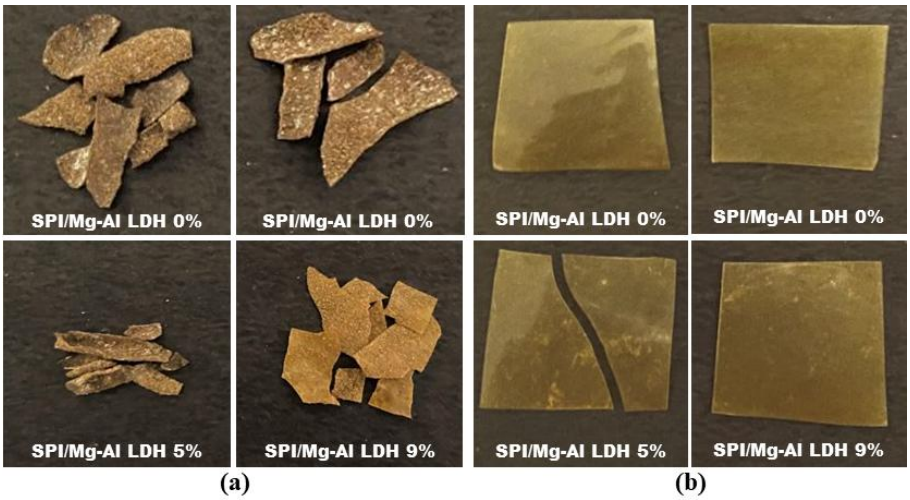


**Fig. 2.8** SPI-based films in **(a)** non-sterile soil, and**(b)** sterile soil

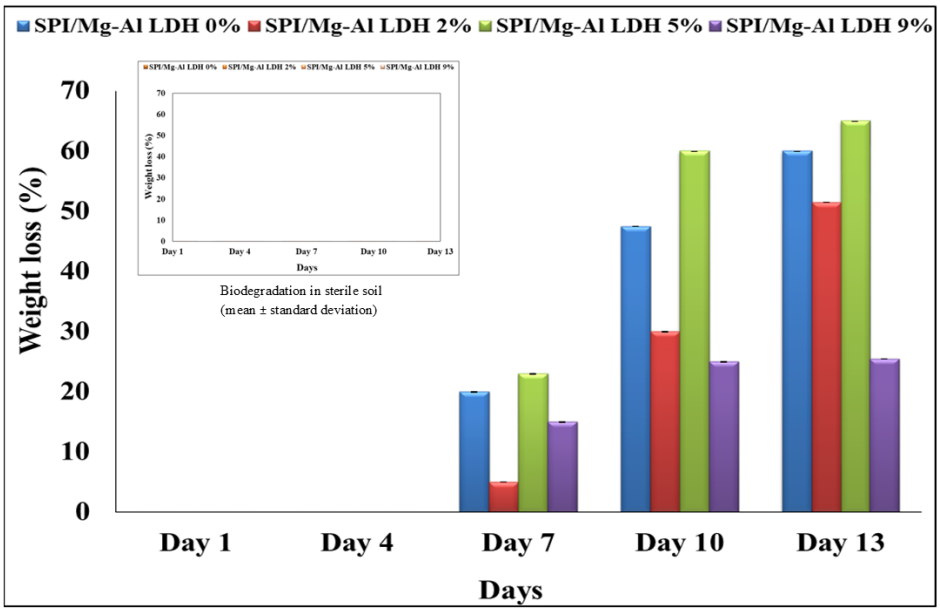


**Fig. 2.9** Biodegradation of SPI-based films in non-sterile soil (mean ± standard deviation)

## 2.4. Conclusion

The major focus of this study was on the preparation and characterization of a novel SPI/Mg-Al LDH-based bionanocomposite films using a simple solution casting method. Efforts were made to incorporate Mg-Al LDH particles into the SPI matrix. The XRD, FTIR, and FE-SEM data distinctly showed some interactions between Mg-Al LDH and the SPI matrix because of the intercalation/exfoliation of LDH sheets. 5 % Mg-Al LDH loading was effective

in terms of tensile strength of the SPI-based films. A reduction in tensile strength was observed at higher LDH loadings. This behaviour was attributed to filler agglomeration and non-uniform dispersion, which reduced stress transfer efficiency within the SPI matrix. Interestingly, no direct correlation was found between the thickness of the films and LDH concentrations. The BNC films showed considerable thermal stability. The BNCs were found to be biodegradable in non-sterile soil. Overall, the major findings of the study would be useful in preparing biodegradable packaging materials.

## References


1. Ozin GA, Arsenault A (2015) Nanochemistry: a chemical approach to nanomaterials. RSC.
2. Shameli K, Ahmad MB, Zargar M, Yunus WMZW, Rustaiyan A, Ibrahim NA (2011) Synthesis of silver nanoparticles in montmorillonite and their antibacterial behavior. Int J Nanomed 6:581. https://doi.org/10.2147/IJN.S17112
3. Hua Y, Cui SW, Wang Q, Mine Y, Poysa V (2005) Heat Induced Gelling Properties of Soy Protein Isolates Prepared from Different Defatted Soybean Flours. Food Res Int 38 (4):377–385. https://doi.org/10.1016/j.foodres.2004.10.006
4. Ojijo V, Ray SS (2013) Processing strategies in bionanocomposites. Prog Polym Sci 38(10–11):1543–89. https://doi.org/10.1016/j.progpolymsci.2013.05.011
5. Gonzalez A, Strumia MC, Alvarez Igarzabal CI (2011) Cross-Linked Soy Protein as Material for Biodegradable Films: Synthesis, Characterization and Biodegradation. J Food Eng 106 (4):331–338. https://doi.org/10.1016/j.jfoodeng.2011.05.030
6. Silva NHCS, Vilela C, Marrucho IM, Freire CSR, Pascoal Neto C, Silvestre, AJD (2014) Protein-Based Materials: From Sources to Innovative Sustainable Materials for Biomedical Applications. J Mater Chem B 2(24):3715–3740. https://doi.org/10.1039/C4TB00168K
7. Zhang H, Mittal G (2010) Biodegradable Protein-Based Films from Plant Resources : A Review 29 (2): 203–20. https://doi.org/10.1002/ep.10463
8. Kaewprachu P, Rawdkuen S (2014) Mechanical and Physico - Chemical Properties of Biodegradable Protein- Based Films : A Comparative Study 2(1):15–30. https://doi.org/10.14456/-fabj.2014.2
9. Ciannamea EM, Stefani PM, Ruseckaite RA (2014) Food Hydrocolloids Physical and Mechanical Properties of Compression Molded and Solution Casting Soybean Protein Concentrate Based Films. Food Hydrocoll 38:193–204. https://doi.org/10.1016/j.foodhyd.2013.12.013
10. Yuan Y, Sun YE, Wan ZL, Yang XQ, Wu JF, Yin SW, Wang JM, Guo J (2014) Chitin Microfibers Reinforce Soy Protein Gels Cross-Linked by Transglutaminase. J Agric Food Chem 62(19):4434–42. https://doi.org/10.1021/jf500922n

11. Felix M, Martín-Alfonso J. E, Romero A, Guerrero A (2014) Development of Albumen/Soy Biobased Plastic Materials Processed by Injection Molding. J Food Eng 125(1):7–16. https://doi.org/10.1016/j.jfoodeng.2013.10.018
12. Saenghirunwattana P, Noomhorm A, Rungsardthong V (2014) Mechanical Properties of Soy Protein Based "Green" Composites Reinforced with Surface Modified Cornhusk Fiber. Ind Crops Prod 60:144–150. https://doi.org/10.1016/j.indcrop.2014.06.010
13. Kalman DS (2014) Amino Acid Composition of an Organic Brown Rice Protein Concentrate and Isolate Compared to Soy and Whey Concentrates and Isolates. Foods 3(3):394–402. https://doi.org/10.3390/foods3030394.
14. Gonzalez A, Alvarez Igarzabal CI (2013) Soy Protein – Poly (Lactic Acid) Bilayer Films as Biodegradable Material for Active Food Packaging. Food Hydrocoll 33(2):289–296. https://doi.org/10.1016/j.foodhyd.2013.03.010
15. Netravali AN, Huang X, Mizuta K (2007) Advanced "green" Composites. Adv Compos Mater Off J Japan Soc Compos Mater 16 (4):269–282. https://doi.org/10.1163/156855107782325230.
16. Lei H, Du G, Wu Z, Xi X, Dong ZV (2014) Cross-Linked Soy-Based Wood Adhesives for Plywood. Int J Adhes Adhes 50:199–203. https://doi.org/10.1016/j.ijadhadh.2014.01.026
17. Echeverria I, Eisenberg P, Mauri AN (2014) Nanocomposites Films Based on Soy Proteins and Montmorillonite Processed by Casting. J Memb Sci 449:15–26. https://doi.org/10.1016/-j.memsci.2013.08.006.
18. Sadare OO, Daramola MO, Afolabi AS (2020) Synthesis and Performance Evaluation of Nanocomposite Soy Protein Isolate/Carbon Nanotube (SPI/CNTs) Adhesive for Wood Applications. Int J Adhes Adhes 100:102–605. https://doi.org/10.1016/j.ijadhadh.2020.102605.
19. Gupta P, Nayak KK (2015) Characteristics of protein-based biopolymer and its application. Polym Eng Sci 55(3):485–98. https://doi.org/10.1002/pen.23928
20. Garrido T, Etxabide A, Peñalba M, De La Caba K, Guerrero P (2013) Preparation and characterization of soy protein thin films: Processing–properties correlation. Mater Lett 105:110–2. https://doi.org/10.1016/j.matlet.2013.04.083
21. Zhao S, Yao J, Fei X, Shao Z, Chen X (2013) An antimicrobial film by embedding in situ synthesized silver nanoparticles in soy protein isolate. Mater Lett 95:142–4. https://doi.org/10.1016/-j.matlet.2012.12.106
22. Muller K, Bugnicourt E, Latorre M, Jorda M, Echegoyen Sanz Y, Lagaron JM, Miesbauer O, Bianchin A, Hankin S, Bolz U, Pérez G (2017) Review on the processing and properties of polymer nanocomposites and nanocoatings and their applications in the packaging, automotive and solar energy fields. Nanomater 7(4):74. https://doi.org/10.3390/nano7040074
23. Cavani F, Trifiro F, Vaccari A (1991) Hydrotalcite-type anionic clays: Preparation, properties and applications. Catal 11(2):173–301. https://doi.org/10.1016/0920-5861(91)80068-K

24. Evans DG, Slade RC (2006) Structural aspects of layered double hydroxides. Layered double hydroxides. 1–87. https://doi.org/10.1007/430_005
25. Wei M, Shi S, Wang J, Li Y, Duan X (2004) Studies on the intercalation of naproxen into layered double hydroxide and its thermal decomposition by in situ FT-IR and in situ HT-XRD. J Solid State Chem 177(7):2534–41. https://doi.org/10.1016/j.jssc.2004.03.041
26. Birgul A, Tasdemir Y (2012) Determination of the sampler type and rainfall effect on the deposition fluxes of the polychlorinated biphenyls. The Scientific World J https://doi.org/10.1100/2012/798020
27. Rives V, Ulibarri MA (1999) Layered double hydroxides (LDH) intercalated with metal coordination compounds and oxometalates. Coord. Chem. Rev 181(1):61–120. https://doi.org/10.1016/S0010-8545(98)00216-1
28. De Roy A (1998) Lamellar double hydroxides. Molecular Crystals and Liquid Crystals Science and Technology. Section A. Mol Cryst Liq 311(1):173–93. https://doi.org/10.1080/-10587259808042384
29. Kuthati Y, Kankala RK, Lee CH (2015) Layered double hydroxide nanoparticles for biomedical applications: Current status and recent prospects. Appl Clay Sci 112:100–16. https://doi.org/10.1016/j.clay.2015.04.018
30. Zumreoglu-Karan B, Ay A (2012) Layered double hydroxides—multifunctional nanomaterials. Chem. Pap 66(1):1–0. https://doi.org/10.2478/s11696-011-0100-8
31. Kura AU, Hussein MZ, Fakurazi S, Arulselvan P (2014) Layered double hydroxide nanocomposite for drug delivery systems; bio-distribution, toxicity and drug activity enhancement. Chem Cent J 8(1):1–8. https://doi.org/10.1186/s13065-014-0047-2
32. Vaccari A (1999) Clays and catalysis: a promising future. Appl Clay Sci 14(4):161–98. https://doi.org/10.1016/S0169-1317(98)00058-1
33. Hsueh HB, Chen CY (2003) Preparation and properties of LDHs/polyimide nanocomposites. Polym 44(4):1151–61. https://doi.org/10.1016/S0032-3861(02)00887-X
34. Olivera S, Hu C, Nagananda GS, Reddy N, Venkatesh K, Muralidhara HB (2019) Multipurpose composite for heavy metal sorption, antimicrobial, and antioxidant applications. Int. J Environ Sci Technol (4):2017–30. https://doi.org/10.1007/s13762-018-1774-z
35. Zoungranan Y, Lynda E, Dobi-Brice KK, Tchirioua E, Bakary C, Yannick DD (2020) Influence of natural factors on the biodegradation of simple and composite bioplastics based on cassava starch and corn starch. J Environ Chem Eng 8(5):104–396. https://doi.org/10.1016/-j.jece.2020.104396
36. Mostafa NA, Farag AA, Abo-dief HM, Tayeb AM (2018) Production of biodegradable plastic from agricultural wastes. Arab J Chem 11(4):546–53. https://doi.org/10.1016/j.arabjc.2015.04.008

37. Patil NB, Sharanagouda H, Doddagoudar SR, Ramachandra CT, Ramappa KT (2019) Effect of rice husk silica nanoparticles on physical and mechanical properties of soy protein isolate packaging films. IJCS 7(6):2272–7.
38. Abdelkader NBH, Bentouami A, Derriche Z, Bettaha N, De Menorval LC (2011) Synthesis and characterization of Mg–Fe layer double hydroxides and its application on adsorption of Orange G from aqueous solution. Chemi Eng J 169(1–3):231–238. https://doi.org/10.1016/j.cej.2011.03.019
39. Roelofs JC, van Bokhoven JA, Van Dillen AJ, Geus JW, de Jong KP (2002) The thermal decomposition of Mg–Al hydrotalcites: effects of interlayer anions and characteristics of the final structure. Eur J Chem 8(24) 5571–5579. https://doi.org/10.1002/1521-3765-(20021216)8:24<5571::AID-CHEM5571>3.0.CO;2-R
40. Zhang S, Xia C, Dong Y, Yan Y, Li J, Shi SQ, Cai L (2016) Soy protein isolate-based films reinforced by surface modified cellulose nanocrystal. Ind Crops Prod 80:207–13. https://doi.org/10.1016/-j.indcrop.2015.11.070
41. Kokoszka S, Debeaufort F, Hambleton A, Lenart A, Voilley A (2010) Protein and glycerol contents affect physico-chemical properties of soy protein isolate-based edible films. IFSET 11(3):503–10. https://doi.org/10.1016/j.ifset.2010.01.006
42. Edanol YD, Poblador JA, Talusan TJ, Payawan Jr LM (2020) Co-precipitation synthesis of Mg-Al-CO3 layered double hydroxides and its adsorption kinetics with phosphate (V) ions. Mater Today MATER 33:1809–13. https://doi.org/10.1016/j.matpr.2020.05.059
43. Chen J, Chen X, Zhu Q, Chen F, Zhao X, Ao Q (2013) Determination of the domain structure of the 7S and 11S globulins from soy proteins by XRD and FTIR. J Sci Food Agri 93(7):1687–91.https://doi.org/10.1002/jsfa.5950
44. Fathi N, Almasi H, Pirouzifard MK (2019) Sesame protein isolate based bionanocomposite films incorporated with TiO2 nanoparticles: Study on morphological, physical and photocatalytic properties. Polym Test 77:105–919. https://doi.org/10.1016/j.polymertesting.2019.105919
45. He Q, Zhang Y, Cai X, Wang S. Fabrication of gelatin–TiO2 nanocomposite film and its structural, antibacterial and physical properties (2016) Int. J. Biol. Macromol 84:153–60. https://doi.org/10.1016/j.ijbiomac.2015.12.012
46. Wang Z, Kang H, Zhao S, Zhang W, Zhang S, Li J (2018) Polyphenol-induced cellulose nanofibrils anchored graphene oxide as nanohybrids for strong yet tough soy protein nanocomposites. Carbohydr Polym 180:354–64. https://doi.org/10.1016/j.carbpol.2017.09.102
47. Becker CM, Gabbardo AD, Wypych F, Amico SC (2011) Mechanical and flame-retardant properties of epoxy/Mg–Al LDH composites. Compos Part A Appl Sci 42(2):196–202. https://doi.org/10.1016/-j.compositesa.2010.11.005
48. Tseng CH, Hsueh HB, Chen CY (2007) Effect of reactive layered double hydroxides on the thermal and mechanical properties of LDHs/epoxy nanocomposites. Compos Sci Technol 67(11–12):2350–62. https://doi.org/10.1016/j.compscitech.2007.01.011

49. Wang Z, Kang H, Zhang W, Zhang S, Li J (2017) Improvement of interfacial interactions using natural polyphenol-inspired tannic acid-coated nanoclay enhancement of soy protein isolate biofilms. Appl Surf Sci 401:271–82. https://doi.org/10.1016/j.apsusc.2017.01.015
50. Karak N (2012) Vegetable Oil-Based Polymers. 2- Biodegradable polymers. Woodhead Plublishing, pp 31–53.
51. Mishra G, Dash B, Pandey S (2018) Layered double hydroxides: A brief review from fundamentals to application as evolving biomaterials. Appl. Clay Sci 153:172–86. https://doi.org/-10.1016/j.clay.2017.12.021

# Chapter- 3

## *Biodegradable wheat gluten/nanoclay films for food packaging applications*

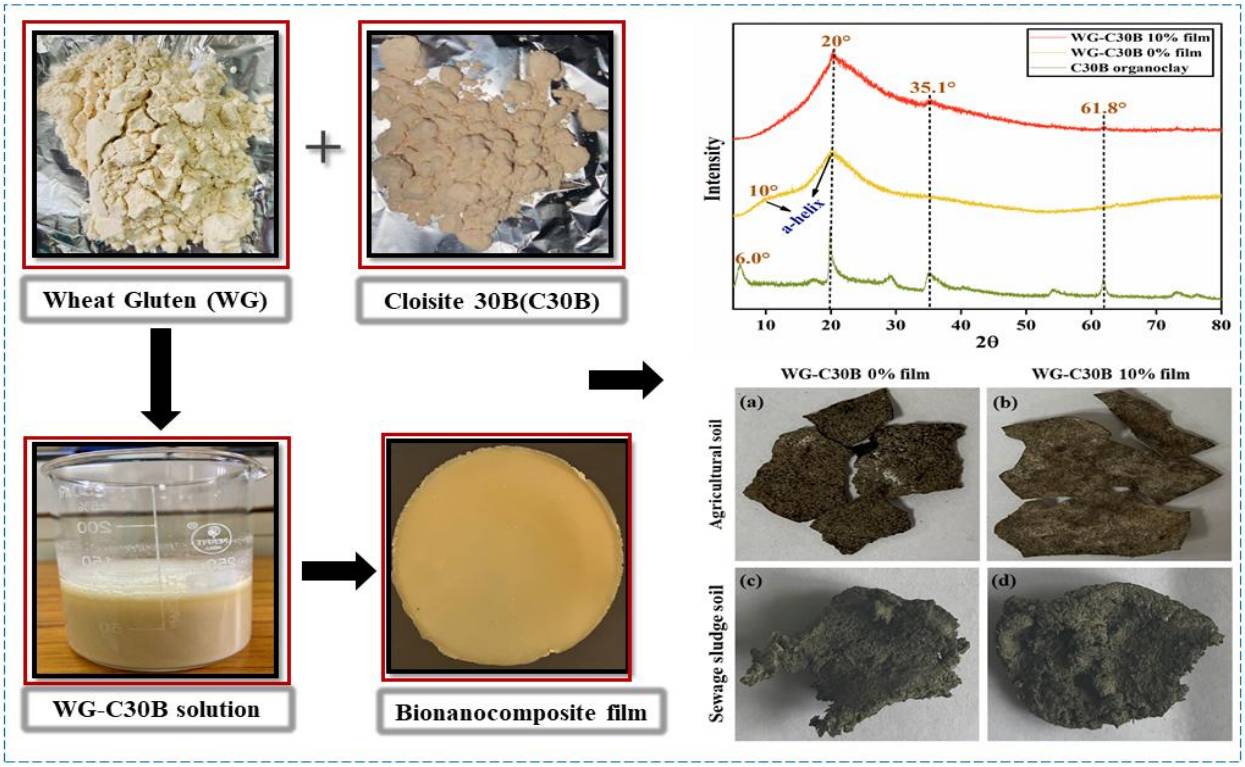


### Schematic Outline:

The purpose of this study was to examine the effect of C30B organoclay nanofiller at different concentrations on WG-based BNC films prepared by the solution casting method. The WG–C30B film containing 10% organoclay exhibited optimal mechanical strength, enhanced thermal stability, notable antibacterial activity, and effectively extended the shelf life of green grapes up to 18 days. Additionally, the biodegradation behaviour of the films was evaluated in both agricultural and sewage sludge soils.

## 3.1 Introduction

Currently, the development of biopolymer-based packaging materials has become an emerging trend in bionanotechnology. Potentially, they could serve as viable alternatives to petroleum-based, non-biodegradable materials due to their biodegradability and eco-friendly nature. For example, effective and safe packaging materials remain crucial in food processing industries for safety, stability, quality, and overall shelf life of food products. Proper packaging can protect them from damages due to physical, chemical, and biological changes during transportation, distribution, and storage. Conventionally, several synthetic polymers like polylactic acid, polybutylene succinate and polyvinyl chloride were used in developing packaging materials [1]. Biodegradable packaging materials with antimicrobial properties are gaining importance as they could prevent spoilage of food products due to pathogenic microbes [2–6]. Among various biopolymers, proteins are relatively more preferred nowadays because of their characteristic physico-chemical properties [7]. Various physical, chemical, and enzymatic treatments are possible due to their amphiphilic nature, electrostatic charges and conformational changes like partial/complete unfolding which were exploited in making various coatings/films [8,9].

Gluten is a storage protein found in the endosperm of wheat, rye and barley grains. Wheat gluten is widely available, having a protein content of more than 75%. Gliadin and glutenin are the major components of gluten that influence the physico-chemical characteristics of cereal-based food products. Gliadins are soluble in aqueous 70% alcohol whereas, glutenin remains insoluble primarily in common solvents because of its size and complex cross-linked structures. Most of the glutenins are moderately soluble under both acidic and alkaline conditions. Although wheat gluten possesses good film-forming ability and biodegradability, its practical application is often restricted by limitations such as moisture sensitivity, moderate barrier performance, and insufficient mechanical stability under certain conditions. Various methods like solvent casting, compression, moulding, extrusion, and electrospinning, either singly or in combination, could be adopted for this purpose [10–13]. Physico-chemical properties of these films were found to be dependent on various factors like pH, heat treatment and concentration of solvent in a film-forming solution. The isoelectric point (p*I*) of wheat gluten is around 7.5. Usually, proteins show poor film-forming properties at their p*I*s [14]. The gluten system can be viewed as a network of polymers with various bonding interactions, such as hydrogen bonds, hydrophobic and ionic interactions. When a fibrous gluten protein network was blended with

a compatible plasticizer and crosslinker, the biopolymer-based films became rigid, flexible, and ductile [15].

Clays are naturally occurring earthly materials commonly used in traditional and modern-day medicines for healing various illnesses [16]. Several type of clays were used as fillers in bionanocomposites (BNCs) due to some characteristic features that include high surface areas, nanoscale sizes, adsorption capacity, hydrophilic/hydrophobic properties, and, importantly, the capability of forming microporous layered structures [17]. Recent literature showed that the global nanoclay market size could grow to 6.4 billion USD by 2032 [18]. The growing importance of nanoclays like montmorillonite (MMT) and its modified forms, such as Cloisite 30B (C30B) and Cloisite 15A (C15A), was due to their layered silicate structures [19,20]. Cloisite 30B (C30B) refers to a MMT-derived organoclay known as methyl tallow bis-2-hydroxyethyl quaternary ammonium MMT. The layers of C30B have a thickness of approximately 1.0 nm, while the lateral dimensions range from 100-500 nm [21,22]. As reported earlier, C30B imparted antimicrobial activities to the polymeric materials compared to normal unmodified nanoclay [23–26]. Chitosan-based BNC films blended with C30B nanoclay having quaternary ammonium groups exhibited antimicrobial activity against Gram-positive bacteria [27].

Usually, nanocomposites can assume flexible film forms for wrapping fresh and dried food products. Several branded packaging/storing materials, namely Debbie Meyer BreadBags™, Aisaika Everfresh Bag, Plantic® Plastic Tray are used to store bread, fruits/vegetables, and chocolates, respectively [28]. Fruits and vegetables are rich sources of vitamins, minerals, proteins, antioxidants, fibers, and other nutrients. Preservation of these farm products with high moisture contents (75–95%) is challenging due to short shelf life and easily perishable nature [29]. Their spoilage could be avoided by using biodegradable bio/polymeric nanocomposite packaging materials, which could minimize respiration rate, ethylene level, water loss and microbial loads [30,31].

Apart from various inorganic nanofillers like ZnO, $TiO_2$ and $SiO_2$, there is a growing interest in using several layered nanoclays in BNCs due to high interfacial interactions with polymer matrix for improving desirable physico-chemical properties of the films [32,33]. Previously, studies have been done separately on wheat gluten protein and C30B organoclay with various nanofillers and biopolymers [34–39]. However, the interactions between WG and C30B in developing packaging materials have not been studied so far. This report employed a simple and reproducible solution casting method to prepare WG-based BNC films blended with C30B

organoclay. Subsequently, various physico-chemical properties such as microstructure, crystallinity, thermal stability, water sensitivity, mechanical properties and color determination of the prepared films were examined. The prepared films were translucent, smooth, flexible, and foldable with a uniform appearance. Incorporating organoclay into the BNC films showed significant improvement in mechanical properties, reduced moisture content along with water solubility, and enhanced surface hydrophobicity. The organoclay-loaded film demonstrated better thermostability as the residual mass increased up to 22%, which was 5% in the case of pristine WG-based BNC film. Their antibacterial properties were studied using the agar disc diffusion method and by checking the shelf-life extension of green grapes under different conditions for up to 18 days. The organoclay-loaded film exhibited an antibacterial effect against both *Salmonella enterica* and *Staphylococcus aureus*. In shelf-life studies, wrapping method was found to be more effective than dip coating. Previously, no studies on the preservation of green grapes were done for duration of 18 days under specified storage conditions using these methods. Moreover, these films were found to be biodegradable in agricultural and sewage-sludge soil. The biodegradation rate in sewage sludge soil was significantly higher than that of agricultural soil. Overall, the strategies adopted in preparing BNC films appeared to be promising and sustainable for developing packaging materials.

## 3.2 Materials and methods

### 3.2.1 Chemicals

Commercial-grade Wheat Gluten (WG) was procured from Nottacia (New Delhi, India). Luria Broth (LB), Agar Agar Type I (CAS No. 9002-18-0), and Tetracycline hydrochloride (CAS No. 64-75-5) were purchased from Himedia, India. Cloisite 30B (C30B) nanoclay (CAS No. 341537-63-1), Glycerol (CAS No. 56815), Sodium hydroxide (NaOH) (CAS No. 1310-73-2), Sodium chloride (NaCl) (CAS No. 7647-14-5), Sodium hypochlorite (NaOCl) (CAS No. 7681-52-9) were procured from Aritech Chemazone Pvt. Ltd., Qualigens Fine Chemicals, and Loba Chemie, India, respectively. Whatman filter paper (CAT No. 1001-125) was obtained from Global Life Sciences Solutions Operations UK Ltd. Deionized water was purchased from Organo Biotech Lab. Pvt. Ltd., India, for routine use.

### 3.2.2 Preparation of WG-C30B BNC Films

WG-C30B-based BNC films were prepared by using solution casting method as reported earlier with some minor modifications [40]. A schematic view is provided in **Scheme 3.1** regarding preparation of the BNC films. Briefly, the organoclay at varying concentrations, i.e.

5%, 10%, and 15% w.r.t. weight of WG, was dispersed in 10 mL deionized water and kept on stirring overnight to ensure proper swelling. To prepare WG solution, pH of the required amount of deionized water was adjusted to 9.0 by adding 1.0 M NaOH. Then, 10.0 g of WG was added to water with stirring at low speed for 30 min at room temperature; pH of the solution was again adjusted to 9.0, and volume made up to 100 mL, followed by heating at 70°C for 10 min in water bath. Glycerol (30% of the weight of WG) was added to the WG solution and mixed thoroughly. Likewise, the C30B suspensions (5%, 10%, and 15% w.r.t weight of WG) were mixed with the WG solution with stirring at ambient temperature for two days (referred to as WG-C30B 5%, WG-C30B 10%, and WG-C30B 15%). The same procedure was adopted to prepare only WG-based film solution except for the addition of C30B, i.e., WG film. Around 95 mL of the film-forming solution was cast on Teflon-coated pan (19.5 cm × 19.5 cm) and allowed to dry at 30 ± 2 °C in an incubator for 48 h. The BNC films were stored at ambient temperature for further characterization and use.

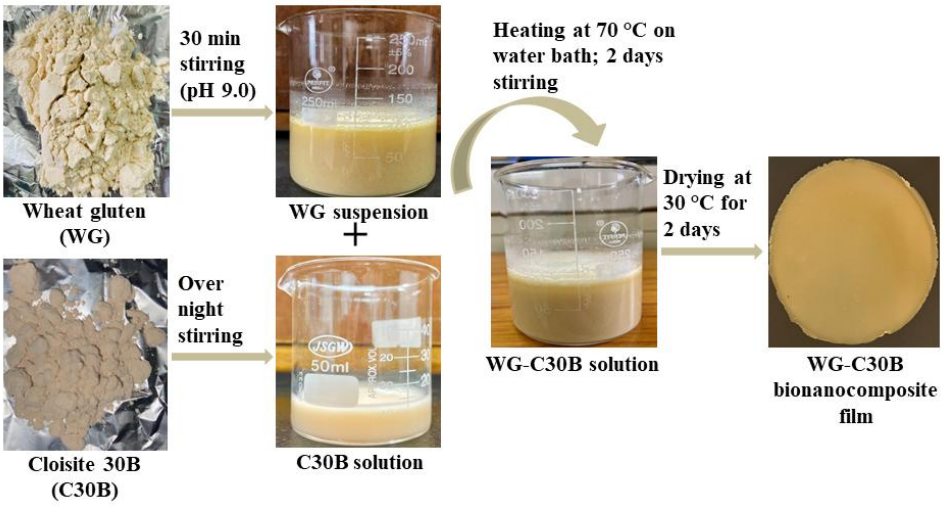


**Scheme 3.1** A schematic representation of wheat gluten (WG)/cloisite30B (C30B)-based bionanocomposite films

### 3.2.3 Physical Properties of BNC films

#### 3.2.3.1 Mechanical Properties of BNC Films

Mechanical properties like tensile strength (TS) and elongation at break (EB) were determined by using a Tensile Strength Tester (Digital vertical model, Angels Instruments, India) based on a standard method IS 1060-1 (Indian Standard, Part 1) as reported earlier [41]. Each film

sample was cut into rectangular strips (11 cm × 1.5 cm). The initial grip separation was kept at 90 mm with a 20 mm/min speed in order to measure the values. Experiment was done in triplicate for an average value.

#### 3.2.3.2 Thickness of BNC Films

The thickness of BNC films was measured with a micrometer thickness gauge (L&W Micrometer, Switzerland). For each film, measurements were taken at six different locations. The experiment was done in triplicate and average of these measurements represents thickness of each film [41].

#### 3.2.3.3 Surface Color Determination of BNC Films

Surface color of the films was determined by using a brightness tester (L&W Elrepho Brightness Tester, Switzerland). The prepared film samples were cut into 3 cm × 3 cm pieces; color coordinates such as L*, a*, b* and yellow indices (YIs) were measured in triplicates for each sample and average values were tabulated.

### 3.2.4 Water Sensitivity Properties of BNC Films

#### 3.2.4.1 Moisture Content (MC)

The film samples were cut into 2 cm × 2 cm pieces to find moisture content. Initial weight of film pieces was noted and placed in a hot air oven at 100 °C for 24 h to obtain weight of the dried film samples [42]. Measurements were done in triplicate to get the average value. The moisture percent (%) was calculated by the following equation (1):

$$\text{Moisture percent (\%)} = \frac{m_1 - m_2}{m_1} \times 100 \qquad (1)$$

Where, $m_1$ = initial weight and $m_2$ = final weight after drying

#### 3.2.4.2 Water Solubility

Water solubility was determined using a method reported earlier with some modifications [43]. First, the film samples were cut into 2 cm × 2 cm pieces and allowed to completely dry at 100 °C for 24 h. The initial weight of dried samples (first drying) was recorded. Each dried film was submerged in 50 mL of deionized water for 24 h at ambient temperature. Water was drained off, and the wet films were dried again at 100 °C for 24 h to get final weight (second drying). Measurements were done in triplicate to get the average value. The solubility (S) % was calculated by the following equation (2):

$$S\ (\%) = \frac{a_1 - a_2}{a_1} \times 100 \qquad (2)$$

Where, $a_1$ = weight after first drying and $a_2$ = weight after second drying

#### 3.2.4.3 Water Contact Angle (WCA)

WCAs of the film samples were measured by goniometer contact angle measuring device (Apex Instruments Co. Pvt. Ltd., India) in a static contact angle mode. Each film was cut into square pieces (4 cm × 4 cm) and placed on a horizontal platform fitted with a WCA analyzer. Aliquots of 3.0 µL deionized water were randomly dropped onto the surface of each BNC film. Changes in the shape of water droplets were recorded. This process was done in triplicate to get the average value for each film sample.

### 3.2.5 Instrumentation

#### 3.2.5.3 X-ray Diffraction (XRD)

XRD patterns of powdered C30B and the film samples were examined by using a PANalytical-Xpert-Pro (Almelo, Netherlands) diffractometer with Cu K-α (λ = 0.154 nm) radiations, and the data were taken at 2θ = 5°−80° (with step size = 0.01°).

#### 3.2.5.4 Field Emission Scanning Electron Microscopy (FESEM)

Surface morphology of the prepared materials was examined by FESEM (Carl Zeiss Sigma 500, Germany). To prepare the nanoclay sample, a drop-cast method was adopted. Briefly, around 2.0 mg of C30B powder was dispersed in 5.0 mL of deionized water, and a few drops of the suspension were cast on copper tape and allowed to dry completely at 35 °C. In the cases of BNC films, they were cut into 1 cm × 1 cm pieces. All these samples were sputter coated with a gold layer prior to analyses.

#### 3.2.5.3 Atomic Force Microscopy (AFM)

AFM analyses (model: NT-MDT Solver NEXT, Russia) were carried out to examine the topography of film samples under ambient conditions using a standard cantilever holder. Non-tapping/non-contact modes were used for analyses. Average surface roughness (Sa) and root mean square (Sq) were measured directly from the AFM images.

#### 3.2.5.4 Thermogravimetric Analysis (TGA)

The thermogravimetric analyzer (NETZSCH STA 449 F3 Jupiter®-Thermal Analysis System, Germany) was used to test thermal stabilities of both the film samples and C30B powder (approximately 25 mg of each sample was taken for analysis). In each case, the heating rate was kept at 10 °C/min from 25–800 °C under air with gas flow rate of 50 mL/min.

### 3.2.6 Determination of Antibacterial Properties of the BNC Films

Disc diffusion method was adopted to examine the antibacterial activities of WG and WG-C30B 10% films. Precultures of the food-borne bacterial strains, namely *Staphylococcus aureus* (gram-positive) and *Salmonella enterica* (gram-negative) were used in this study. In order to show antibacterial properties of the BNC films, following method was adopted. Briefly, the BNC films were cut into discs of approximately 6 mm diameter and each side of the disc was irradiated by UV light under laminar air flow for 25 min. Sterile discs of similar dimension were also prepared using Whatman filter paper. The bacterial strains were grown in Luria Broth (LB) for 16 h at 37°C. The overnight grown cultures were 3-fold diluted with sterile standard saline solution and 80 µL of each diluted bacterial suspension was uniformly spread onto Luria-Agar (LA) plates. Subsequently, the discs of the BNC films were placed on the agar surface; the filter paper discs priorly dipped in tetracycline solution (1.0 mg/mL) were also used as a positive control. The plates were incubated at 37 °C overnight. Appearance of inhibition zones (colony-free areas) indicated antibacterial activities.

### 3.2.7 Daily Life Applications of the Prepared BNC Films

#### 3.2.7.1 Application of BNC Coatings/Films in the Preservation of Fruits

In order to develop packaging material, both BNC coatings/films were used to preserve green grapes. Briefly, healthy green grapes of similar weight, size, shape, color, and maturity, with no mechanical injuries, were purchased from a local market. For surface sterilization, the grapes were first washed with running tap water, then dipped in 0.5% sodium hypochlorite (NaOCl) solution for 10 min, rinsed with sterile deionized water and allowed to aseptically dry at room temperature. Both BNC solutions and films were treated with UV rays for 30 min under laminar flow prior to their uses. For coating, the surface-sterilized green grapes were dipped separately in WG and WG-C30B 10% solutions for 15 min, followed by gently drying of the coated layers for 10 s over hot air surrounding the flame. The pretreated green grapes were also wrapped with corresponding BNC films. For wrapping, the films were cut into circular pieces and placed in the Petri dishes to cover both the upper and lower surfaces. The grapes were then placed between the films, and the dishes were sealed externally before storage and further analysis. All these coated/wrapped grapes were stored in the laboratory under ambient conditions (with diurnal temperature variations of 30−35°C ± 2 °C/15− 20 °C ± 2°C being day/night temperatures with an average relative humidity of 27%, during late March to mid-April) along with in the incubators set at 4 °C and 42 °C. Gradual changes in the grapes were noted periodically for up to 18 days.

#### 3.2.7.2 Biodegradability of the BNC Films in Soil

Biodegradability test was conducted by composting method with some modifications [41, 44]. The following soil samples were used: soil directly from an agricultural field (pH ~6.4) and soil mixed with sewage sludge (pH ~8.0). Both the soils were also heat-treated (at 45 °C for 24 h) for sustenance of thermophilic microbes. Completely sterile soils were prepared by calcining them at 550 °C for 4 h in a muffle furnace (control). Approximately 0.5 g of the film samples were kept inside 30 g of each soil sample in a clean and sterile glass jar and incubated at 30 ± 2 °C. On every third day, each film sample was taken out of the soil, oven-dried at 40 °C for 3–4 h, adhering soil particles were removed prior to taking weight, then again placed inside the soil. This test was continued for up to 12 days and done in triplicate to get the average values. The extent of biodegradation was calculated by the equation given below (3):

$$\text{Biodegradability (\%)} = \frac{\text{initial weight} - \text{final weight}}{\text{initial weight}} \times 100 \qquad (3)$$

## Statistical Analysis

All the experiments were performed in triplicates, and the data was expressed as mean ± standard deviation. The data analyses were performed by using one-way analysis of variance (ANOVA) in GraphPad Prism (GraphPad Software, LLC, California, USA). Mean values comparison was determined by Tukey's test. The differences were considered significant at $p < 0.05$.

## 3.3 Results and discussion

### 3.3.1 Physical Properties of BNC Films

#### 3.3.1.1 Mechanical Properties of BNC Films

Mechanical strength is a critical parameter for packaging applications regarding handling, transportation, and maintaining structural integrity during storage. Tensile strength (TS) and elongation at break (EB) were determined to examine the mechanical properties of BNC films. The effect of clay loading on prepared WG-based films was shown in **Table 3.1**. In the cases of WG and WG-C30B 5% films, the TS values were 0.7±0.02 KNm/g to 0.82±0.01 KNm/g, respectively; whereas, the value was significantly higher i.e., 1.11±0.04 KNm/g for WG-C30B 10% film which clearly indicated the reinforcing effect of organoclay. An increase in TS value in polymer/clay nanocomposites could be due to the formation of electrostatic

interactions and hydrogen bonds between polymer matrix and silicate layers [21]. The reinforcement of gluten matrix by organoclay particles produced a robust network until reaching a critical threshold concentration. The published report on gelatin/magnetic iron oxide nanoparticle-based films supported this view [45]. Further increment in the concentration of organoclay (WG-C30B 15%) led to a decrease in TS value (0.79±0.08 KNm/g). The addition of a nanofiller beyond its optimal concentration resulted in the weakening of hydrogen bonding within protein structure, which in turn showed plasticizing effect characterized by altering their strength, stiffness, and enhanced strain at break. The tendency of agglomeration at higher concentrations also led to a decrease in tensile strength. Usually, inorganic/organic composites with inorganic fillers were known to be stiff and more brittle. Taheri and Sayyahi showed a similar reduction in tensile strength (19±0.52) for TPU loaded with a maximum 5% concentration of OMMT [46]. According to earlier reports, layered structured nanofillers were considered stress concentrators [47,48]. The effect of nanofiller was found to be more prominent in terms of extensibility (EB), indicating an increase in film flexibility. There was a significant difference ($p$ = 0.001) in mechanical properties of the films.

The BNC films were prepared with varying concentrations of C30B i.e., 5%, 10%, and 15% and their mechanical properties namely tensile strength were studied, as it was a crucial parameter with regard to strength of a packaging material. The WG-C30B 10% film appeared to be most suitable in comparison to other prepared films. More specifically, the results indicated that WG-C30B 10% film showed better mechanical properties in terms of compatibility between clay particles and protein matrix, compactness and strength. Keeping all these aspects in view, the major focus was on WG-C30B 10% film for further characterization and other experiments. Interactions between cationic groups of amino acid side chains ($–NH_3^+$) and $Na^+$ ions at the clay surface are considered to play important role in a BNC film [49,50]. The processes of intercalation and exfoliation of C30B organoclay significantly impact mechanical properties of the BNC films. Intercalation reinforced the polymer matrix; however, such changes remained less noticeable due to limited separation of clay layers. On the contrary, exfoliation led to more homogeneous dispersion of clay layers resulting in a stress transfer more or less uniformly across the BNC film. This explains why there is an increase of tensile strength in the case of WG-C30B 10% film. Usually, the desirable mechanical properties of a film can only be achieved at an appropriate concentration of nanofiller (such as 10% C30B in this study); while at higher concentration, mechanical properties of the intercalated structures could be affected due to uneven dispersion throughout the polymer matrix [22,51].

**Table 3.1** Mechanical Properties of BNC film samples (mean ± standard deviation)

| Film Samples | Tensile strength (KNm/g) | Elongation at break (%) |
|---|---|---|
| **WG film** | 0.71±0.02 | 7.5±0.36 |
| **WG-C30B 5% film** | 0.82±0.01 | 20±0.57 |
| **WG-C30B 10% film** | 1.11±0.04 | 36.2±0.60 |
| **WG-C30B 15% film** | 0.79±0.08 | 28.6±0.35 |

### 3.3.1.2 Thickness of BNC Films

Several methods were reported for preparation of BNC films. As mentioned earlier, a simple and efficient solution casting method was adopted in this study. The thickness of WG and WG-C30B 10 % films was found to be 235±12.4 and 230±5.8 μm ($p$=0.000), respectively, as shown in **Table 3.2**. The prepared films were found to be smooth, flexible, foldable, and mostly uniform in appearance. Both films were translucent; however, the former was shiny while the latter was matte in appearance. The data also indicated that organoclay (10% w.r.t. WG) had no considerable impact on thickness of the film. Similar findings were also reported on soy protein isolates and rice husk silica nanoparticles. The thicknesses of blend at varying concentrations of SNPs were found to be in the range of 0.211–0.213 mm [52]. Usually, thickness of a BNC film was known to depend on the extent of compatibility and incorporation of a particular nanofiller into biopolymer matrix [53]. Sheet-like structure of C30B organoclay could have probably replaced the surrounding water molecules of WG matrix. In the cases of MMT/soy protein-, soy protein/ZnO-and nanocrystals-based BNC films, the changes in thickness remained non-significant [54,55].

**Table 3.2** Thickness, water solubility and moisture content of WG film and WG-C30B 10% BNC film samples (mean ± standard deviation)

| Film Samples | Thickness 444(µm) | Moisture content (MC %) | Water solubility (S %) |
|---|---|---|---|
| **WG film** | 235±12.4 | 11.51±1.2 | 69.56±0.5 |
| **WG-C30B 10% film** | 230±5.8 | 8.04±0.5 | 39.83±0.7 |

### 3.3.1.3 Surface Color Determination of BNC Films

The color of film is a crucial aspect with regard to their looks and commercial uses [56]. Here terms of L*, a*, b* and yellow index (YI) express the color of BNC films as shown in **Table 3.3**. L* gives lightness, and a* represents red/green color, where a positive value stands for redness and a negative value for green color. In the case of b*, it refers to yellow/blue color, where the positive value gives yellowness, and the negative value was for blue color. Color properties were found to be significantly influenced by the presence of the blended nanofiller. However, the extent of color change was dependent on nanofiller contents. The a* values of WG-C30B 10% film were found to be significantly higher positive in comparison to WG film (indicating shift to red); whereas, the b* values remained positive and almost comparable for both the films (indicating change to yellow), giving an overall red-yellow tone. These color shifts were reflected in the YI parameter. A slight reduction of the L* values and increase in the YI values were noticed after clay loading. All these values were significantly different ($p$=0.000). Similar b* values indicated a higher amount of gluten protein fraction and the presence of other components such as phospholipids and fats in the films [57]. These results were different from the observations reported by Fu and co-workers on wheat gluten protein/cellulose nanocrystals (WGP-CNC)-based films. The b* values were found to show an increasing trend compared to pristine WGP film i.e. 6.28±0.10 (WGP), 8.61±0.84 (WGP-CNC-1), and 7.83±0.25 (WGP-CNC-2); however, the maize protein, zein and soy protein isolates (SPI)-based blends showed non-significant changes with increased CNC concentration, which were in agreement with our findings [58]. The films' opacity increased at higher clay concentrations, indicating a considerable affinity for gluten protein with clay particles. Such changes could be due to surface properties like the hydrophobic nature of C30B and its dispersion into the WG solution. Similar trends were also noticed in the cases of whey protein isolates (WPI) blended with different nanoclays [23].

**Table 3.3** Color determination of WG film and WG-C30B 10% BNC films (mean ± standard deviation)

| Film Samples | Film color | | | |
|---|---|---|---|---|
| | L* | a* | b* | YI |
| **WG film** | 67.44±0.0 | 11.17±0.63 | 52.30±0.0 | 103.31±0.0 |
| **WG-C30B 10% film** | 66.38±0.0 | 13.62±0.23 | 51.94±0.0 | 106.64±0.0 |

*Where, L*= lightness; a*= red/green; b*= yellow/blue, and YI= Yellow index, respectively*

### 3.3.2 Water Sensitivity Properties of BNC Films

Measuring water sensitivity of the BNC films remained a crucial parameter in assessing their suitability as a packaging material. Here, a few widely used methods were adopted to evaluate the water sensitivity of the WG-based films.

#### 3.3.2.1 Moisture Content (MC)

Moisture content is an indicator of the water sensitivity of biopolymer-based films. Particularly for food packaging purposes, the extent of moisture transfer between foods and surroundings must be considerably reduced [59]. Moisture contents (MC) of the WG and WG-C30B 10% films were found to vary significantly **(Table 3.2)**. Glycerol-based protein films were more sensitive to water due to their inherent hydrophilic nature. This explained why the MC value of the former reduced from 11.51±1.2 to 8.04±0.5 after loading hydrophobic organoclay. The reduction of water content in the WG-C30B 10% film suggested strong interactions between protein-clay and glycerol-clay interfaces, resulted in minimal available sites for water retention [45]. A decrease in moisture content was correlated with an increase in tensile strength due to the lower availability of water to plasticize the protein matrix. The results were relatively more promising in comparison to wheat gluten and lignin nanoparticle (LNP)-based BNCs. WG film loaded with 3 % LNP exhibited considerably higher moisture content (10.14±0.81) [60].

#### 3.3.2.2 Water Solubility

Water solubility is a vital aspect in assessing the stability of packaging films in a wet environment [56]. The values of solubility (S%) of the prepared films were shown in **Table 3.2**. As expected, WG film had shown significantly higher solubility in water (69.56±0.5) as compared to WG-C30B 10% film (39.83±0.7) indicating the effect of

organoclay in the BNC film ($p = 0.001$). It was likely due to interactions between clay particles and wheat gluten molecules. Since free water molecules do not strongly interact with nanofiller-based composite films as compared to biopolymer films. More specifically, the formation of hydrogen bonds between the organo-modified nanofiller and biopolymers lowered water solubility. The clay-loaded film retained structural integrity and did not form a gel, whereas pristine gluten film was found to be dissolved in water. The findings were proved to be better than previous reports for methylcellulose/MMT-based BNC films. At maximum MMT concentration (60 wt%), the water solubility was 54.5±1.9. All these observations recognized importance of nanofiller in developing biopolymer-based packaging materials [61].

#### 3.3.2.3 Water Contact Angle (WCA)

WCA refers to a quantitative measure of the wetting properties of packaging materials. Measure of WCA reveals hydrophobic or hydrophilic nature of a film surface [62]. As shown in **Fig. 3.1**, the WCA value for WG film was 38.93°±0.008, suggesting its poor water resistance due to the combined effects of inherent hydrophilicity due to presence of polar amino acids and glycerol [63]. In the case of WG-C30B 10% film, the WCA value was significantly higher, i.e., 77.56°±0.137, due to increased surface hydrophobicity. WCA values of the films were significantly different ($p$=0.000). The clay-loaded film was found to be more hydrophobic than the pristine WG film. It was shown that the organic modification of clay resulted in its enhanced hydrophobicity [64]. Comparable results were showed by El-Wakil and co-workers for wheat gluten/nanocellulose $TiO_2$–based nanocomposites. The WCA value of WG blend with 12.5% CNC increased to 78.48±1.18 and 89.70±0.14 with 1% $TiO_2$ incorporation [39]. Poly(ε-caprolactone)/cloisite 30B thin films also showed similar properties [65]. Films exhibiting WCA values above 65° could be considered hydrophobic [66]. As reported earlier, positive contact angle values indicated water droplet adhesion to the solid composite surface; therefore, higher the positive value stronger is the bonding [67].

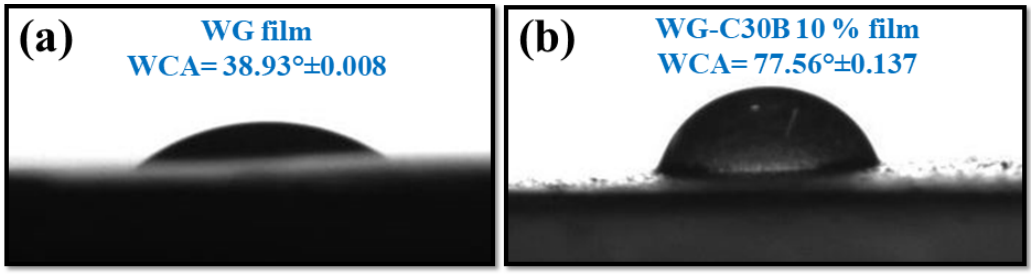


**Fig. 3.1** Water contact angle (WCA) of **(a)** WG film, and **(b)** WG-C30B 10% film

### 3.3.3 Characterization

#### 3.3.3.1 X-ray Diffraction (XRD)

The XRD patterns of C30B powder along with WG and WG-C30B 10% films were shown in **Fig. 3.2**. Amorphous gluten proteins were associated with α-helical structures; this explained why WG film showed two diffraction peaks corresponding to the 2θ values at 10° and 20°. The peak at 2θ =10° of this film represented a mean interhelix distance, while average backbone distance within the helix was linked to the peak at 2θ = 20° [68]. In the case of C30B, diffraction peaks at 2θ = 6°, 20°, 35.1° and 61.8° referred to crystallinity of the organoclay; here, 2θ =6° indicated d-spacing between the clay layers which was about 1.47 nm [69]. Once organoclay was incorporated into the WG matrix, i.e., WG-C30B 10% film, some peaks conspicuously disappeared with a concomitant decrease in intensities of the remaining peaks. The clay particles were probably surrounded by polypeptide chains in the matrix. There was no diffraction peak at 2θ = 6° in this composite film, possibly due to considerable exfoliation of silicate layers of the organoclay. Disappearing of C30B peak in WG-C30B 10% film suggested uniform distribution of C30B particles into the gluten protein matrix and their compatibility with each other. A distinct peak at 2θ = 20° along with other peaks suggested a shift towards crystallinity because of the intercalation of polypeptide chains of WG into clay layers. There was no change in the peak positions of organoclay, indicating that C30B structure remained unchanged. Very likely, interactions of these chains with aluminosilicate layers contributed to the rise in crystallinity. Shahvalizadeh and co-workers reported similar results for gelatin, tragacanth, and ZnO nanoparticle-based BNC films [70]. Similar features were noticed in the cases of Nylon 6, 12/cloisite 30B electrospun nanocomposites [71]. Therefore, intercalation/exfoliation of layered C30B structure in the WG matrix confirmed formation of the WG-C30B blend.

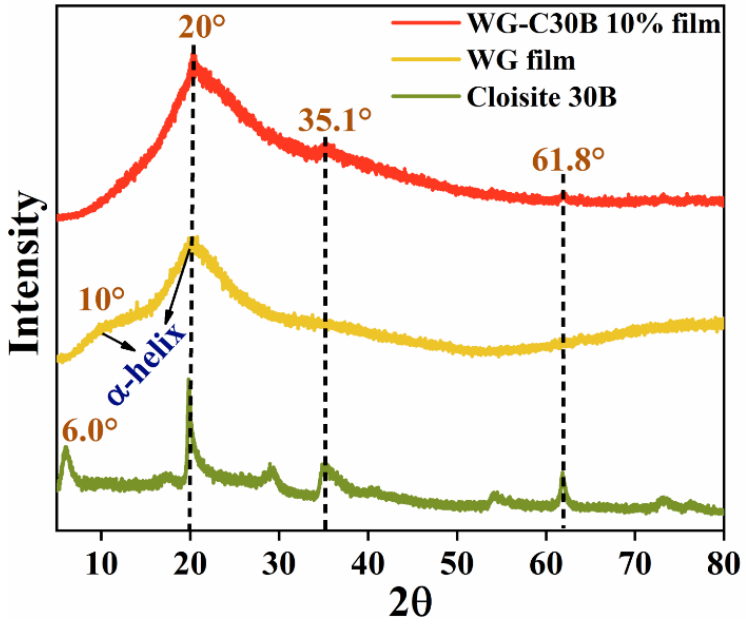


**Fig. 3.2** X-ray diffraction (XRD) spectra of C30B, WG, and WG-C30B 10% films

### 3.3.3.2 Field Emission Scanning Electron Microscopy (FESEM)

FESEM was carried out in order to examine the surface morphology of organoclay and cross-sectional views of the films. Micrographs of these materials were presented at two different scales. Surface morphology of the organoclay, C30B, clearly showed multiple silicate layers **(Fig. 3.3a)**. The Fractured surface of the pristine WG i.e., WG film, revealed the presence of an asymmetric porous surface with several holes **(Fig. 3.3b)**. After addition of the clay, pores became negligible; hence, forming a dense structure as shown in **Fig. 3.3c**. Bright/white single/multiple strands along with sheet-like structures revealed the presence of rough surface with partially aggregated clumps in WG-C30B 10% film. In previous reports, similar observations for agglomeration were reported in WG/CNC 12.5% blend at higher CNC (12.5%) concentration [34]. Very likely, strong molecular interactions between amino/hydroxyl groups of gluten protein and hydroxyl groups of C30B particles contributed towards association of the blend. Similar studies were carried out by Liu and co-workers on polyvinyl alcohol/quaternary chitosan composite films [72]. Heterogeneous structure of the film could be due to interference/rupturing of the protein network by organoclay, as proposed in the earlier report [73].

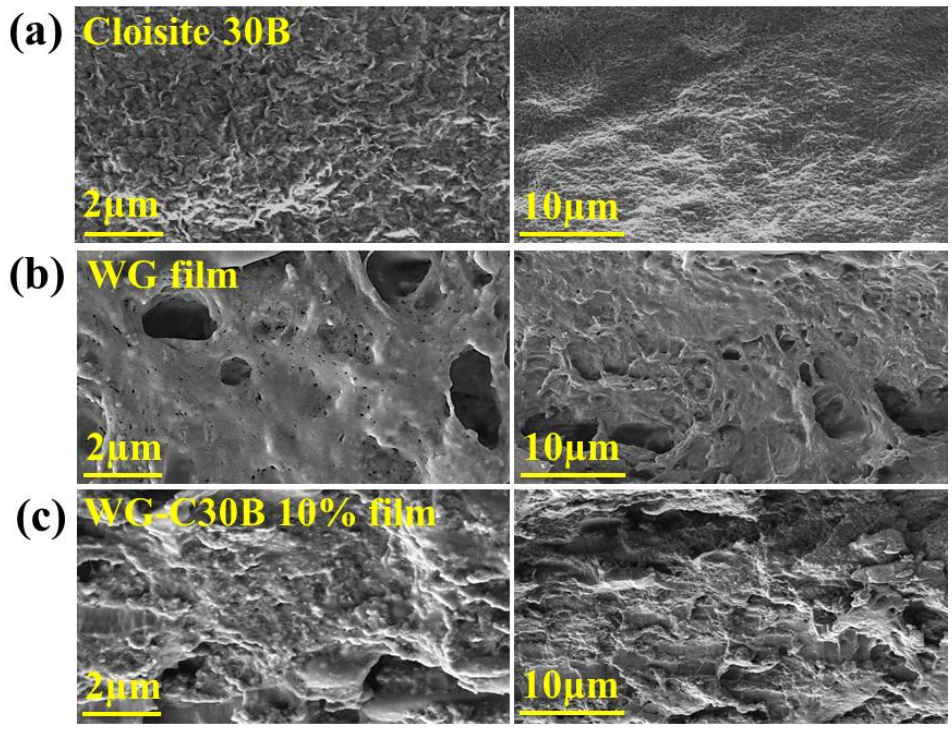


**Fig. 3.3** Field emission scanning electron microscopy **(**FESEM) images of **(a)** Cloisite 30B, **(b)** WG film, and **(c)** WG-C30B 10% film at 2 µm and 10 µm scale

### 3.3.3.3 Atomic Force Microscopy (AFM)

AFM was used to generate both 2-D and 3-D images of the BNC films in order to examine their surface roughness (Sa) and respective root mean square (Sq) values, as shown in **Fig. 3.4(a–d)**. The Sq and Sa values of WG film were found to be 57.622 nm and 41.835 nm, respectively, whereas, for WG-C30B 10% film, the corresponding values were 35.685 nm and 26.414 nm. A significant decrease in both Sq and Sa values of the WG-C30B 10% film was reflected in terms of lowering in its roughness. In earlier reports, it was demonstrated that incorporation of C30B into PVDF matrix reduced the surface roughness from 22.00 to 4.12, indicating improvement in antifouling properties of the blend. Possibly, it was due to partial agglomeration of the clay particles in protein matrix and presence of active functional groups in the plate-like structure of C30B which impacted film surface characteristics [74]. Similar observations were also reported in PES membranes mixed with high-concentration MWCNTs. The surface roughness was decreased from 21.4±1.8 to 10.5±1.2 after loading of 0.04 wt% MWCNTs to the PES matrix. The increased viscosity and reduced pore size led to surface smoothness [75]. The pristine gluten film's roughness was mainly due to some insoluble protein particles. The result was comparable to pectin- and gluten-based films [57]. Overall, the

findings explained why there were non-significant changes in thicknesses of WG and WG-C30B 10% films, as stated in the earlier section.

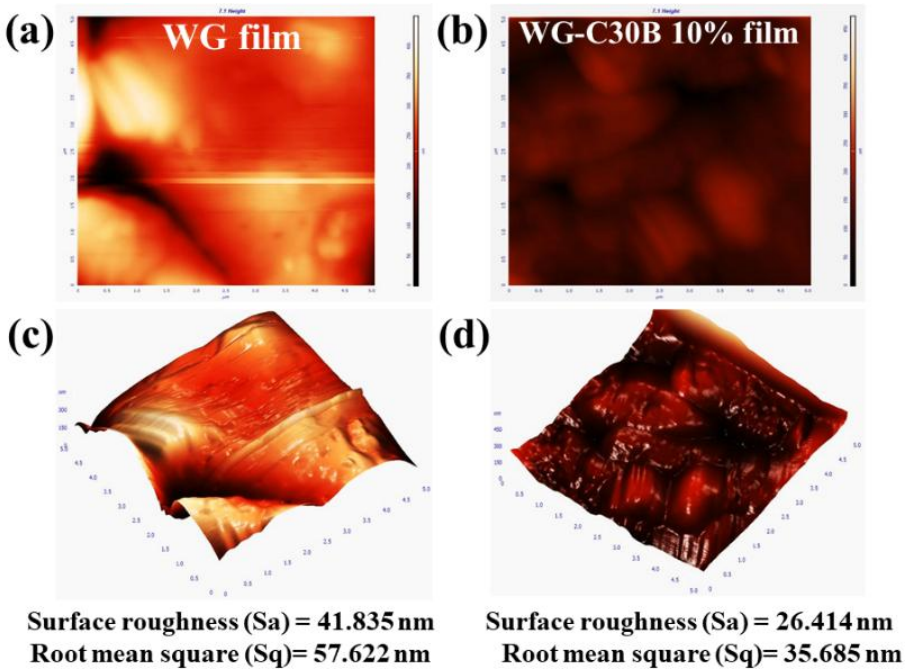


**Fig. 3.4** Atomic force microscopy **(**AFM) images of bionanocomposite films **(a, c)** 2-D & 3-D images of WG film, and **(b, d)** 2-D & 3-D images of WG-C30B 10% film

### 3.3.3.4 Thermogravimetric Analysis (TGA)

The thermal stability of BNC films was analyzed by TGA, as shown in **Fig. 3.5**. Step-wise thermal degradation of C30B and the films was distinctly noticeable in a temperature range of 25–800°C. First step was associated with the process of water loss below 150°C. In next step, multiple changes like breakdown of peptide bonds in the protein matrix, decomposition of organic components of C30B, and loss of glycerol occurred at 200–500°C temperature range. As evident from the literature, some wheat gluten/MMT-based nanocomposites and starch/mineral clay-based films also showed similar trend [35,76]. In the last step of thermal degradation process (500–800 °C), significant chemical changes such as oxidation of partially decomposed WG protein and dehydroxylation of C30B organoclay occured. The residual mass of WG film was around 5%, whereas, it increased to 22% for WG-C30B 10% film. Such an increase in thermal stability in the oxidative atmosphere could be due to physical barrier effect of layered silicates in the protein matrix and superficial flame combustion zone. The results were found to be significant than earlier reports on wheat gluten (WG)/cellulose nanofibrils (CNF) and nanocrystals (CNC)-based BNCs where residual masses for 3% CNC and

3% CNF-loaded WG film were 18.2% and 20.3%, respectively, while it was 21.1% for wheat gluten (WG)/lignin nanopacticles (LNP)-based BNCs (WG/3LNP) [60,77].

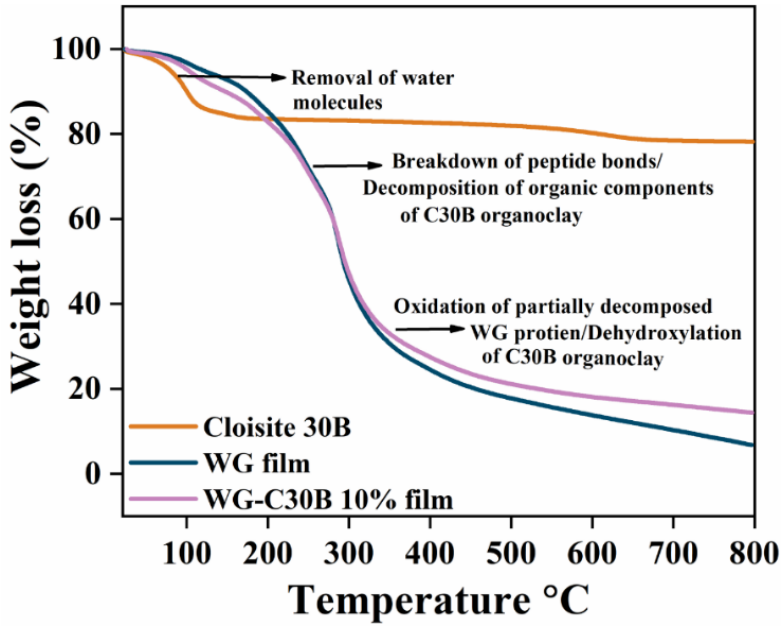


**Fig. 3.5** Thermal degradation spectra of C30B, WG, and WG-C30B 10% films

### 3.3.4 Determination of Antibacterial Properties of BNC films

Unmodified and organically modified clays were known to vary in antimicrobial activities depending on bacterial species. As evident from earlier reports, C30B organoclay was successfully used as nanofiller in the packaging films, showing antibacterial properties. The WG-C30B 10% film discs clearly showed antibacterial activity against both *S. enterica* and *S. aureus* indicating the effect of nanofiller **(Fig. 3.6)** and the corresponding inhibition zones were found to be 13 mm and 9 mm, respectively; whereas, there was no zone of inhibition in case of WG film. Both the bacterial strains were sensitive to tetracycline [78,79] which was used as a positive control in order to validate the antibacterial efficacy of the prepared BNC films. Quaternary ammonium i.e., alkyl ammonium groups present in C30B silicate layers, could potentially disrupt bacterial cell envelope, cell wall in particular, causing cell lysis [27]. Usually, bacterial cell walls attain a net negative charge under normal physiological conditions due to carboxyl groups [80]. Therefore, due to mutual attractions, electrostatic interactions between clay minerals of BNC films and bacterial cell surface appeared to be crucial for their proximity. Moreover, hydrophobic interactions could considerably augment the process of attachment and disruption. The organoclay component of BNC film exhibited antimicrobial activity due to direct surface contact with food materials. For example, poly (e-

caprolactone)/cloisite 30B thin films were found to be effective against *S. haemolyticus* and *S. epidermidi*. The zone of inhibition was in the range of 6–13 mm for both bacterial strains [65]. Among the organically modified MMT nanoclays, C30B appeared effective in antimicrobial activity [23]. Moreover, addition of C30B organoclay into polymer matrices is considered to enhance barrier properties of the films so that microbes fail to penetrate and grow due to tortuous pathways. Therefore, such physical barrier contributes to overall antibacterial activity [65, 81]. Keeping in view, the WG-C30B 10% film appeared to be promising for developing a packaging material with antimicrobial potential. The C30B-blended BNC film of this study could be classified under the 'good category' in view of clear inhibition zones noticed around and under the sample. The result was consistent with the Standard Antibacterial Test "SNV 195920-1992" endorsed by earlier reports [82,83].

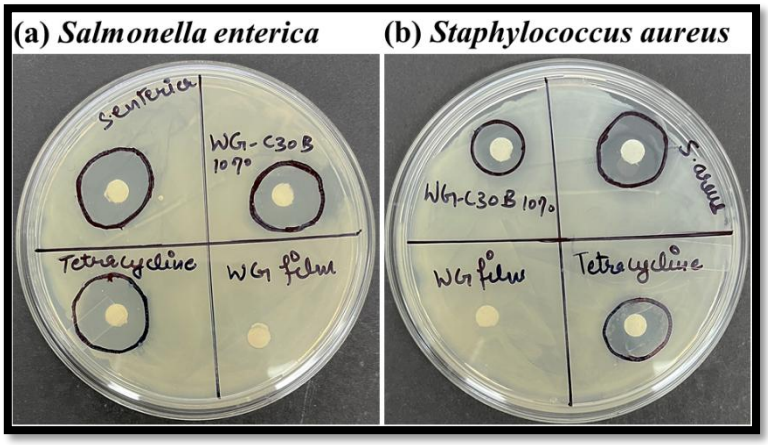


**Fig. 3.6** Antibacterial activities of WG and WG-C30B 10% films (tetracycline used as a positive control) **(a)** *Salmonella enterica,* and **(b)** *Staphylococcus aureus*

### 3.3.5 Daily life applications of BNC films

#### 3.3.5.1 BNC Coatings/Films in the Preservation of Fruits

Both BNC coatings/films were tested to see whether they could effectively preserve green grapes, as depicted in **Scheme 2**. Visual changes were noted under different storage conditions. Surface sterilized green grapes were divided into 5 experimental groups having three grapes in each set: (a) open air (control), (b) dip coated with WG solution, (c) dip coated with WG-C30B 10% solution, (d) wrapped with WG film, and (e) wrapped with WG-C30B 10% film. They were kept under ambient conditions and also in the incubators set at 4 °C and 42 °C as mentioned earlier. At 4 °C, the first three experimental groups, i.e., grapes kept open, dip coated with WG and WG-C30B 10% solutions, exhibited watery surface by the third day;

subsequently, there was a gradual development of brownish-slushy texture by 18$^{th}$ day as shown in **Fig. 3.7A(a–c)**. While the last two experimental groups i.e., grapes wrapped with WG and WG-C30B 10% films, showed a gradual loss in color intensity without losing their firmness throughout the period of observation **(Fig. 3.7Ad and e)**. At low storage temperatures, activities of various metabolic enzymes usually become very low, resulting in a concomitant decline in microbial growth [84]. Similar strategies were adopted earlier with regard to shelf-life extension of cherries with edible coating, and a delay in the degradation of protopectins to soluble pectin and pectic acid was reported [85]. Under ambient conditions, grapes of the first two experimental groups started rotting by third day and intensely deteriorated with a deformed shape by 18$^{th}$ day **(Fig. 3.7Ba and b)**. For dip coating with WG-C30B 10% solution, the grapes gradually deteriorated after 9$^{th}$ day and appeared to be soggy from 15$^{th}$ day onwards **(Fig. 3.7Bc)**. The grapes wrapped with WG film appeared to be squishy and wrinkled due to leakage of sticky juice after 6$^{th}$ day, and turned brownish with a foul smell after 9$^{th}$ day **(Fig. 3.7Bd)**. Interestingly, grapes wrapped with WG-C30B 10% film appeared to be considerably fresh, firm and healthy looking even after storage for more than 2 weeks since the deterioration process remained almost negligible **(Fig. 3.7Be)**. It was demonstrated that grapes retained firmness with WG-C30B 10% film wrapping at both 4°C and ambient conditions which could be due to barrier effects of organoclay particles. As expected, at higher temperature (42 °C), grapes distributed to all five experimental groups started showing the process of decay by 6$^{th}$ day and became worse by 18$^{th}$ day due to extensive dehydration, turning brownish, and distortion in shape as shown in **Fig. 3.7C(a–e)**. Such changes at higher temperature were due to enhanced chemical reaction rates and altered crystallization characteristics in high sugar-containing foods [86]. It was shown that an elevated temperature impacted metabolic rates; for example, synthesis and accumulation of several secondary metabolites such as polyphenols and anthocyanins were affected [87]. At higher temperature, probably the effects of organoclay remained negligible. Dip coating method had some drawbacks, possibly due to non-uniform thickness of the coating layers, reduction in respiration of products, damage of fruit surface, and various environmental factors including microbial loads resulting in gradual loss of coating materials as proposed in earlier reports [88,89]. Keeping in view, wrapping with films appeared to be more effective as this process isolated the grapes from microbial exposure in the external environment. This study suggested that C30B-blended BNC film with superior protection properties and antimicrobial activities could be a promising packaging material under ambient conditions. Our findings were consistent with

earlier reports on the shelf-life extension of green grapes by wrapping them with agar/ZnO nanoparticle-based films under ambient conditions [90].

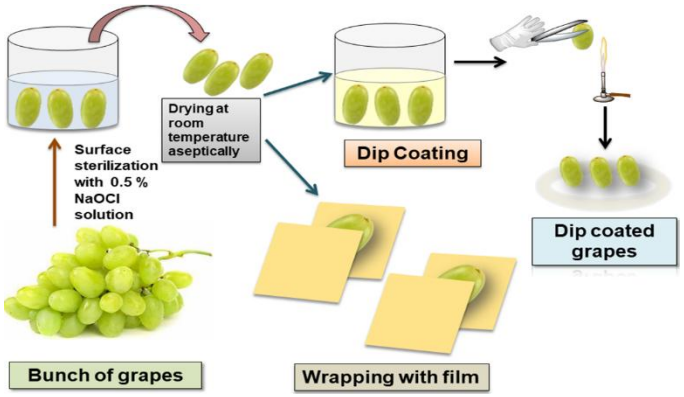


**Scheme 3.2** A schematic representation of dip coating and wrapping methods for shelf-life extension of green grapes.

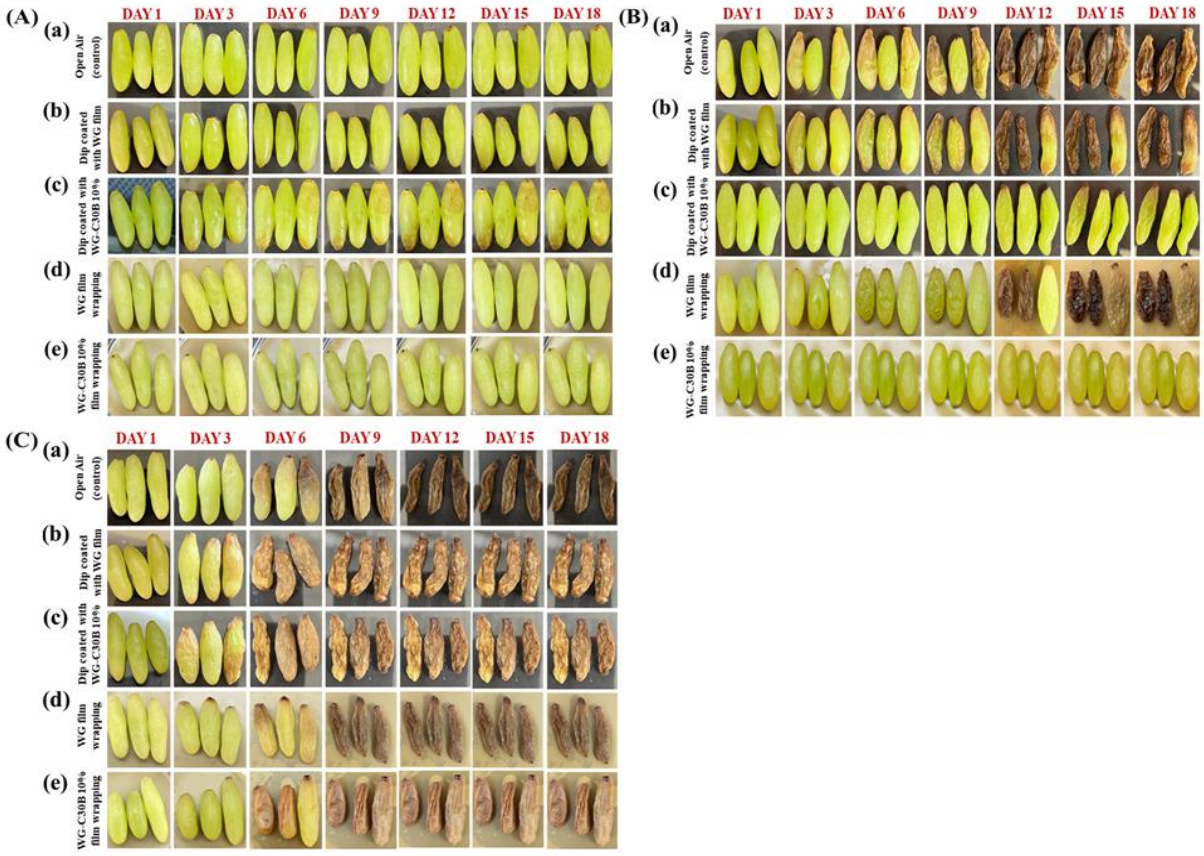


**Fig. 3.7** Effects of dip coating and wrapping on green grapes during storage under (A) 4 °C, (B) ambient conditions, and (C) 42 °C. Experimental groups: (a) open air (control), (b) dip coated with WG solution, (c) dip coated with WG-C30B 10% solution, (d) wrapped with WG film, and (e) WG-C30B 10% film

### 3.3.5.2 Biodegradability of BNC Films in Soil

Biodegradation of natural polymers occurs in the environment due to concerted biological, chemical, mechanical and other factors. Such processes are responsible for the changes in their chemical structures and generation of various products [91]. Soil burial is a widely used method for studying biodegradation of different polymeric materials under field conditions. It has become a common practice of waste disposal [92]. The biodegradability test of BNC films was carried out in agricultural and sewage-sludge soils. As shown in Fig. 8a and b, there was a gradual biodegradation of films in agricultural soil over a given period; however, the process was visibly rapid in the case of sewage-sludge soil **(Fig. 3.8c and d)**. The extent of biodegradation of films was negligible in both sterile/heat-treated soil samples (data not shown). Similar trends were showed in soy protein isolates/MgAl LDH-based BNC films and cassava starch- corn starch-based bioplastics on biodegradation in soil [41, 44]. Various environmental factors such as moisture content, soil pH, inorganic/organic matters, and diverse microbes contributed to biodegradation of the films. Extent of weight loss was considered to be an indicator of degradation of a film in agricultural soil. Overall weight loss was noted on every third day after burial, and the process continued up to 12 days. WG and WG-C30B 10% films showed approximately 72% and 56% weight loss ($p$ = 0.000), respectively **(Fig. 3.9)**. In other words, the latter film was slowly biodegraded. Antimicrobial properties of the organoclay could be a hindrance for microbes in terms of their access and subsequent metabolic degradation of the BNCs in soils. Multiple factors were considered to impact complex degradation process of BNCs/various polymer-based composites in the soil, such as their physico-chemical properties, light, moisture, pH, temperature, aerobic/anaerobic conditions, different inorganic/organic molecular constituents, metabolic activities of diverse microbial population [93].

As evident from the findings, there was a considerable difference between the processes of biodegradation of BNC films between agricultural and sewage-sludge soils. Sewage sludge is rich in vast and diverse microbes including bacteria, fungi and other species that could rapidly metabolize various organic materials and polymeric substances [94]. Nutrient-rich sewage sludge with high moisture content triggered various microbial metabolic activities associated with rapid biodegradation of the BNC films. Under such situation, potential antimicrobial activity of the films remained insignificant. On the other hand, the distribution and overall activities of microorganisms in an agricultural soil depend upon various factors such as soil texture, pH, porosity, nature of nutrients, plant roots along with other biomass/debris including their breakdown products. An agricultural soil could be rich with regard to microbial load, but

it might lack diverse microbes, particularly BNC degrading ones [95]. The moisture content of such soil mostly depends on irrigation and weather patterns; usually microbial activities get significantly reduced during dry periods. All these factors could be responsible for slowdown in the process of biodegradation of BNC films in agricultural soil [96, 97].

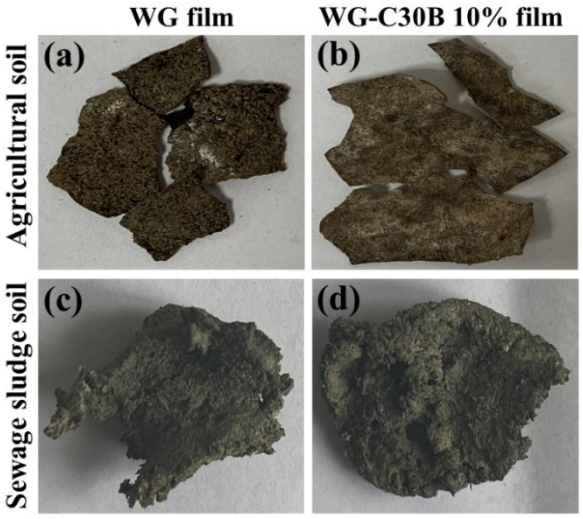


**Fig. 3.8** Biodegradation of WG-C30B-based bionanocomposite films in **(a, b)** agricultural soil, and **(c, d)** sewage-sludge soil

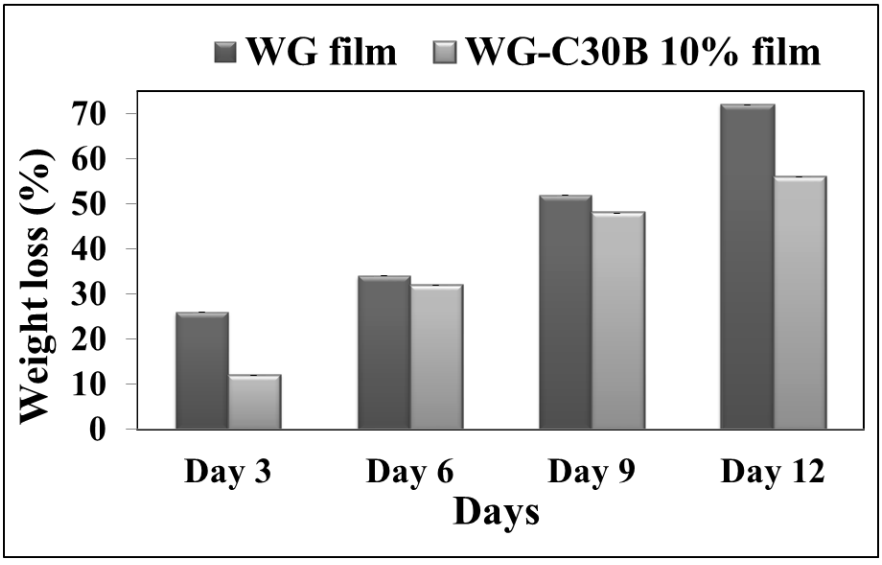


**Fig. 3.9** Weight loss of bionanocomposite films during the process of biodegradation in agricultural soil (mean ± standard deviation)

## 3.4 Conclusion

In this study, wheat gluten/cloisite 30B-based BNC films were successfully prepared using a simple and reproducible solution casting method. Subsequently, effects of the organoclay on

protein matrix were investigated. The XRD, FESEM and AFM data clearly reflected interactions between C30B and the WG matrix because of intercalation/exfoliation of sheet-like organoclay structure. WG-C30B 10% film showed desirable mechanical properties like tensile strength and elongation at break in comparison to WG film. The former also appeared to be promising in terms of water sensitivity as its moisture content and water solubility were significantly lowered compared to the latter one. These findings exhibited more effectiveness than the previous studies on wheat gluten-based BNC films. Moreover, the organoclay nanofiller was found to render considerable hydrophobicity and thermal stability to the WG-C30B 10% film. This film showed antibacterial activity against *S. enterica* and *S. aureus*. The physical changes in green grapes were monitored under different storage conditions; ambient conditions along with incubators set at 4 °C, and 42 °C. At 4 °C, grapes wrapped with films maintained their firmness but showed gradual changes in color intensities, most likely due to lowering of enzyme activities. Under ambient conditions, wrapping with WG-C30B 10% film ensured shelf-life extension of green grapes by maintaining some desirable qualities such as color, firmness, and healthy look up to 18 days. In comparison to wrapping, dip coating with WG-C30B 10% solution appeared to be less effective as the grapes began to deteriorate after 9 days. Grapes were unable to withstand storage at higher temperature (42 °C) as there was rapid deterioration. There was no such report regarding preservation of green grapes under different storage conditions using these methods for a duration of 18 days. The prepared BNC films were found to be biodegradable in both normal agricultural and sewage-sludge soils. In conclusion, this study would be useful in preparing biodegradable biopolymer-based packaging materials with desirable physico-chemical properties for preservation of different fruits/vegetables and other food products.

## References


1. Fathima PE, Panda SK, Ashraf PM, Varghese TO, Bindu J (2018) Polylactic acid/chitosan films for packaging of Indian white prawn (Fenneropenaeus indicus). Inter J Biol Macromol 117:1002–1010. https://doi.org/10.1016/j.ijbiomac.2018.05.214
2. Groh KJ, Backhaus T, Carney-Almroth B, Geueke B, Inostroza PA, Lennquist A, Leslie HA, Maffini M, Slunge D, Trasande L, Warhurst AM (2019) Overview of known plastic packaging-associated chemicals and their hazards. Sci Total Environ 651:3253–68. https://doi.org/10.1016/-j.scitotenv.2018.10.015
3. Indumathi MP, Sarojini KS, Rajarajeswari GR (2019) Antimicrobial and biodegradable chitosan/cellulose acetate phthalate/ZnO nano composite films with optimal oxygen permeability

and hydrophobicity for extending the shelf life of black grape fruits. Inter J Biol Macromol 132:1112–1120. https://doi.org/10.1016/j.ijbiomac.2019.03.171

4. Pandey VK, Upadhyay SN, Niranjan K, Mishra PK (2020) Antimicrobial biodegradable chitosan-based composite Nano-layers for food packaging. Inter J Biol Macromol 157:212–219. https://doi.org/10.1016/j.ijbiomac.2020.04.149
5. Kumar S, Basumatary IB, Sudhani HPK, Bajpai VK, Chen L, Shukla S, Mukherjee A (2021) Plant extract mediated silver nanoparticles and their applications as antimicrobials and in sustainable food packaging: A state-of-the-art review. Trends Food Sci Technol 112:651–666. https://doi.org/10.1016-/j.tifs.2021.04.031
6. Severo C, Anjos I, Souza VGL, Canejo JP, Bronze MR, Fernando AL, Coelhoso I, Bettencourt AF, Ribeiro IA, Ribeiro IAC (2021) Development of cranberry extract films for the enhancement of food packaging antimicrobial properties. Food Packag Shelf Life 28:100646. https://doi.org/10.1016/-j.fpsl.2021.100646
7. Kaewprachu P, Osako K, Benjakul S, Tongdeesoontorn W, Rawdkuen S (2016) Biodegradable protein-based films and their properties: a comparative study. Packag Technol Sci 29(2):77–90. https://doi.org/10.1002/pts.2183
8. CJR Verbeek, LE van den Berg (2010) Extrusion processing and properties of protein-based thermoplastics. Macromol Mater Eng 295(1):10–21. https://doi.org/10.1002/mame.200900167
9. Zink J, Wyrobnik T, Prinz T, Schmid M, (2016) Physical, "Chemical and biochemical modifications of protein-based films and coatings: An extensive review. Inter J Biol Macromol 17(9):1376. https://doi.org/10.3390/ijms17091376
10. Domenek S, Feuilloley P, Gratraud J, Morel MH, Guilbert S (2004) Biodegradability of wheat gluten based bioplastics. Chemosphere 54(4):551–559. https://doi.org/10.1016/S0045-6535(03)00760-4
11. Mojumdar S, Moresoli C, Simon L, Legge R (2011) Edible wheat gluten (WG) protein films. J Therm Analy Calor 104(3):929–936. https://doi.org/10.1007/s10973-011-1491-z
12. Ansorena MR, Zubeldía F, Marcovich NE (2016) Active wheat gluten films obtained by thermoplastic processing. LWT- Food Sci Technol 69:47–54. https://doi.org/10.1016-/j.lwt.2016.01.020
13. Zhang Y, Deng L, Zhong H, Zou Y, Qin Z, Li Y, Zhang H (2022) Impact of glycation on physical properties of composite gluten/zein nanofibrous films fabricated by blending electro spinning. Food Chem 366:130586. https://doi.org/10.1016/j.foodchem.2021.130586
14. Olabarrieta I, Cho SW, Gallstedt M, Sarasu JR, Johansson E, Hedenqvist MS (2006) Aging properties of films of plasticized vital wheat gluten cast from acidic and basic solutions. Biomacromol 7(5):1657–1664. https://doi.org/10.1021/bm0600973
15. Chen L, Reddy N, Wu X, Yang Y (2012) Thermoplastic films from wheat proteins," Ind Crops Prod 35(1):70–76. https://doi.org/10.1016/j.indcrop.2011.06.009

16. Williams LB, Holland M, Eberl DD, Brunet T, Brunet de Courrsou L (2004) Killer clays. Natural antibacterial clay minerals. Mineral Soci Bull 139:3–8.
17. Youssef AM, El-Sayed SM (2018) Bionanocomposites materials for food packaging applications: Concepts and future outlook. Carbohydr Polym 193:19–27. https://doi.org/10.1016/-j.carbpol.2018.03.088
18. Perera KY, Hopkins M, Jaiswal AK, Jaiswal S (2024) Nanoclays-containing bio-based packaging materials: Properties, applications, safety, and regulatory issues. J Nanostr Chem 14(1):71–93. https://doi.org/10.1007/s40097-023-00525-5
19. Peighambardoust SJ, Zahed-Karkaj S, Peighambardoust SH, Ebrahimi Y, Peressini D (2020) Characterization of carboxymethyl cellulose-based active films incorporating non-modified and Ag or Cu-modified Cloisite 30B and montmorillonite nanoclays. Iran Polym J 29:1087–1097. https://doi.org/10.1007/s13726-020-00863-z
20. Khashayary S, Aarabi A (2021) Evaluation of physico-mechanical and antifungal properties of gluten-based film incorporated with vanillin, salicylic acid, and montmorillonite (Cloisite 15A). Food Bioproc Technol 14(4):665–678. https://doi.org/10.1007/s11947-021-02598-y
21. Ray SS, Okamoto M (2003) Polymer/layered silicate nanocomposites: a review from preparation to processing. Prog Polym Sci 28(11):1539–1641. https://doi.org/10.1016/-j.progpolymsci.2003.08.002
22. Alexandre M, Dubois P (2000) Polymer-layered silicate nanocomposites: preparation, properties and uses of a new class of materials. Mater Sci Eng: R: Reports 28(1–2):1–63. https://doi.org/10.1016/S0927-796X(00)00012-7
23. Hong SI, Rhim JW (2008) Antimicrobial activity of organically modified nanoclays. J Nanosci Nanotechnol 8(11):5818–5824. https://doi.org/10.1166/jnn.2008.248
24. Nigmatullin R, Gao F, Konovalova V (2009) Permanent, Non-Leaching Antimicrobial Polyamide Nanocomposites Based on Organoclays Modified with a Cationic Polymer. Macromol Mater Eng 294(11):795–805. https://doi.org/10.1002/mame.200900166
25. Parolo ME, Fernandez LG, Zajonkovsky I, Sánchez MP, Baschini M (2011) Antibacterial activity of materials synthesized from clay minerals. Science against Microbial Pathogens: Communicating Current Research and Technological Advances 1:144–51.
26. de Azeredo HM (2013) Antimicrobial nanostructures in food packaging. Trends Food Sci Technol 30(1):56–69. https://doi.org/10.1016/j.tifs.2012.11.006
27. Rhim JW, Hong SI, Park HM, Ng PK (2006) Preparation and characterization of chitosan-based nanocomposite films with antimicrobial activity. J Agri Food Chem 54:5814–5822. https://doi.org/10.1021/jf060658h
28. Bumbudsanpharoke N, Ko S (2015) Nano-food packaging: an overview of market, migration research, and safety regulations. J Food Sci 80(5):910–923. https://doi.org/10.1111/1750-3841.12861

29. Otoni CG, Avena-Bustillos RJ, Azeredo HMC, Lorevice MV, Moura MR, Mattoso LHC, McHugh TH (2017) Recent advances on edible films based on fruits and vegetables— a review. Comprehensive Review on Food Science and Food Safety 16:1151–69. https://doi.org/10.1111/1541-4337.12281
30. Wu CT (2010) An overview of postharvest biology and technology of fruits and vegetables. Technology on Reducing Post-harvest Losses and Maintaining Quality of Fruits and Vegetables Proceedings of 2010 AARDO Workshop 2–11. https://scholars.tari.gov.tw/-handle/123456789/2621
31. Bodbodak S, Z Rafiee (2016) Recent trends in active packaging in fruits and vegetables. Eco-Friendly Technology for Postharvest Produce Quality: 77–125. https://doi.org/10.1016/B978-0-12-804313-4.00003-7
32. Li JH, Hong RY, Li MY, Li HZ, Zheng Y, Ding J (2009) Effects of ZnO nanoparticles on the mechanical and antibacterial properties of polyurethane coatings. Prog Org Coat 64(4):504–509. https://doi.org/10.1016/j.porgcoat.2008.08.013
33. Kanmani P, Rhim JW (2014) Physical, mechanical and antimicrobial properties of gelatin based active nanocomposite films containing AgNPs and nanoclay. Food Hydrocoll 35:644–652. https://doi.org/10.1016/j.foodhyd.2013.08.011
34. El-Wakil NA, Hassan EA, Abou-Zeid RE, Dufresne A (2015) Development of wheat gluten/nanocellulose/titanium dioxide nanocomposites for active food packaging. Carbohydr polym 124:337–346. https://doi.org/10.1016/j.carbpol.2015.01.076
35. Tunc S, Angellier H, Cahyana Y, Chalier P, Gontard N, Gastaldi E (2007) Functional properties of wheat gluten/montmorillonite nanocomposite films processed by casting. J Membr Sci 289(1–2):159–168. https://doi.org/10.1016/j.memsci.2006.11.050
36. Ture H, Blomfeldt TO, Gallstedt M, Hedenqvist MS (2012) Properties of wheat-gluten/montmorillonite nanocomposite films obtained by a solvent-free extrusion process. J Polym Environ 20:1038–1045. https://doi.org/10.1007/s10924-012-0506-6
37. Caner C, Rahvali F, Yuceer M, Oral A (2023) Effects of types and concentrations of modified Cloisite Clays on properties of chitosan nanocomposites for food packaging. Polym Adv Technol 34(7):2248–2260. https://doi.org/10.1002/pat.6045
38. Sothornvit R, Rhim JW, Hong SI (2009) Effect of nano-clay type on the physical and antimicrobial properties of whey protein isolate/clay composite films. J Food Eng 91(3):468–473. https://doi.org/10.1016/j.jfoodeng.2008.09.026
39. Salarbashi D, Tafaghodi M, Bazzaz BSF, Bazeli J (2018) Characterization of a green nanocomposite prepared from soluble soy bean polysaccharide/Cloisite 30B and evaluation of its toxicity. Inter J Biol Macromol 120:109–118. https://doi.org/10.1016/-j.ijbiomac.2018.07.183

40. BŞ Kayserilioglu, Bakir U, Yilmaz L, Akkaş N (2003) Drying temperature and relative humidity effects on wheat gluten film properties. J Agri Food Chem 51(4): 964–968. https://doi.org/10.1021/-jf0205817
41. Sharma S, Das N, Pal B (2023) Preparation, characterization, and application of soy protein isolate/Mg–Al layered double hydroxide-based bionanocomposite films. Cheml Pap 77(6):3265–3275. https://doi.org/10.1007/s11696-023-02702-w
42. Muller CMO, Yamashita F, Laurindo JB (2008) Evaluation of the effects of glycerol and sorbitol concentration and water activity on the water barrier properties of cassava starch films through a solubility approach. Carbohydr Polym 72(1):82–87. https://doi.org/10.1016/-j.carbpol.2007.07.026
43. Rangel-Marrón M, Montalvo-Paquini C, Palou E, López-Malo (2013) A Optimization of the moisture content, thickness, water solubility and water vapor permeability of sodium alginate edible films. Recent advances in chemical engineering, Biochemistry and computational chemistry 72–78.
44. Zoungranan Y, Lynda E, Dobi-Brice KK, Tchirioua E, Bakary C, Yannick DD (2020) Infuence of natural factors on the biodegradation of simple and composite bioplastics based on cassava starch and corn starch. J Environ Chem Eng 8(5):104–396. https://doi.org/10.1016/-j.jece.2020.104396
45. Mehmood Z, Sadiq MB, Khan MR (2020) Gelatin nanocomposite films incorporated with magnetic iron oxide nanoparticles for shelf life extension of grapes. J Food Safety 40(4):12814. https://doi.org/10.1111/jfs.12814
46. Taheri N, Sayyahi S (2016) Effect of clay loading on the structural and mechanical properties of organoclay/HDI-based thermoplastic polyurethane nanocomposites. e-Polym 16(1):65–73. https://doi.org/10.1515/epoly-2015-0130
47. Becker CM, Gabbardo AD, Wypych F, Amico SC (2011) Mechanical and flame-retardant properties of epoxy/Mg–Al LDH composites. Compos Appl Sci 42(2):196–202. https://doi.org/10.1016/-j.compositesa.2010.11.005
48. Tseng CH, Hsueh HB, Chen CY (2007) Effect of reactive layered double hydroxides on the thermal and mechanical properties of LDHs/epoxy nanocomposites. Compos Sci Technol 67(11–12):2350–62. https://doi.org/10.1016/j.compscitech.2007.01.011
49. Ensminger LE, Gieseking JE (1939) The absorption of proteins by montmorillonitic clays. Soil Sci 48(6):467.
50. Ensminger LE, Gieseking JE (1941) The absorption of proteins by montmorillonitic clays and its effect on base-exchange capacity. Soil Sci 51(2):125.
51. Ali F, Ullah H, Ali Z, Rahim F, Khan F, Rehman ZU (2016) Polymer-clay nanocomposites, preparations and current applications: a review. Current Nanomaterials 1(2):83–95.
52. Patil NB, Sharanagouda H, Doddagoudar SR, Ramachandra CT, Ramappa KT (2019) Effect of rice husk silica nanoparticles on physical and mechanical properties of soy protein isolate packaging films. Inter J Chem Studies 7(6):2272–2277.

53. Rhim JW, Lee JH, Kwak HS (2005) Mechanical and water barrier properties of soy protein and clay mineral composite films. Food Sci Biotechnol 14(1):112–116.
54. Echeverría I, Eisenberg P, Mauri AN (2014) Nanocomposites films based on soy proteins and montmorillonite processed by casting. J Membr Sci 449:15–26. https://doi.org/10.1016/-j.memsci.2013.08.006
55. Y Xiao, Y Liu, S Kang, Wang K, Xu H (2020) Development and evaluation of soy protein isolate-based antibacterial nanocomposite films containing cellulose nanocrystals and zinc oxide nanoparticles. Food Hydrocoll 106:105898. https://doi.org/10.1016/-j.foodhyd.2020.105898
56. Bourtoom T, Chinnan MS (2008) Preparation and properties of rice starch–chitosan blend biodegradable film. LWT- Food Sci Technol 41(9):1633–1641. https://doi.org/10.1016/-j.lwt.2007.10.014
57. Sartori T, Feltre G, do Amaral Sobral PJ, da Cunha RL, Menegalli FC (2018) Properties of films produced from blends of pectin and gluten. Food Packag Shelf Life 18:221–229. https://doi.org/10.1016/j.fpsl.2018.11.007
58. Menghan F, Cao M, Duan J, Zhou Q, Dong M, Zhang T, Liu X, Duan X (2022) Research on the Properties of Zein, Soy Protein Isolate, and Wheat Gluten Protein-Based Films Containing Cellulose Nanocrystals. Foods 11(19):3010. https://doi.org/10.3390/foods11193010
59. Dashipour A, Razavilar V, Hosseini H, Shojaee-Aliabadi S, German JB, Ghanati K, Khakpour M, Khaksar R (2015) Antioxidant and antimicrobial carboxymethyl cellulose films containing Zataria multiflora essential oil. Inter J Biol Macromol 72: 606–613. https://doi.org/10.1016/-j.ijbiomac.2014.09.006
60. Yang W, Kenny JM, Puglia D (2015) Structure and properties of biodegradable wheat gluten bionanocomposites containing lignin nanoparticles. Ind Crops Prod 74:348–356. https://doi.org/10.1016/j.indcrop.2015.05.032
61. Tunc S, Duman O (2010) Preparation and characterization of biodegradable methyl cellulose/montmorillonite nanocomposite films. Appl Clay Sci 48(3):414–424. https://doi.org/10.1016/j.clay.2010.01.016
62. Han JH, Krochta JM (1999) Wetting properties and water vapor permeability of whey-protein-coated paper. Trans ASAE 42: 1375–1382, 10.13031/2013.13300.
63. Angellier-Coussy H, Chalier P, Gastaldi E, Guillard V, Guillaume C, Gontard N, Peyron S (2013) Protein-Based Nanocomposites for Food Packaging. Biopolymer nanocomposites: processing, properties, and applications: 613–654. https://doi.org/10.1002/-9781118609958.ch25
64. Lin JJ, Chan YN, Lan YF (2010) Hydrophobic modification of layered clays and compatibility for epoxy nanocomposites. Materials 3(4):2588–2605. https://doi.org/10.3390/ma3042588
65. Babu SS, Mathew S, Kalarikkal N, Thomas S (2016b) Antimicrobial, antibiofilm, and microbial barrier properties of poly (ε-caprolactone)/cloisite 30B thin films. 3 Biotech 6:249. https://doi.org/10.1007/s13205-016-0559-7

66. Oymaci P, Altinkaya SA (2016) Improvement of barrier and mechanical properties of whey protein isolate based food packaging films by incorporation of zein nanoparticles as a novel bionanocomposite. Food Hydrocoll 54:1–9. https://doi.org/10.1016/j.foodhyd.2015.08.030
67. Serbezeanu D, Bercea M, Butnaru M, Enache AA, Rîmbu CM, Vlad-Bubulac T (2022) Development of histamine reinforced poly (vinyl alcohol)/chitosan blended films for potential biomedical applications. J Appl Polym Sci 139(14):51912. https://doi.org/10.1002/app.51912
68. Kuktaite R, Plivelic TS, Ture H, Hedenqvist MS, Gallstedt M, Marttila S, Johansson E (2012) Changes in the hierarchical protein polymer structure: Urea and temperature effects on wheat gluten films. RSC Adv 2(31):11908–11914.
69. Shishavan SM, Azdast T, Ahmadi SR (2014) Investigation of the effect of nanoclay and processing parameters on the tensile strength and hardness of injection molded acrylonitrile butadiene styrene–organoclay nanocomposites. Mater Des 58:527–534. https://doi.org/10.1016/j.matdes.2014.02.014
70. Shahvalizadeh R, Ahmadi R, Davandeh I, Pezeshki A, Moslemi SAS, Karimi S, Rahimi M, Hamishehkar H, Mohammadi M (2021) Antimicrobial bio-nanocomposite films based on gelatin, tragacanth, and zinc oxide nanoparticles–Microstructural, mechanical, thermo-physical, and barrier properties. Food Chem 354:129492. https://doi.org/10.1016/-j.foodchem.2021.129492
71. SS Babu, A Augustine, N Kalarikkal, S Thomas (2016a) Nylon 6, 12/cloisite 30B electrospun nanocomposites for dental applications J Sib Fed Uni Biol 29:198. https://elib.sfu-kras.ru/handle/2311/20366
72. Liu F, Zhang X, Xiao X, Duan Q, Bai H, Cao Y, Zhang Y, Alee M, Yu L (2023) Improved hydrophobicity, antibacterial and mechanical properties of polyvinyl alcohol/quaternary chitosan composite films for antibacterial packaging. Carbohydr Polym 312:120755. https://doi.org/10.1016-/j.carbpol.2023.120755
73. Song NB, Jo WS, Song HY, Chung KS, Won M, Song KB (2013) Effects of plasticizers and nano-clay content on the physical properties of chicken feather protein composite films. Food Hydrocoll 31(2):340–345. https://doi.org/10.1016/j.foodhyd.2012.11.024
74. Dehghankar M, Mohammadi T, Tavakolmoghadam M, Tofighy MA (2021) Polyvinylidene fluoride/nanoclays (cloisite 30B and palygorskite) mixed matrix membranes with improved performance and antifouling properties. Ind Eng Chem Research 60(32):12078–12091. https://doi.org/10.1021/acs.iecr.1c01656
75. Vatanpour V, Madaeni SS, Moradian R, Zinadini S, Astinchap B (2011) Fabrication and characterization of novel antifouling nanofiltration membrane prepared from oxidized multiwalled carbon nanotube/polyethersulfone nanocomposites. J Membr Sci 375(1–2):284–294. https://doi.org/10.1016/j.memsci.2011.03.055
76. Wilhelm HM, Sierakowski MR, Souza GP, Wypych F (2003) Starch films reinforced with mineral clay. Carbohydr Polym 52(2):101–110. https://doi.org/10.1016/S0144-8617(02)00239-4

77. Fortunati E, Luzi F, Jiménez A, Gopakumar DA, Puglia D, Thomas S, Kenny JM, Chiralt A, Torre L (2016) Revalorization of sunflower stalks as novel sources of cellulose nanofibrils and nanocrystals and their effect on wheat gluten bionanocomposite properties. Carbohydr polym 149:357–368. https://doi.org/10.1016/j.carbpol.2016.04.120
78. Srinu B, Vijaya KA, Kumar E, Madhava R (2012) Antimicrobial resistance pattern of bacterial foodborne pathogens. J Chem Pharm Res 4(7):3734–6.
79. Tjaniadi P, Lesmana M, Subekti D, Machpud N, Komalarini S, Santoso W, Simanjuntak CH, Punjabi N, Campbell JR, Alexander WK, Beecham III HJ (2003) Antimicrobial resistance of bacterial pathogens associated with diarrheal patients in Indonesia. Ame J Trop Med Hyg 68(6):666–70.
80. Breen PJ, Compadre CM, Fifer E, Salari H, Serbus DC, Lattin DL (1995) Quaternary ammonium compounds inhibit and reduce the attachment of viable Salmonella typhimurium to poultry tissues. J Food Sci 60(6):1191–1196. https://doi.org/10.1111/j.1365-2621.1995.tb04553.x
81. Busolo MA, Fernandez P, Ocio MJ, Lagaron JM (2010) Novel silver-based nanoclay as an antimicrobial in polylactic acid food packaging coatings. Food Add Contam 27(11):1617–1626. https://doi.org/10.1080/19440049.2010.506601
82. Villanueva ME, Salinas A, Díaz LE, Copello GJ (2015) Chitin nanowhiskers as alternative antimicrobial controlled release carriers. New J Chem 39(1):614–620.
83. Leite LSF, Pham C, Bilatto S, Azeredo HM, Cranston ED, Moreira FK, Mattoso LHC, Bras J (2021) Effect of tannic acid and cellulose nanocrystals on antioxidant and antimicrobial properties of gelatin films. ACS Sustain Chem Eng 9(25):8539–8549. https://doi.org/10.1021/-acssuschemeng.1c01774
84. Michener HD, Elliott RP (1964) Minimum growth temperatures for food-poisoning, fecal-indicator, and psychrophilic microorganisms. Adv Food Research 13:349–396. https://doi.org/10.1016/S0065-2628(08)60103-2
85. Yaman O, Bayoındırlı L (2002) Effects of an edible coating and cold storage on shelf-life and quality of cherries. LWT-Food Sci Technol 35:146–150.
86. Volpe MG, Di Stasio M, Paolucci M, Moccia S (2015) Polymers for Food Shelf-Life Extension. Functional Polymers in Food Science: from Technology to Biology 9–66. 10.1002/9781119109785
87. Blancquaert EH, Oberholster A, Ricardo-da-Silva JM, Deloire AJ (2019) Grape flavonoid evolution and composition under altered light and temperature conditions in Cabernet Sauvignon (Vitis vinifera L.). Fronti Plant Sci 10:1062. https://doi.org/10.3389/-fpls.2019.01062
88. Herrera MA, Sirviö JA, Mathew AP, Oksman K (2016) Environmental friendly and sustainable gas barrier on porous materials: Nanocellulose coatings prepared using spin-and dip-coating. Mater Des 93:19–25. https://doi.org/10.1016/j.matdes.2015.12.127
89. Pirozzi A, Ferrari G, Donsi F (2021) The use of nanocellulose in edible coatings for the preservation of perishable fruits and vegetables. Coatings 11(8):990. https://doi.org/10.3390/-coatings11080990

90. Kumar S, Boro JC, Ray D, Mukherjee A, Dutta J (2019) Bionanocomposite films of agar incorporated with ZnO nanoparticles as an active packaging material for shelf life extension of green grape. Heliyon 5(6). https://doi.org/10.1016/j.heliyon.2019.e01867
91. Pandey JK, Kumar AP, Misra M, Mohanty AK, Drzal LT, Palsingh R (2005) Recent advances in biodegradable nanocomposites. J Nanosci Nanotechnol 5(4):497–526. https://doi.org/10.1166/-jnn.2005.111
92. Dutta S, Karak N, Saikia JP, Konwar B (2010) Biodegradation of epoxy and MF modified polyurethane films derived from a sustainable resource. J Polym Environ 18:167–76. https://doi.org/10.1007/s10924-010-0161-8
93. Karak N (2012) Vegetable oil-based polymers: 2-biodegradable polymers. Woodhead Plublishing.
94. Campanaro AL, Simcik MF, Maurer-Jones MA, Penn RL (2023) Sewage sludge induces changes in the surface chemistry and crystallinity of polylactic acid and polyethylene films. Sci Total Environ 890:164313. https://doi.org/10.1016/j.scitotenv.2023.164313
95. Kyrikou I, Briassoulis D (2007) Biodegradation of agricultural plastic films: a critical review. J Polym Environ 15:125–150. https://doi.org/10.1007/s10924-007-0053-8
96. Othman SH, Ronzi NDA, Shapi'i RA, Dun M, Ariffin SH, Mohammed MAP (2023) Biodegradability of starch nanocomposite films containing different concentrations of chitosan nanoparticles in compost and planting soils. Coatings 13(4):777. https://doi.org/10.3390/-coatings13040777
97. Sander M (2019) Biodegradation of polymeric mulch films in agricultural soils: concepts, knowledge gaps, and future research directions. Environ Sci Technol 53(5):2304–2315. https://doi.org/10.1021/-acs.est.8b05208

# Chapter- 4

## *SPI/ZnAl LDH biocomposites for rapid tartrazine adsorption and evaluation of their antimicrobial activity*

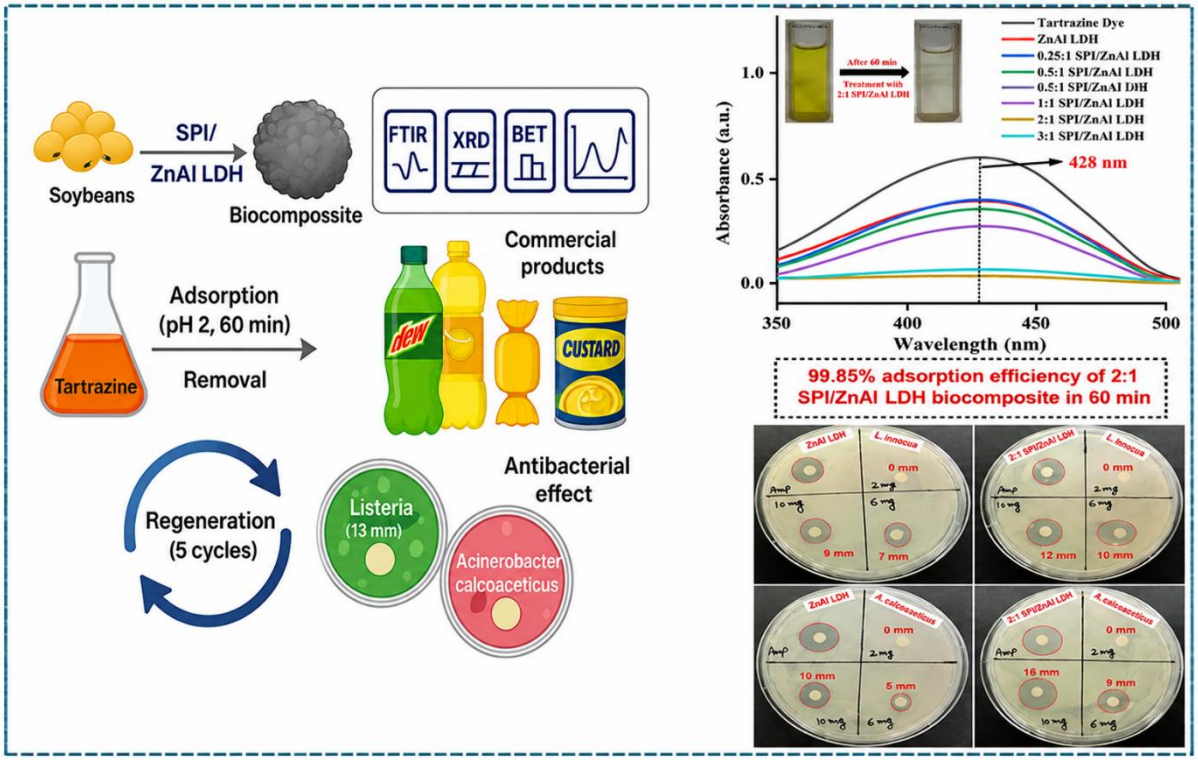


### Schematic Outline:

The schematic view shows synthesis of SPI/ZnAl LDH biocomposites and their comprehensive characterization using structural and surface analysis techniques. It illustrates the efficient adsorption of tartrazine dye from aqueous solutions and commercial food products under optimized conditions, followed by successful regeneration over multiple cycles. Biocomposite exhibited antimicrobial activity against the selected pathogenic bacteria, namely, *Listeria* species and *Acinetobacter calcoaceticus.* It showed multifunctional application in food safety and wastewater treatment.

## 4.1 Introduction

Color significantly influences the consumer decisions in buying commercial products. Food dyes (FDs) refer to chromogenic substances used for centuries to impart colors to food and beverages. Nowadays, food industries mostly prefer synthetic dyes because of their large scale productivity, water solubility, and extensive color range [1]. FDs pose serious risks to the environment and human health [2]. Azo dyes represented a class of predominant synthetic colorants released into the environment. These organic compounds are chemically represented as R–N = N–R', where, R or R' are either aryl or alkyl compounds that typically determine the color intensity and shade of a particular dye. Approximately 800,000 tons of synthetic food dyes are produced annually with azo dyes constituting ~50% of this volume [3,4]. Tartrazine (Tr) called Yellow 5 or E 102, is the most widely used food colorant. It is a highly water-soluble anionic dye synthesized from coal tar as trisodium 5-oxo-1-(4-sulfonatophenyl)-4-[(4-sulfonatophenyl)diazenyl]-4H-pyrazole-3 carboxylate. It is an attractive cost-effective alternative to natural beta-carotene in processed cheese, canned products, beverages, candies, cereals and non-food products. Tr poses significant toxicological risks. Upon entering the body, it is converted to sulfanilic acid through gut microbiota and mammalian azo reductase leading to allergic symptoms including urticaria and asthma [5]. It also triggers dermatitis, eczema, and induces behavioral changes such as irritation or depression [6,7]. Several studies have documented the elemination of tartrazine from wastewater and food products by employing a variety of adsorbents [8–13].

The analytical methods namely Electrochemical Sensor, High Performance Liquid Chromatography, Liquid-liquid extraction and Capillary Electrophoresis were used for quantification and removal of dyes from food products [14–17]. Such methods are complex, cost-intensive, and rely on excessive use of solvents. A precise, reliable, and sensitive method is required to detect low quantities of Tr in food products. The process of adsorption has emerged as a preferred alternative in addressing such limitations as it is associated with minimal byproduct generation, ease of execution, and environmental protection for removal of dyes from wastewater [18,19,20]. Fossil-based synthetic composites and sorbent materials are chemically stable, and hazardous to the life forms due to release of microplastics, polycyclic aromatic hydrocarbons (PAHs) and heavy metals into ecosystems. Also, they produce toxic pollutants like dioxins and furans upon burning. Proper disposal and removal of such composite materials from our surroundings remain a challenging issue [21]. Naturally occurring materials and bionanocomposites are gaining importance as adsorbents due to their cost-effectiveness

and biodegradability [22,23,24]. They are being used as bioadsorbents for various pollutants. For instance, $Ni^{2+}$ and Congo red were eliminated by using crystalline nanocellulose-modified coal bionanocomposites [25].

Protein-based adsorbents are being preferred over polysaccharide-based materials due to their amphiphilic nature and electrostatic charges. Soy protein is a globular protein rich in functional groups such as amino ($-NH_2$), carboxyl ($-COOH$), hydroxyl ($-OH$), and sulfonate groups ($-SO_3H$) that provide active sites for adsorption and chelation of dyes and other contaminants [26]. The incorporation of cellulose nanofibers and nanosilica into SPI-based nanocomposite films led to increased surface hydrophilicity and a corresponding decrease in water contact angle. An increase in surface hydrophilicity enhances adsorption process due to the interactions between adsorbent and aqueous dye molecules [27]. SPI-based composite sponges are porous, and their pore size increases with reduced wall thickness with increment in SPI content. Higher porosity provides more surface area for dye adsorption and improves the overall adsorption capacity of the composites [28]. Out of several types of lamellar solids, LDHs are emerging as anionic clays with general formula: $[(M^{2+})_{1-x}(M^{3+})_x(OH)_2]^{x+}(A^{n-}{}_{x/n})\cdot mH_2O$. ZnAl LDH possesses a layered brucite-like structure with positive charges due to partial substitution of $Al^{3+}$ for $Zn^{2+}$ ions within the octahedral layers. Their interlayer anion exchangeability enables enclosing negatively charged functional biomolecules. They confer chemical stability and biocompatibility [29]. The octahedrally coordinated metal cations with hydroxide ions forming layers can exchange interlayer anions, making them excellent for adsorption [30]. Earlier reports suggested that LDHs and their hybrids demonstrated superior adsorptive properties against hazardous contaminants [31,32]. LDHs have ability to inculcate different antimicrobial agents. The gradual release of these active chemicals enhances the effectiveness of the material with fewer side effects [29]. The general structure of LDH is already shown in **Fig.1.3**.

The SPI integrated biocomposite with ZnAl LDH forms a hybrid material where the porous LDH layers are embedded within or coated by the protein matrix. This combination leverages high surface area, ion-exchange properties of LDHs with the SPI functional groups and biocompatibility which enhances adsorption performance and antimicrobial potential[33,34]. Materials with antimicrobial properties are gaining importance in high-risk areas like public places, food packaging and healthcare facilities as they eliminate microorganisms due to self-sterilizing surfaces [35–39]. For instance, egg albumin and ZnO nanoparticles based biocomposites exhibited antimicrobial effect against multiple bacterial strains [40]. Composites of fenugreek (FNP) and mung bean (MNP) seed proteins with silver nanoparticles (Ag-NPs) demonstrated antimicrobial activity. The MIC values of Ag-FNP were low against

*Salmonella typhimurium* (20 µg/mL) and *Pseudomonas aeruginosa* (10 µg/mL), but higher against *E. coli and Listeria monocytogenes* (162 µg/mL). Ag-MNP showed less MIC (20 µg/mL) for *Staphylococcus aureus*, yet required more concentrations (325 µg/mL) against *Listeria monocytogenes* [41].

Although LDHs and their polymer-based hybrids have been extensively investigated for the adsorption of synthetic dyes, most reported systems rely on polysaccharides, synthetic polymers, or petroleum-derived matrices [42–45], which may suffer from limited biodegradability, secondary pollution, or reduced performance in complex food matrices. The present work reports a new protein-based ZnAl layered double hydroxide (LDH) biocomposite developed using soy protein isolate (SPI) for effective removal of the anionic food dye tartrazine leveraging the diverse functional groups and amphiphilic nature of SPI to enhance dye–adsorbent interactions and adsorption efficiency. Demonstration of dye removal from real commercial food products and food dye wastewater is a notable aspect of this report in comparison to other studies that are restricted to laboratory-prepared dye solutions. In addition, the incorporation of SPI improves the stability of LDH structure under acidic conditions and imparts combined adsorption and antibacterial functionality, enabling effective action against both bacteria. It is shown that SPI with ZnAl LDH can yield a multifunctional bio–inorganic adsorbent capable of simultaneous food-dye removal and antibacterial activity. Considering the growing need for sustainable water-treatment materials, the protein–LDH hybrids are promising. Synthesis of protein-based hybrids, their characterization and performance evaluation under relevant conditions are some of the important aspects of this study.

## 4.2 Materials and methods

### 4.2.1 Materials

#### 4.2.1.1 Analytical materials

Commercial-grade soy protein isolate (SPI, 90% total protein content, dry powder) was purchased from ProFoods, M/s ChemKart (Maharashtra, India). Tartrazine ($C_{16}H_9N_4Na_3O_9S_2$, AR, >99%, dry powder) with molecular weight of 534.36 g $mol^{-1}$, Aluminium nitrate nonahydrate ($Al(NO_3)_3.9H_2O$, 98% extra pure, hygroscopic crystals), Zinc nitrate hexahydrate ($Zn(NO_3)_2.6H_2O$, 98 % AR, hygroscopic flakes), Sodium Hydroxide (NaOH, 97 % extra pure, pellets) and ethanol ($C_2H_6O$, 99.9%, liquid) were procured from Loba Chemie, India. Ampicillin ($C_{16}H_{19}N_3O_4S$, dry powder) was purchased from Himedia, India. Whatman filter

paper was obtained from Global Life Sciences Solutions Operations UK Ltd. Deionized water was purchased from Organo Biotech Laboratories Pvt. Ltd. (New Delhi, India).

#### 4.2.1.2 Biological materials

Dry powdered Luria Broth (LB), Agar Agar Type I were purchased from Himedia, India

#### 4.2.1.3 Commercial food products

Custard powder, yellow candies and mountain dew were procured from Weikfield Foods, Perfetti Van Melle Pvt. Ltd. and PepsiCo, India, respectively.

### 4.2.2 Synthesis of SPI/ZnAl biocomposites

SPI/ZnAl-based biocomposites were synthesized using a simple co-precipitation method, as reported earlier with minor modifications [46]. The Zn/Al ratio was kept at 3:1. Briefly, 1.5 g $Zn(NO_3)_2 \cdot 6H_2O$ and 0.65 g $Al(NO_3)_3 \cdot 9H_2O$ were thoroughly mixed in 50 mL of deionized water for 5 min. A known amount of SPI, i.e. 0.25 g, 0.5 g, 1 g, 2g and 3 g, was dissolved in a separate beaker with 50 mL of deionized water followed by ultra-sonication for 15 min. To prepare the biocomposite solution, mixed metal solution was added to SPI solution and refluxed at 90 °C for 24 h, in order to denature the SPI for effective interactions. Only ZnAl LDH was synthesized using the same method without any addition of SPI. pH of the solutions was maintained at 9.0 by dropwise addition of 1 M NaOH before refluxing. The solid biocomposites, comprising organic and inorganic phases were precipitated. The precipitates were centrifuged at 9000 rpm for 12 min, followed by multiple washes with deionized water and ethanol to remove impurities. The obtained material was dried at 45 °C and ground into fine powder for further use. A schematic representation of synthesis of SPI/ZnAl LDH biocomposites was shown in **Scheme 4.1**.

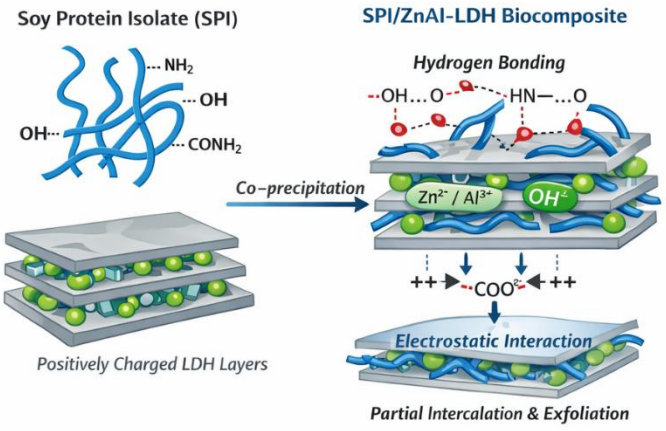


**Scheme 4.1** A schematic representation of synthesis of SPI/ZnAl LDH biocomposites

### 4.2.3 Instrumental characterization techniques

The XRD pattern of powdered ZnAl LDH and SPI/LDH biocomposites was recorded by using a PANalytical-Xpert-Pro (Almelo, Netherlands) diffractometer with Cu K-α (λ=0.154 nm) radiations. The XRD pattern was taken at 2θ = 5°−65° (with step size=0.01°). Crystallinity index (CI) can be calculated by the following equation:

$$\mathrm{CI} = \frac{\mathrm{I_{002}} - \mathrm{I_{AM}}}{\mathrm{I_{002}}} \times 10 \quad (1)$$

Where, $I_{002}$ corresponded to peak intensity of crystalline region and $I_{AM}$ represented peak intensity of amorphous region within the diffractogram from the studied samples.

Fourier transform infrared spectroscopy (FTIR) analysis of grounded ZnAl LDH and SPI/ZnAl LDH biocomposites was done by a Shimadzu IRTracer-100 Fourier Transform Infrared Spectrophotometer, Japan, with ATR mode. The wavelength range was set at 400–3800 $cm^{-1}$, with a scan range of 30 and a spectral resolution of 2 $cm^{-1}$. Surface morphology of as-synthesized ZnAl LDH and SPI/ZnAl LDH biocomposites was studied using scanning electron microscopy (SEM, JSM, 65101v JEOL, Japan). The samples were dispersed uniformly on specimen stubs. Before analyses, all samples were subjected to a thin gold layer sputter coating. Elemental composition and distribution were determined by Energy Dispersive Spectroscopy (EDS) analysis (Bruker, USA). A thermogravimetric analyzer (TGA) was used to analyze thermal stability of the samples (NETZSCH STA 449 F3 Jupiter®-Thermal Analysis System, Germany). For each sample, the heating rate was kept at 10 °C/min from 28 to 800 °C under a nitrogen atmosphere. The thermal behavior of the samples was also evaluated by Differential Scanning Calorimeter (DSC) using a Linseis PT-1600 analyzer, applying a heating rate of 10 °C $min^{-1}$ between 27 and 600 °C under air. Alumina was used as reference material. The balance's detection limit was 0.1 mg while the temperature controller's limit was 0.01◦C. the Surface area, pore size and pore volume were determined by Brunauer-Emmett-Teller analysis (BET) using Quantachrome Touchwin v1.24 surface analyzer from Quantachrome Instruments, USA. The bath temperature was kept at 77.35 K. Degassing was performed at 120 °C for six h.

### 4.2.4 Point of zero charge (PZC)

The PZC values were evaluated through salt addition method. A series of six 250 mL Erlenmeyer conical flasks were prepared. Each flask contained 50 mL of 0.01 M NaCl solution. Initial pH ($pH_i$) values were adjusted to 2, 4, 6, 8, 10 and 12 by dropwise addition of 0.1 M $H_2SO_4$/NaOH solutions. Subsequently, an adsorbent mass of 0.1 g was introduced into every

flask. The suspensions were agitated at 150 rpm for 48 h at 30 °C. The samples were centrifuged, after which the $pH_f$ (final pH) of the supernatant was determined with a digital pH meter (Eutech Instruments, Singapore). Values of PZC were determined from the graph of $pH_i$ v/s ΔpH ($pHi–pH_f$).

### 4.2.5 Batch adsorption studies

The adsorption process of Tr dye on ZnAl LDH and SPI/ZnAl LDH biocomposites was investigated through batch adsorption studies. The effects of pH, initial dye concentration, adsorbent dosage, and contact time were evaluated systematically. Experiments were conducted in test tubes by agitating 5 mg of adsorbent in 10 mL of dye solution (18–38 mg/L) at a speed of 200 rpm under ambient temperature conditions (30°C ± 2). pH was adjusted using 1 M $H_2SO_4$/NaOH solutions. The adsorption process was carried out in dark for predetermined time intervals. After that, adsorbent was separated from the remaining dye solution by centrifugation at 9000 rpm for 10 min and the left-out dye solution was further analyzed using a UV-visible spectrophotometer (JASCO V-750 Spectrophotometer, Japan) at the maximum absorption wavelength ($\lambda_{max}$) of 428 nm. Experiments were performed in triplicate to get the consistent results. Percentage removal efficiency and total amount of dye adsorbed by the absorbent at equilibrium, $q_e$ (mg/g), were calculated by equations (2) and (3).

$$\%\ \text{adsorption} = \frac{C_0 - C_e}{C_o} \times 100 \quad (2)$$

$$\text{Adsorption capacity } (q_e) = \frac{(C_0 - C_e)V}{W} \quad (3)$$

Where $C_0$ and $C_e$ are the initial and equilibrium dye concentrations (mg/L), respectively, V (L) is the volume of dye solution, and W (g) is the weight of adsorbent in grams.

### 4.2.6 Adsorption isotherms

For studying the adsorption behavior of Tr dye onto ZnAl LDH and SPI/ZnAl LDH biocomposites different isotherm models were used for the experimental data whose corresponding linear equations are given below:

Langmuir isotherm model:

$$\frac{C_e}{q_e} = \frac{1}{K_L} qmax + \frac{C_e}{q_{max}} \quad (4)$$

$$R_L = \frac{1}{1 + K_L + C_o} \quad (5)$$

Freundlich isotherm model:

$$log q_e = log kf + \frac{1}{n} log C_e \quad (6)$$

Dubinin Raushkevich (D–R) isotherm model:

$$lnq_e = lnqm - \beta^2 \quad (7)$$

$$E = \frac{1}{\sqrt{2\beta}} \quad (8)$$

Temkin isotherm model:

$$q_e = BlnA + BlnC_e \quad (9)$$

where $C_e$ (mg/L) and $q_e$ (mg/g) are the dye concentration and amount of dye adsorbed at equilibrium, respectively. $q_{max}$ (mg/g) demonstrates the maximum monolayer adsorption capacity. $K_L$ and $K_f$ is Langmuir and Freundlich constants. $R_L$ represents a dimensionless constant indicating the nature of adsorption and whether the process is favorable or unfavorable in the Langmuir isotherm: $R_L$ >1 (unfavorable), $R_L$ =1 (linear), $R_L$ =0 (irreversible), and 0 <RL <1 (favorable). n tells the heterogeneity factor in freundlich isotherm model and values of n range between 0 and 1, where n >1 represents favorable process. β (mol$^{-2}$KJ$^2$/g) represents the D–R activity constant, and ε is the Polanyi potential. E (E KJ/mol) is the mean free adsorption energy. A (L/mg) refers to the Temkin equilibrium binding constant, and B is the constant related to heat of adsorption. Model constants can be calculated by fitting the experimental data using linear equations.

The following thermodynamic formula (Eq. 10) was employed to determine reaction's spontaneity.

$$\Delta G = -\mathrm{RT}\, lnk \quad (10)$$

Where R is the gas constant (8.314 J mol$^{-1}$K$^{-1}$), T corresponds to absolute temperature (298 K), "k" represents the equilibrium constant, and it is feasible to determine the free energy of Tr adsorption on 2:1 SPI/ZnAl LDH biocomposite.

### 4.2.7 Adsorption kinetics study

The reaction rate was analyzed using pseudo-second-order, Elovich linear kinetic, and intraparticle diffusion kinetic models. The linear form of rate equations is as follows:

Pseudo-second-order (PSO) kinetic model:

$$\frac{1}{qt} = \frac{1}{K_2 q_e 2} + \frac{t}{qt} \quad (11)$$

Elovich kinetic model:

$$q_t = \frac{1}{\beta} ln(\alpha\beta) + \frac{1}{\beta} lnt \quad (12)$$

Intraparticle diffusion kinetic (IPD) model:

$$q_t = K_{di}\sqrt{t} + C_i \quad (13)$$

where $q_t$ and $q_e$ are adsorption capacity at time t and equilibrium, respectively. $C_t$ is the concentration of dye at time t (min); $K_2$ (g $mg^{-1}min^{-1}$) is the PSO rate constant; α (mg $g^{-1}$ $min^{-1}$) is the initial rate constant, and β (g $mg^{-1}$) represents the desorption process constant in elovich kinetic model; $K_{di}$ (mg $g^{-1}$ $min^{1/2}$) and $C_i$ (mg $g^{-1}$) are the intraparticle rate constant and resistance to diffusion constant, respectively.

### 4.2.8 Antibacterial activity

The antibacterial properties of ZnAl LDH and 2:1 SPI/ZnAl LDH were investigated using the agar disc diffusion method. This study used precultures of two bacterial strains namely *Listeria* species (gram-positive) and *Acinetobacter calcoaceticus* (gram-negative). These pathogenic bacteria are found in water, stored food, sewage, agricultural and industrial wastes [47,48]. Briefly, both ZnAl LDH and 2:1 SPI/ZnAl LDH were separately dispersed in distilled water at concentrations of 2, 6 and 10 mg/mL. The laminar airflow was irradiated by UV light for 20 min prior to use. Using Whatman filter paper, sterile discs measuring around 6 mm were created. Luria Broth (LB) was used to subculture the bacterial strains for 24 hours at 37 °C. The overnight grown cultures were threefold diluted with sterile standard saline solution. A uniform distribution of approximately 85 µL of each diluted bacterial suspension was applied to Luria-Agar (LA) plates. Subsequently, the discs dipped in ZnAl LDH and 2:1 SPI/ZnAl LDH suspensions were placed on an agar surface; filter paper discs previously dipped in ampicillin (Amp) solution served as a positive control. The plates were incubated at 37 °C overnight. Antibacterial activity was indicated by appearance of inhibitory zones (mm).

### 4.2.9 Practical application of SPI/ZnAl LDH biocomposite

Evaluating the performance of the proposed adsorption technique on real-world samples is essential, as these samples typically exhibit greater complexity and variability compared to laboratory-prepared model solutions. The adsorption percentage of 2:1 SPI/ZnAl LDH biocomposite was assessed using three widely available commercial food products, namely custard powder, yellow candy, and a soft drink (Mountain Dew) alongwith food dye wastewater. The food samples were procured from a local market, while the dye-contaminated wastewater was collected from bakery and sweets shop units located in 22 No. Market, Patiala, India. For the food samples, a custard solution was prepared by dissolving 10 g of custard powder in 100 mL of deionized water, followed by continuous stirring overnight to ensure complete dissolution. The resulting thick solution was then filtered to eliminate any suspended impurities. Yellow candies (14 g) were ground into fine particles and dissolved in 100 mL of deionized water until a uniform yellow-colored solution was obtained. The Mountain Dew soft

drink was used directly without any pretreatment. The adsorption experiments were conducted under conditions consistent with those employed for commercial dye samples to ensure comparability. The concentration of dyes in all solutions was quantitatively measured using a UV-visible spectrophotometer (JASCO V-750, Japan). Each experiment was performed in triplicate to ensure reproducibility and to obtain average values. The percent (%) removal was calculated using the equation (2).

#### 4.2.10 Desorption and regeneration studies of 2:1 SPI/ZnAl LDH biocomposite

To make the adsorption procedure more environment-friendly and economical, adsorbent regeneration is essential. Three desorbing agents 0.1 M NaCl/$H_2SO_4$/NaOH were used for desorption studies. 0.01 g of 2:1 SPI/ZnAl LDH biocomposite was treated with 10 mL dye solution (18 mg/L) for 1 h. The adsorbent was filtered out and dried at 40 °C for 24 h. Now, dye-loaded biocomposite was immersed in desorbing agents and stirred for 5 min at ambient conditions. The final dye concentration was measured spectrophotometrically. The 2:1 SPI/ZnAl LDH biocomposite reusability test was conducted for five consecutive cycles. Desorption efficiency was calculated by following equation.

$$\text{Desorption efficiency (\%)} = \frac{M_{desorbed}}{M_{sorbed}} \times 100 \quad (14)$$

$$= \frac{C_r \times V_r}{C_0 \times C_e} \times 100 \quad (15)$$

## Statistical analysis

All the experiments were performed in triplicates. The data analyses were performed by using one-way analysis of variance (ANOVA) in GraphPad Prism (GraphPad Software, LLC, CA, USA). Mean values comparison was determined by Tukey's test. The differences were considered significant at $p < 0.05$.

## 4.3 Results and discussion

### 4.3.1 Instrumental characterization

#### 4.3.1.1 Crystallographic and morphological studies

XRD patterns obtained for ZnAl LDH and its biocomposites were shown in **Fig. 4.2(a and b)**. The distinctive diffraction peaks of synthesized ZnAl LDH at 2θ = 11.7°, 23.4°, 31.7°, 34.6°, 36.3°, 39.2°, 46.7°, 52.9°, 56.5°, 60.2°, and 61° corresponded to (003), (006), (101), (012), (015), (009), (018), (111), (110), and (113) crystal planes (JCPDS no. 38-0486) [49], confirmed

its highly ordered lamellar structure. Upon incorporation of SPI, systematic changes in the diffraction pattern were observed, providing insight into composite formation rather than simple physical mixing. For biocomposites with lower SPI loadings (0.25:1, 0.5:1, and 1:1) the characteristic LDH reflections were retained with only minor intensity reduction, indicating that the layered structure remained intact while being surrounded by the protein matrix. With increasing SPI content (2:1 and 3:1) a progressive decrease in peak intensity and peak broadening was evident particularly for the basal reflections. This behavior signified partial intercalation and exfoliation of LDH platelets within the SPI matrix caused by strong interfacial interactions that disrupted long-range crystallographic order without destroying the fundamental LDH framework. The emergence of protuberance at $2\theta = 19.2°$ was ascribed to SPI's amorphous β-sheet secondary structure confirming successful incorporation of the protein phase. The simultaneous presence of LDH crystalline reflections and the amorphous SPI signal demonstrated the formation of a hybrid bio–inorganic system [50]. CI values for ZnAL LDH and SPI/ZnAl LDH biocomposites were shown in **Table 4.1**. Significant difference of $p = 0.001$ was showed by the materials. The reduction in overall crystallinity at higher SPI loadings further indicated that hydrogen bonding and electrostatic interactions between SPI functional groups and LDH layers restricted crystal growth and stacking regularity. The observations were consistent with earlier reports on chitosan and polyaniline-based composites [51].

**Table 4.1** Crystallinity Index (CI) values of ZnAl LDH and SPI/ZnAl LDH biocomposites

| Sr No. | Samples | CI (%) |
|---|---|---|
| **1.** | ZnAl LDH | 92.6±0.251 |
| **2.** | 0.2:1 SPI/ZnAl LDH | 85.8±0.264 |
| **3.** | 0.5:1 SPI/ZnAl LDH | 81.7±0.360 |
| **4.** | 1:1 SPI/ZnAl LDH | 67.8±0.251 |
| **5.** | 2:1 SPI/ZnAl LDH | 53.8±0.416 |
| **6.** | 3:1 SPI/ZnAl LDH | 44.4±0.40 |

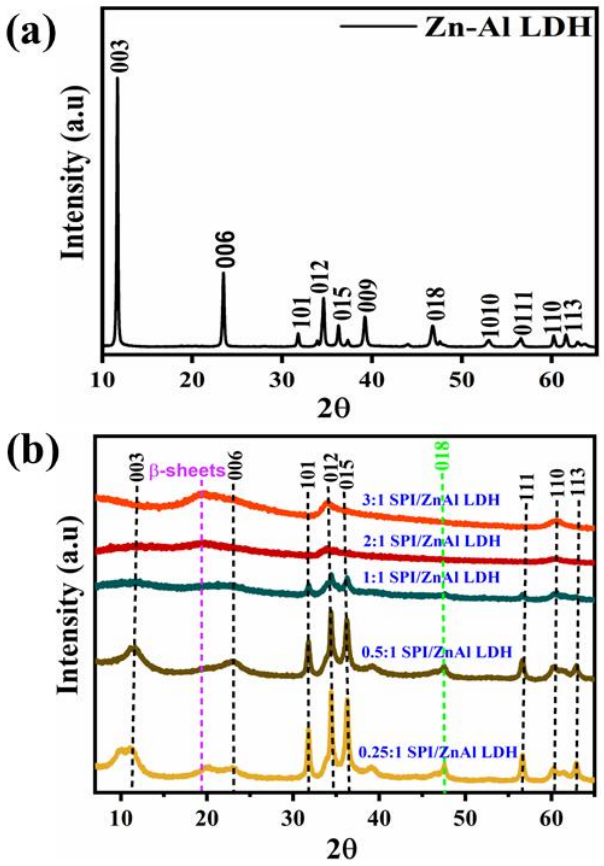


**Fig. 4.2** XRD spectra of **(a)** ZnAl LDH, and **(b)** SPI/ZnAl LDH biocomposites

SEM analysis provides vital insights into the surface morphology and microstructural features of the synthesized biocomposites which directly influence their adsorption performance. As depicted in **Fig. 3a**, ZnAl LDH exhibited an asymmetric and porous morphology characterized by aggregated, irregular-shaped particles with rough surfaces. Such morphological features are indicative of synthesis conditions that favor formation of nanoscale particles with high surface roughness and providing abundant active sites for adsorption processes. The non-symmetrical, porous structure can be attributed to the synthesis methodology, potentially involving co-precipitation techniques. Surface morphology of SPI/ZnAl LDH biocomposites (0.5:1 and 2:1 weight ratios) shifts towards a heterogeneous and denser structure with evident cracks and a rough texture as illustrated in **Fig. 4.3 (b and c)**. Presence of cracks can be considered as micro voids arising from interfacial interactions, stress relaxation, or phase separation during composite formation. The dense morphology with close packing of SPI and LDH particles suggested strong interfacial adhesion possibly due to hydrogen bonding or electrostatic interactions. Some morphological changes were observed in the materials after dye adsorption, as shown in **Fig. 4.3(d–f)**. The surfaces become more compact and smoother with

reduction/disappearance of pores accompanied by the emergence of wrinkled polymeric networks. These changes imply successful dye molecule adherence to the biocomposite surface. Such evolution can be attributed to the physical and chemical interactions like hydrogen bonding, electrostatic attraction or π-π stacking between dye molecules and the functional groups of SPI and LDH which could result in surface coverage and pore blockage [52,53]. The observed morphological transition from porous and rough surfaces to dense, smooth, and wrinkled structures aligns with the mechanism of surface adsorption where dye molecules penetrate or adhere to active sites leading to alterations in surface topology.

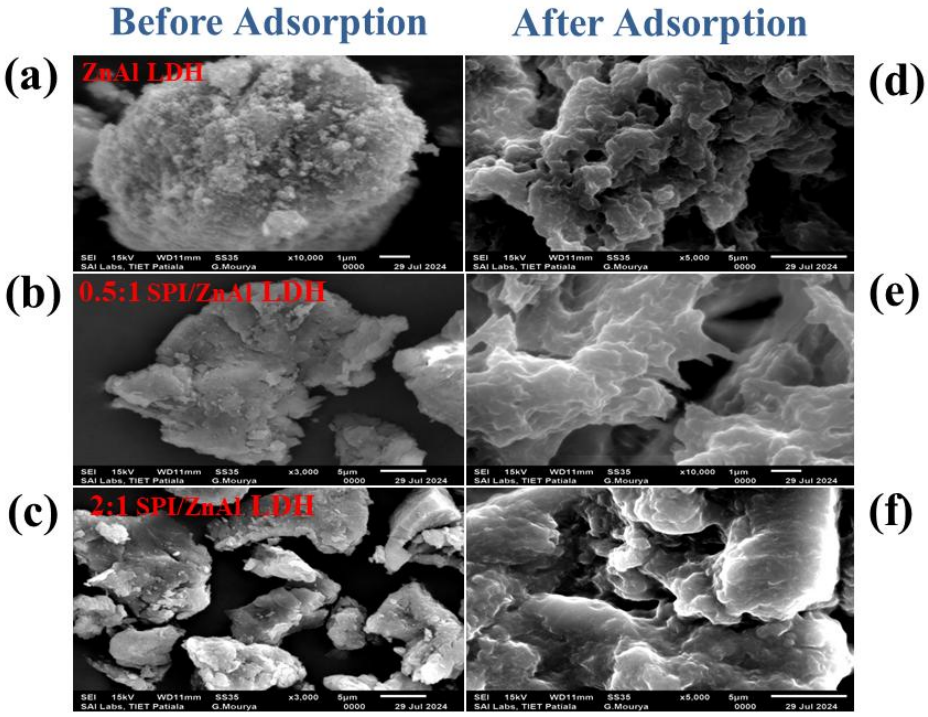


**Fig. 4.3** SEM images of ZnAl LDH, 0.5:1 SPI/ZnAl LDH and 2:1 SPI/ZnAl LDH, **(a–c)** before adsorption, and **(d–f)** after adsorption

To complement the morphological interpretations EDS was performed. The EDS spectra for ZnAl LDH, 0.5:1 and 2:1 SPI/ZnAl LDH biocomposites representing atomic and weight percentage of elements was shown in **Fig. 4.4** and **Table 4.2**. The weight % distribution of zinc (Zn), aluminium (Al), carbon (C), oxygen (O) and nitrogen (N) for ZnAl LDH was 46.38, 4.97, 19.56, 38.02 and 0.90, as shown in **Fig. 4a**. In case of 0.5:1 SPI/ZnAl LDH it was 48.04, 3.30, 18.29, 25.24 and 5.13, while for 2:1 SPI/ZnAl LDH, weight % distribution of Zn, Al, C, O and N was 8.83, 1.59, 40.13, 34.96 and 14.49 as shown in **Fig. 4.4(b and c)**. From the analysis it

was observed that the peaks of principle elements i.e Zn and Al were diminished and dominated by C and N peaks with increase in SPI content.

**Table 4.2** Weight and atomic % of different elements present in ZnAl LDH, 0.5:1 and 2:1 SPI/ZnAl LDH biocomposites

| Elements | Weight % | | | Atomic % | | |
|---|---|---|---|---|---|---|
| | ZnAl LDH | 0.5:1 SPI/ZnAl LDH | 2:1 SPI/ZnAl LDH | ZnAl LDH | 0.5:1 SPI/ZnAl LDH | 2:1 SPI/ZnAl LDH |
| **Zinc (Zn)** | 46.38 | 48.04 | 8.83 | 17.12 | 16.99 | 2.00 |
| **Aluminium (Al)** | 4.97 | 3.30 | 1.59 | 4.44 | 2.83 | 0.87 |
| **Carbon (C)** | 9.74 | 18.29 | 40.13 | 19.56 | 35.23 | 49.46 |
| **Oxygen (O)** | 38.02 | 25.24 | 34.96 | 57.34 | 36.49 | 32.35 |
| **Nitrogen (N)** | 0.90 | 5.13 | 14.49 | 1.54 | 8.46 | 15.32 |
| **Total** | 100 | | | 100 | | |

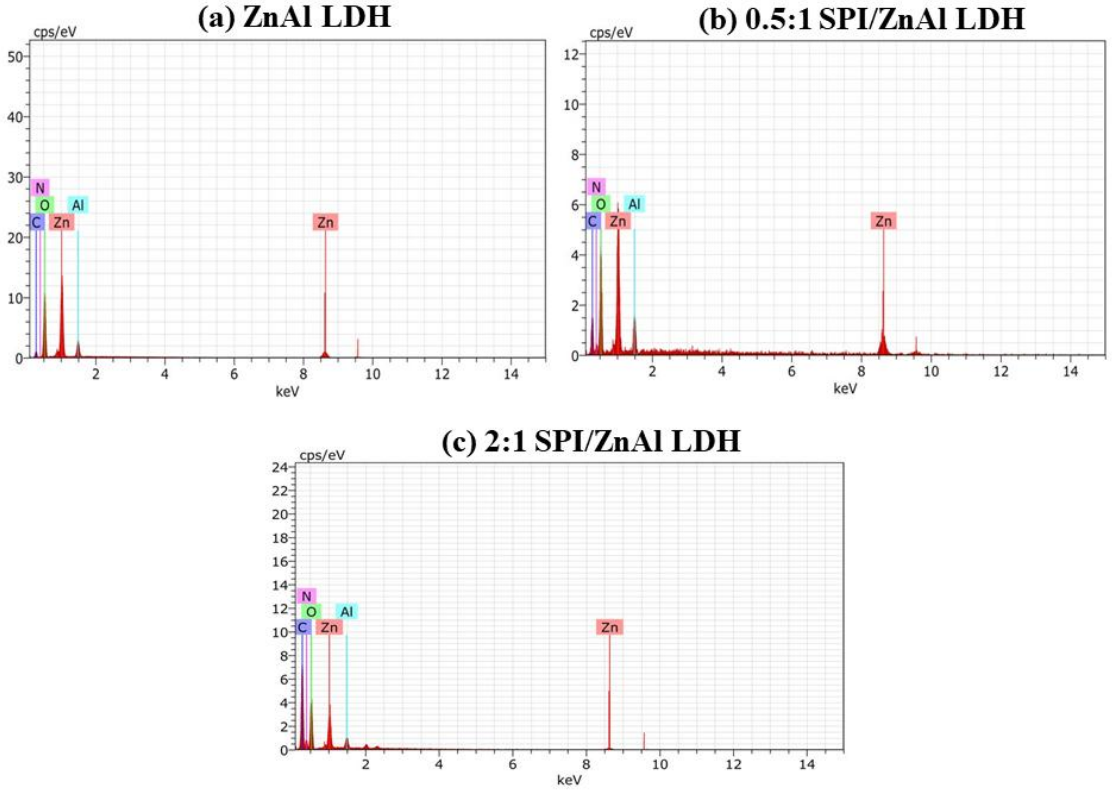


**Fig. 4.4** EDS spectra of **(a)** ZnAl LDH, **(b)** 0.5:1, and **(c)** 2:1 SPI/ZnAl LDH biocomposites

#### 4.3.1.2 Functional group and surface porosity analysis

FTIR spectroscopy provides direct molecular-level evidence of interactions between SPI and ZnAl-LDH. The spectra of ZnAl LDH and SPI/ZnAl LDH biocomposites (0.5:1 and 2:1) was represented in **Fig. 4.5** with the corresponding functional group assignments summarized in **Table 4.3**. Prior to adsorption, ZnAl LDH exhibited various characteristic absorption peaks **(Fig. 4.5a)**. 3412 $cm^{-1}$ corresponded to –OH stretching vibrations, while 1631 $cm^{-1}$ represented the bending vibrations of interlayered water molecules. The adsorption peak at 1356 $cm^{-1}$ was assigned to asymmetric stretching vibrations of interlayered $CO_3^{2-}$ anions probably due to the presence of atmospheric $CO_2$. Lower frequency region (946–446 $cm^{-1}$) corresponded to metal-oxygen bond stretching modes. Appearance of additional characteristic bands of SPI, most notably at 1621 $cm^{-1}$ (amide I, C=O stretching), 1521 $cm^{-1}$ (amide II, N–H bending), and peak at 2976 $cm^{-1}$ were due to asymmetric/symmetric stretching of $–CH_2$ groups indicated the process of biocomposite formation and confirmed the successful incorporation of protein components into biocomposite structures [54]. A broad absorption band that appeared at 3264 $cm^{-1}$ corresponded to the overlapping signals of –OH and –NH groups present in SPI. A peak at 1075 $cm^{-1}$ represented strong C–O stretching of C–O–C groups as shown in **Fig. 4.5(b and c)**. Following Tr adsorption, several changes were observed in the spectra, such as some functional groups shifted to higher/lower frequencies. This shift was indicative of strong hydrogen bonding interactions between the hydroxyl groups of LDH layers and the amino, amide, and carboxyl groups of SPI, whereas certain bands disappeared, suggesting formation of hydrogen bonds between the hydroxyl group of Tr and amino groups of protein component. Weak electrostatic interactions probably contributed to the adsorbent–dye molecule interactions. Additional spectral shifts and the appearance of sulfonate ($SO_3$)-related vibrations at 1250 $cm^{-1}$ confirmed dye adsorption as the same functional groups involved in composite formation also participated in dye binding, clearly suggesting their chemical accessibility and activity. Similar spectral modifications were reported earlier on the removal of congo red dye using bael shell carbon [55].

**Table 4.3** Summary of functional groups assignment before and after adsorption of tartrazine dye on ZnAl LDH, 0.5:1 and 2:1 SPI/ZnAl biocomposites

| Wavenumber ($cm^{-1}$) | Functional groups |
|---|---|
| **3420 $cm^{-1}$** | −OH stretching |
| **2976$cm^{-1}$** | $-CH_2$ stretching of aliphatic groups |
| **1631 $cm^{-1}$** | bending vibrations of the interlayered water molecules |
| **1626 $cm^{-1}$** | amide I C=O stretching |
| **1521 $cm^{-1}$** | amide II N−H bending |
| **1356 $cm^{-1}$** | asymmetric stretching vibrations of the interlayered $CO_3^{-2}$ anions |
| **1250 $cm^{-1}$** | $-SO_3$ stretching |
| **1075 $cm^{-1}$** | strong C–O stretching of C–O–C groups |
| **1057 $cm^{-1}$** | strong C–O stretching |
| **946–446 $cm^{-1}$** | stretching of metal–oxygen bond |

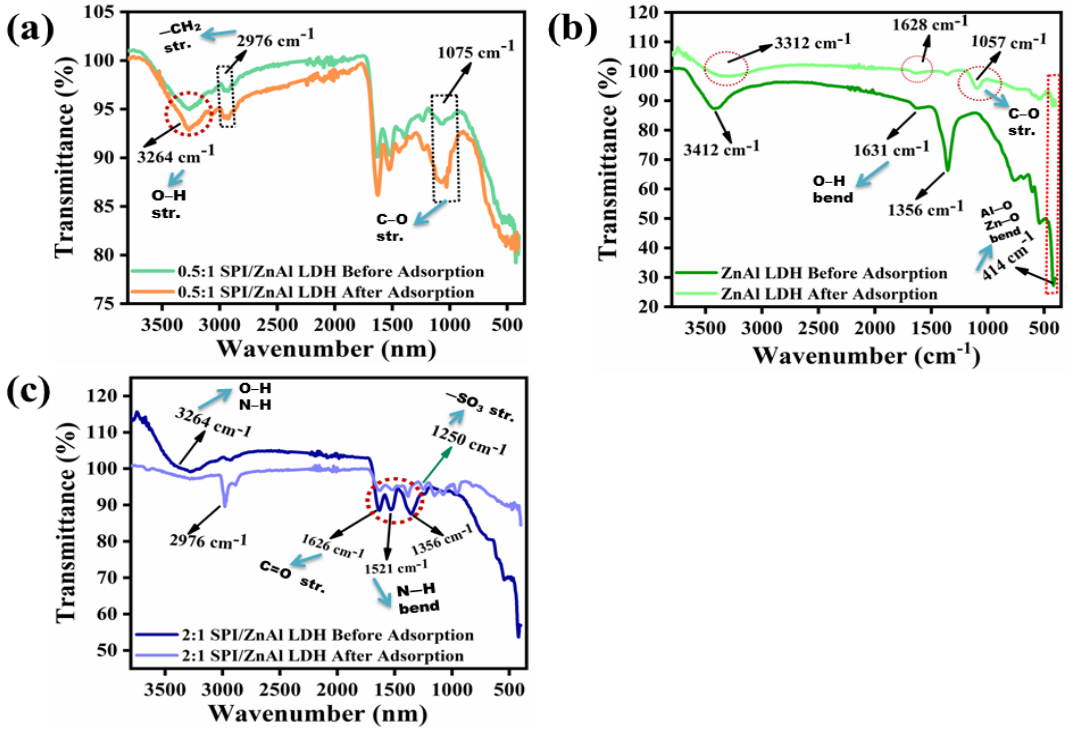


**Fig. 4.5** FTIR spectra of **(a)** ZnAl LDH, **(b)** 0.5:1 SPI/ZnAl LDH, and **(c)** 2:1 SPI/ZnAl LDH biocomposites before and after adsorption

Nitrogen adsorption-desorption measurements at 77.35 K serve as a fundamental approach for characterizing the textural properties of porous materials, facilitating the quantitative determination of specific surface area, pore size distribution, and pore volume. A Type–IV Langmuir adsorption/desorption profile with distinctive H3 hysteresis loops by the nitrogen sorption isotherm of ZnAl LDH and 2:1 SPI/ZnAl LDH biocomposite suggested multilayer and mesoporous properties. The distinct H3 hysteresis suggested non-rigid, aggregated sheet-like particles forming slit-like pores [56]. The material's mesoporous nature (1–20 nm) was confirmed by pore size distribution analysis. The initial rapid increase in adsorption volume with increasing relative pressure during adsorption denotes multilayer formation and pore filling phenomena, while the hysteresis observed in the desorption branch suggested capillary condensation within mesoporous structures. Specific surface area and pore volume for ZnAl LDH was dropped from 31.96 $m^2/g$ to 1.7939 $m^2/g$ and 0.109 $cm^3/g$ to 0.058 $cm^3/g$ after incorporating SPI content, as shown in **Fig. 4.6(a and b)**. This significant decline indicated substantial occupation of pore spaces by the larger molecular size SPI which obstructs nitrogen access to internal surfaces. The pore filling effect was consistent with molecular size exclusion principles and surface blocking phenomena observed in organic-inorganic hybrid materials. Decrease in porosity and surface area with higher SPI loading suggested that the organic molecules not only fill interlayer spaces but also induces structural densification subsequently diminishing accessible surface sites for nitrogen adsorption. Despite this substantial reduction the lower BET surface area did not imply decreased adsorption performance. In aqueous dye adsorption systems, particularly for ionic dyes such as tartrazine, adsorption was often governed by electrostatic attraction, hydrogen bonding, and ion-exchange mechanisms, rather than by surface area alone. The SPI matrix introduced abundant functional groups ($–NH_2$, –COOH, –OH) that act as active binding sites which enhance dye–adsorbent interactions even when the physical surface area was reduced. Moreover, LDHs inherently possessed anion-exchange capabilities allowing dye molecules to interact with interlayer regions that could not be fully probed by nitrogen adsorption. These results were consistent with earlier reports on organically modified bentonite-based composites that were used to remove Tr from aqueous solutions [57,58].

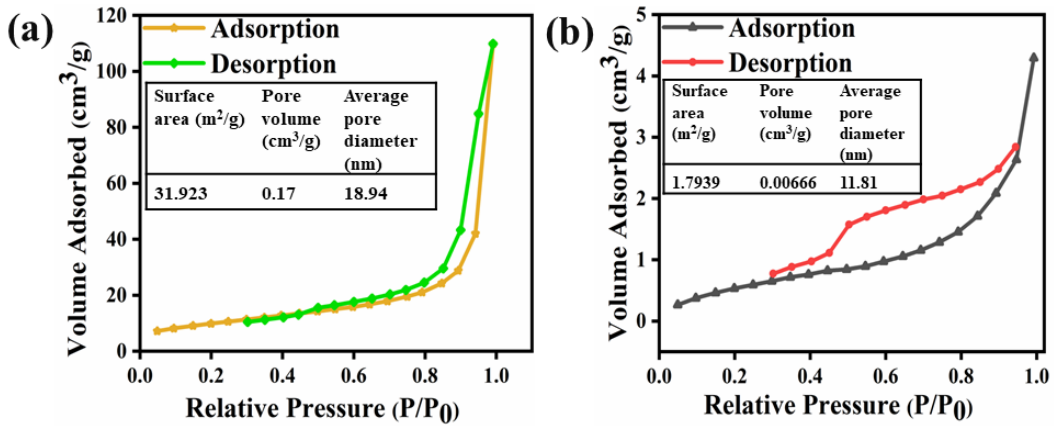


**Fig. 4.6** BET analysis **(a)** ZnAl LDH and **(b)** 2:1 SPI/ZnAl LDH biocomposites

#### 4.3.1.3 Thermal properties

The thermal behavior and stability of ZnAl LDH and SPI/ZnAl LDH biocomposites were evaluated by combining thermogravimetric analysis (TGA) and differential scanning calorimetry (DSC), as both techniques provided complementary information on mass loss events and associated thermal transitions. The data was presented in Fig. 7(a,b). Initial thermal event observed below ~200°C were referred to the loss of physically adsorbed and interlayer water molecules, as evident by both gradual mass loss in TGA and an endothermic peak in the DSC thermograms. This transition reflected the hydrophilic nature of LDH layers and the presence of bound water within the SPI matrix [59]. The major degradation region between ~200 and 450°C represented the most critical stability domain of the biocomposites (0.5:1 and 2:1). In this temperature range, TGA showed significant weight loss arising from overlapping processes including dehydroxylation of LDH layers, release of interlayer carbonate species, and thermal degradation of SPI polypeptide chains. Findings were consistent with the TGA data obtained for Starch-NiFe-layered double hydroxide composites [60]. Correspondingly, DSC displayed broad endothermic transitions associated with protein denaturation, peptide bond cleavage, and structural rearrangements within the biocomposites. The broadening and shift of these transitions in SPI/ZnAl LDH compared to pristine LDH indicated strong interfacial interactions between SPI functional groups and LDH layers which retarded thermal decomposition. At higher temperatures (>450°C), only minor weight changes were observed in TGA accompanied by weak endothermic signals in DSC attributable to the conversion of the LDH framework into stable mixed metal oxides (ZnO and $Al_2O_3$) and carbonization of the protein residue [61]. Notably, the higher residual mass of the biocomposite at elevated temperatures confirmed the stabilizing role of the inorganic LDH component. The combined

TGA–DSC analysis demonstrated that incorporation of SPI into ZnAl LDH led to thermally stable hybrid structures where the LDH layers acted as a protective barrier, delaying protein degradation and improving resistance to thermal decomposition. These results confirmed the structural integrity and suitability of the SPI/ZnAl LDH biocomposite for practical applications involving thermal or acidic environments.

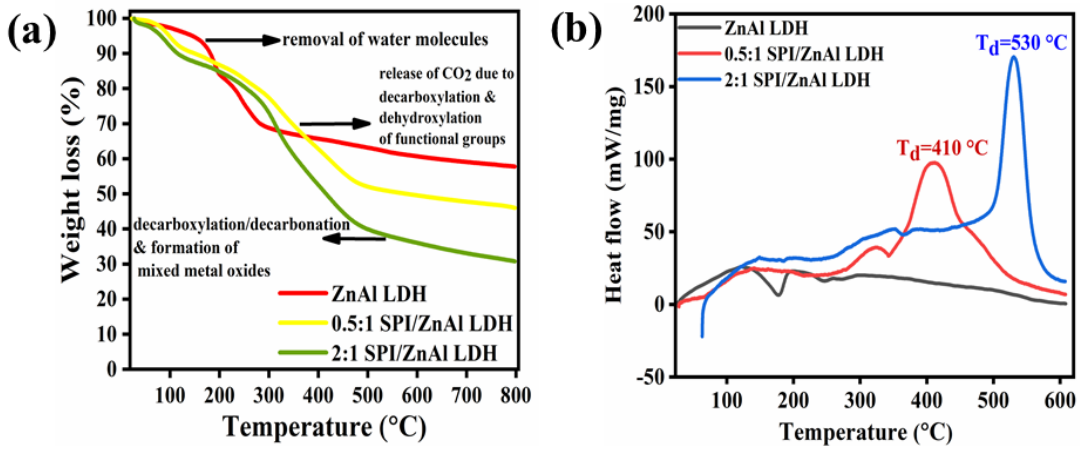


**Fig. 4.7 (a)** TGA curves, and **(b)** DSC analyses of ZnAl LDH, 0.5:1 and 2:1 SPI/ZnAl LDH biocomposites

### 4.3.1.4. Adsorption parameters optimization

#### 4.3.1.4.1 Effect of initial dye concentration

Initial dye concentration on the adsorption process was investigated over the range of 18–38 mg/L at ambient temperature (30°C ± 2°C), while keeping all other parameters, such as pH (2), contact time (60 min), and adsorbent dosage (5 mg) constant. The results illustrated in **Fig. 4.8a** demonstrated that adsorption percentage decreases with the increase in initial dye concentration. This finding contrasts with the commonly reported trend in adsorption studies where increased solute concentration typically enhances adsorption capacity due to a stronger driving force for mass transfer [62]. The decline at higher dye concentrations suggested that at lower concentrations the adsorbent surface possesses an excess of available active sites in relation to the number of dye molecules facilitating efficient adsorption. Under such conditions, adsorption is likely dominated by monolayer formation and favorable interactions between the dye and adsorbent surface. The high site availability enables better utilization of the adsorbent resulting in greater removal efficiency and capacity. As the dye concentration rises, number of dye molecules exceeds the number of accessible binding sites resulting in saturation of active sites. The limited number of active sites restricts the adsorption capacity and competition

among dye molecules for these sites reduces the overall percentage of dye removal. The reduced concentration gradient between the bulk solution and the adsorbent surface at higher dye concentrations can slow down the adsorption rate. The optimal dosage was 5 mg.

#### 4.3.1.4.2 Effect of initial pH

Solution pH often called the 'master variable' critically affects the adsorption process by governing adsorbent's surface charge, ionization state, and functional group dissociation. In this study, the adsorption of Tr dye was tested across a pH range from 2 to 12 (in increments of 2 units) with constant initial dye concentration (18 mg/L), adsorbent dosage (5 mg), and contact time (60 min) at 30 ± 2°C. Results shown in **Fig. 4.8b** revealed declined adsorption percentage with increasing pH. The 2:1 biocomposite showed early complete removal (99.85%) at pH 2. ZnAl LDH exhibited a significantly lower removal efficiency of 47.9%, likely due to partial hydrolysis or instability in strongly acidic conditions [63].

At pH 2, the surface of biocomposite becomes positively charged due to the protonation of hydroxyl and amino groups. As Tr dye exists as anionic ions under acidic conditions (pKa values $–SO_3^-$, = 2.0, –COO− = 5.0, –N=N– = 10.86) it carried a strong negative charge from their sulfonate groups. These opposite charge interactions led to strong electrostatic attraction between the adsorbent and the dye resulting in enhanced adsorption under acidic conditions. As the solution pH rises, electrostatic repulsions and competition from $OH^-$ ions reduce dye uptake. Complete ionization of carboxylic groups within SPI matrix altered the equilibrium.

The PZC values for ZnAl LDH, 0.5:1, and 2:1 SPI/ZnAl LDH biocomposites were 6.10, 6.45, and 6.72 **(Fig. 4.9)**. Below PZC, surface of adsorbents are positively charged enhancing dye uptake whereas above PZC, negative surface charge lowers the sorption capacity. The optimal removal was achieved at pH 2. This explanation was also supported by FTIR analysis. The color variations of Tr dye solutions after treatment were shown in **Fig. 4.10**.

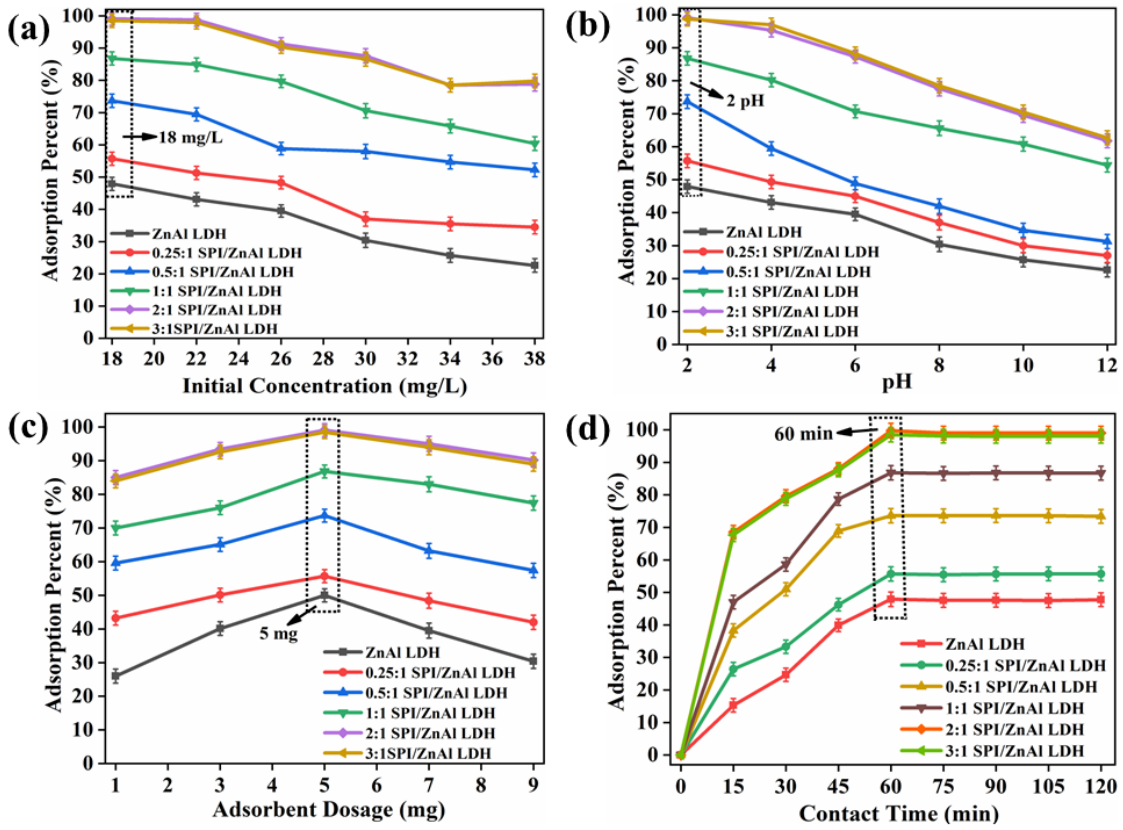


**Fig. 4.8** Parametric optimization for tartrazine dye adsorption by ZnAl LDH and SPI/ZnAl LDH biocomposites **(a)** Effect of initial dye concentration, **(b)** Effect of pH, **(c)** Effect of adsorbent dosage, and **(d)** Effect of contact time

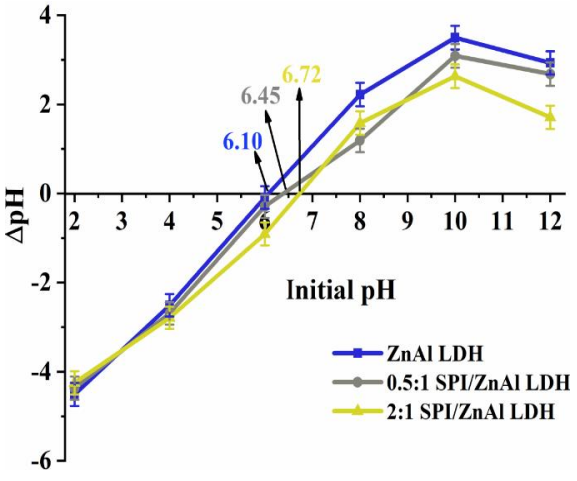


**Fig. 4.9** Point of zero charge (PZC) of ZnAl LDH, 0.5:1 and 2:1 SPI/ZnAl LDH biocomposites

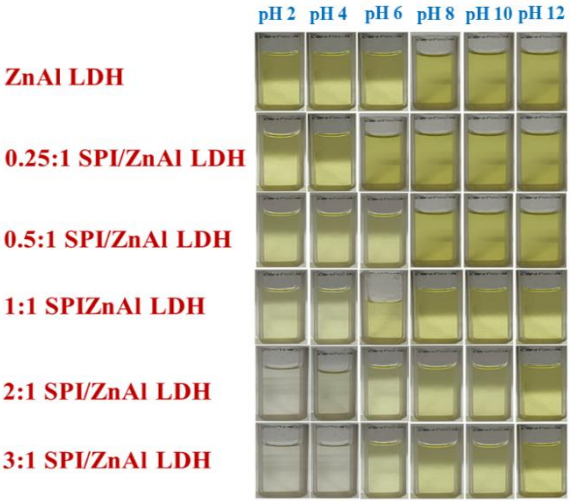


**Fig. 4.10** Variation in color of tartrazine at different pH ranges. Experimental Conditions: Temperature = 30±2°C, Initial Concentration = 18 mg/L, Contact Time = 60 min, Adsorbent Dosage = 5 mg

#### 4.3.1.4.3 Effect of adsorbent dosage

The amount of adsorbent used play a critical role in determining the adsorption capacity as each adsorbent has a finite number of active sites available for binding the adsorbate molecules. To determine the optimal adsorbent requirement for maximum Tr adsorption, experiments were run over a range of 1–9 mg. Initial dye concentration (18 mg/L), pH (2.0), and contact time (60 min) were kept constant at ambient temperature. Results indicated that by increasing the adsorbent dosage from 1 mg to 5 mg adsorption percentage enhanced significantly. This could be attributed to increased availability of active sites and a larger effective surface area for adsorption allowing more dye molecules to be captured. The adsorption percentage of Tr dye was found to be 28 % to 45% for ZnAl LDH and from 43% to 99.85% across 0.25:1 to 3:1 SPI/ZnAl LDH biocomposites, with 2:1 achieving the highest adsorption, as shown in **Fig. 4.8c**. However, when the adsorbent dosage exceeded 5 mg, a decrease in adsorption percentage was observed. This decline was likely caused by the aggregation of adsorbent particles at higher dosages which reduced the total accessible surface area and blocked the active adsorption sites. Aggregation can also hinder effective dispersion of adsorbent in solution leading to decreased interactions between dye molecules and active sites [64]. An optimal dosage of 5 mg was selected for experiments to balance site availability and minimize particle agglomeration

#### 4.3.1.4.4 Effect of contact time

Contact time is a critical factor affecting the adsorption process as it directly influences the rate at which adsorbate molecules are transferred from the bulk solution to the adsorbent surface and subsequently bound to active sites. The impact of contact time on removal of Tr dye was studied from 15–120 min keeping initial dye concentration (18 mg/L), pH (2) and adsorbent dosage (5 mg) constant under ambient conditions. The adsorption profile **(Fig. 4.8d)** revealed a rapid uptake of dye molecules during the initial 60 min followed by a gradual approach to equilibrium. High adsorption rate observed at the beginning of the process could be attributed to abundance of vacant adsorption sites on adsorbent surface and strong affinity between the Tr dye molecules and functional groups present on the adsorbent. This leads to efficient surface binding through electrostatic attraction, hydrogen bonding and π–π interactions. As the process continued, number of available active sites diminished and the surface become increasingly occupied by adsorbed dye molecules [65]. Consequently, repulsive forces develop between the already adsorbed dye molecules and those remaining in the solution, this led to deceleration of the adsorption rate.

After 60 min, the system reached equilibrium which was evidenced by the plateau in dye removal percentage where no further significant adsorption occurred. This indicated that the adsorbent surface has become saturated and the dynamic exchange of dye molecules between solution and adsorbent surface reached at balance. The overall rate of adsorption was often controlled by diffusion of dye molecules from the bulk solution through the boundary layer to the adsorbent surface. This was a process referred to as external mass transfer which could be a rate-limiting step depending on the adsorbent's pore structure and surface chemistry [66]. The UV-visible spectra under constant experimental conditions were shown in **Fig. 4.11**. The adsorption performance of SPI alone (control) was evaluated under same experimental conditions. The UV-visible spectrum was shown in **Fig. 4.12**.

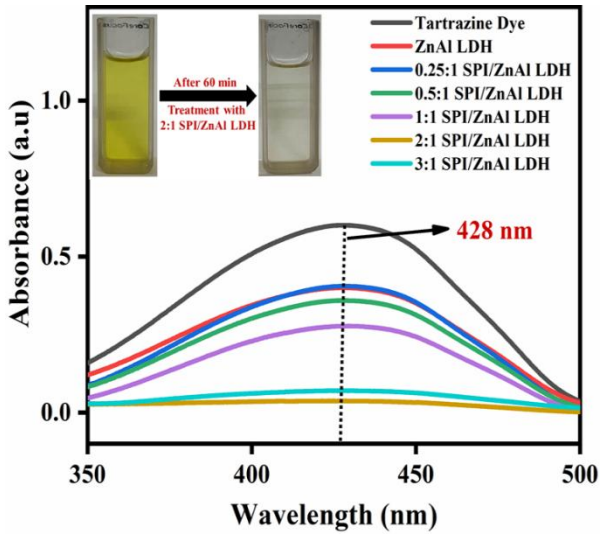


**Fig. 4.11** Uv-vis adsorption spectra of tartrazine dye on ZnAl LDH and SPI

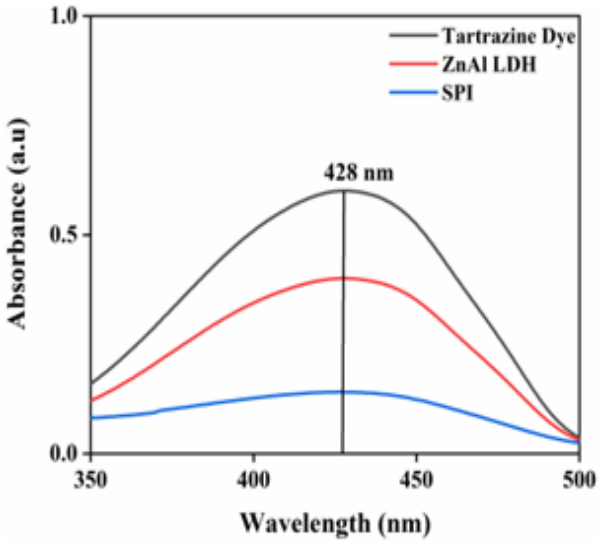


**Fig. 4.12** Uv-vis adsorption spectra of tartrazine dye on SPI

### 4.3.2 Adsorption isotherms

The interactions between dye molecules and synthesized adsorbent surfaces at equilibrium were elucidated by employing different adsorption isotherm models to analyze the experimental results of ZnAl LDH, 0.5:1 SPI/ZnAl LDH, and 2:1 SPI/ZnAl LDH. Linear plots of isotherm models were shown in **Fig. 4.13**, whereas **Tables 4.4** and **4.5** provided the correlation values and adsorption isotherm constants. There was a significant difference ($p$ = 0.001). Using the Langmuir isotherm model, according to which the monolayer adsorption occurs when only one dye molecule interacts with each active site, where full site occupancy was represented by saturation coverage. $R^2$ values for ZnAl LDH, 0.5:1 SPI/ZnAl LDH, and 2:1 SPI/ZnAl LDH were 0.9658, 0.9927, and 0.9935 **(Fig. 4.13a)**. Corresponding maximum

adsorption capacities ($q_{max}$) for each of these adsorbents were found to be 26.44 mg/g, 46.83 mg/g, and 49.01 mg/g, respectively. The increase in adsorption capacity with higher SPI content could be attributed to the generation of additional active sites and enhanced surface characteristics such as increased porosity and hydrophilicity [46]. Freundlich isotherm model describes adsorption on heterogeneous surfaces with the potential for multilayer development. This model yielded high correlation coefficients ($R^2$) of 0.9745, 0.9962, and 0.9959 for ZnAl LDH, 0.5:1 SPI/ZnAl LDH, and 2:1 SPI/ZnAl LDH **(Fig. 4.13b)**. n and $R_L$ values were less than 1 validating favorable and homogenous adsorption during eliminating process. The convergence of these parameters supported that adsorbents exhibited homogenous adsorption sites with a high degree of affinity for the Tr dye molecules despite the model's accommodation for heterogeneous and multilayer adsorption. This indicated that while the adsorbent surface might have some degree of heterogeneity the adsorption process remained efficient and well-fitted by both Langmuir and Freundlich isotherms. The Gibbs free energy change (ΔG) for the adsorption of Tr dye onto the 2:1 biocomposite was calculated (–2.72 kJ $mol^{-1}$). Since ΔG is negative, this confirmed that the adsorption process occurred spontaneously under the studied conditions. The magnitude of ΔG in this range also suggested that the adsorption mechanism likely involves physisorption or weak chemisorption interactions which are typically associated with moderate energy changes.

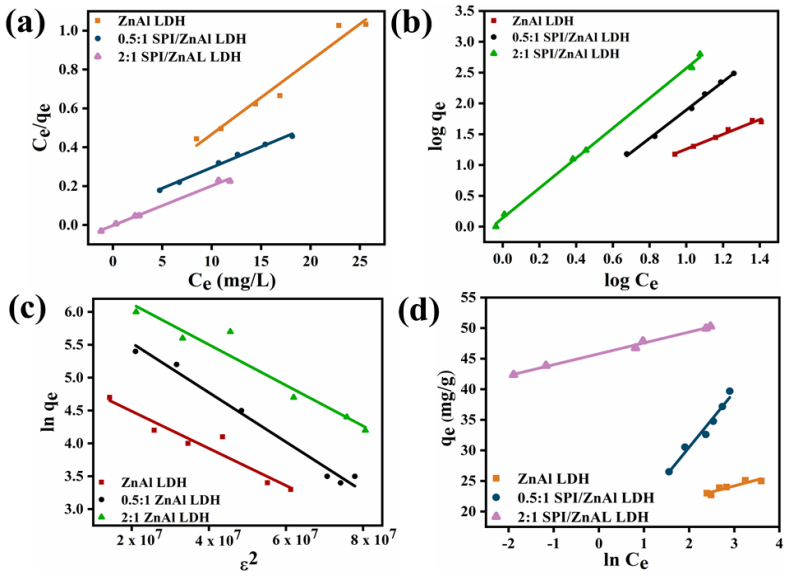


**Fig. 4.13** Linearlized fitting of **(a)** Langmuir, **(b)** Freundlich, **(c)** Dubinin Raushkevich D–R, and **(d)** Temkin adsorption isotherm models for tartrazine dye onto ZnAl LDH, 0.5:1 SPI/ZnAl LDH, and 2:1 SPI/ZnAl LDH biocomposites

**Table 4.4** Calculated parameters of Langmuir and Freundlich isotherm models for tartrazine dye adsorption onto ZnAl LDH, 0.5:1 SPI/ZnAl LDH and 2:1 SPI/ZnAl LDH based biocomposites

| | | **Langmuir isotherm model** | | | **Freundlich isotherm model** | | |
|---|---|---|---|---|---|---|---|
| **Samples** | **$q_{max}$ (mg/g)** | **$K_L$** | **$R_L$** | **$R^2$** | **$K_F$** | **n** | **$R^2$** |
| ZnAl LDH | 26.44 | 2.2 | 0.023 | 0.9658 | 3.37 | 0.79 | 0.9745 |
| 0.5:1 SPI/ZnAl LDH | 46.83 | 4.2 | 0.012 | 0.9927 | 5.12 | 0.85 | 0.9962 |
| 2:1 SPI/ZnAl LDH | 49.01 | 3 | 0.052 | 0.9935 | 3.84 | 0.91 | 0.9959 |

**Table 4.5** Calculated parameters of Dubinin Raushkevich (D–R) and Temkin isotherm models for tartrazine dye adsorption onto ZnAl LDH, 0.5:1 SPI/ZnAl LDH and 2:1 SPI/ZnAl LDH based biocomposites

| | **D–R isotherm model** | | | **Temkin isotherm model** | | |
|---|---|---|---|---|---|---|
| **Samples** | **$\beta \times 10^{-8}$ ($mol^{-2}KJ^2/g$)** | **E (KJ/mol)** | **$R^2$** | **B ($KJ\ mol^{-1}$)** | **A ($L\ mg^{-1}$)** | **$R^2$** |
| ZnAl LDH | 3.8 | 3.59 | 0.9200 | 0.0019 | 11,133 | 0.8571 |
| 0.5:1 SPI/ZnAl LDH | 2.91 | 4.15 | 0.9837 | 0.0090 | 3.925 | 0.9658 |
| 2:1 SPI/ZnAl LDH | 2.85 | 4.19 | 0.9395 | 0.00177 | $1.5 \times 10^{11}$ | 0.9723 |

D-R isotherm model sheds light on the adsorption process using linear plots of ln $q_e$ vs ε **(Fig. 4.13c)**. A critical parameter derived from the D-R model is the mean free energy of adsorption (E kJ/mol) which provides insight into the nature of the adsorption process. It distinguishes between physical adsorption, ion exchange, or chemical adsorption [67]. The calculated E values for ZnAl LDH, 0.5:1 SPI/ZnAl LDH and 2:1 SPI/ZnAl LDH were 3.59 KJ/mol, 4.15 KJ/mol, and 4.19 KJ/mol, respectively. Since the values were less than 8 KJ/mol, it suggested that the adsorption of Tr dye primarily occurs via physisorption, which involves weak van der Waals forces rather than chemical bonding.

Complementary information was obtained from the Temkin isotherm model which accounts for adsorbate-adsorbent interactions by assuming that the heat of adsorption decreases linearly with increasing surface coverage due to adsorbate-adsorbate repulsion effects. Linear plots of

qt vs $\sqrt{t}$ were shown in **Fig. 4.13d**. The heat of adsorption (B) values for ZnAl LDH, 0.5:1 SPI/ZnAl LDH, and 2:1 SPI/ZnAl LDH were 0.0019 KJ/mol, 0.0090 KJ/mol, and 0.00177 KJ/mol, respectively. The positive values of B indicated endothermic process implying that adsorption capacity increases with temperature. The relatively low magnitude of these B values signifies that physisorption dominated, as weak physical interactions typically correspond to small heats of adsorption. According to the findings, Langmuir and Freundlich isotherm models best reflect the fit. Such fitting arose from the hybrid nature of the SPI/ZnAl LDH biocomposite that contained both relatively uniform adsorption sites associated with LDH layers and heterogeneous functional sites originating from the SPI matrix. The good fit to the Langmuir model suggested presence of energetically favorable sites where adsorption occurred in a near-monolayer fashion consistent with electrostatic interactions and anion exchange at positively charged LDH surfaces. In contrast, the Freundlich model accounted for surface heterogeneity and multilayer adsorption, considering the diverse functional groups (–$NH_2$, –COOH, –OH) present in SPI and the non-uniform distribution of active sites within the composite as well. Although both models adequately described the experimental data but Freundlich model more realistically represented the overall adsorption mechanism. Comparison of adsorption efficiency of different composites for Tr dye was listed in **Table 4.6**.

**Table 4.6** Comparison of adsorption capacities for tartrazine dye with other materials

| **Adsorbent** | **Adsorbate Initial Concentration (mg/L)** | **Adsorbent amount (mg)** | **pH** | **Maximum adsorption percentage** | **$q_{max}$ (mg/g)** | **Reference** |
|---|---|---|---|---|---|---|
| Sawdust | – | 5000 | 3 | 97% | 4.71 | [68] |
| Bottom ash | 46 | 100 | 2 | 86.85% | 12.6 | [69] |
| Polyaniline nanolayer composite | 50 | 500 | 2–5 | 98% | 2.47 | [70] |
| Polypyrrole coated tenorite nanoparticle | 50 | 1000 | – | 87% | 42.50 | [71] |
| S/MgAl LDH | – | 6 | 7 | 97.6% | 162.9 | [72] |
| $Zn_2$Al/Cl LDH | 40 | 40 | 5.8 | 96.8% | 282.48 | [73] |
| **2:1 SPI/ZnAl LDH** | **18** | **5** | **2** | **99.85%** | **49.01** | **This work** |

### 4.3.3 Adsorption kinetics

Kinetic analysis offers important information about the mechanism and rate of adsorption process. In this study, adsorption kinetics was investigated by monitoring the dye uptake over a contact time range of 15 to 120 min at ambient temperature (30°C ± 2°C). The adsorption profile exhibited a rapid uptake phase within the initial 60 min followed by a slower approach to equilibrium. Three kinetic models were applied to elucidate the adsorption mechanism. **Table 4.7** summarized the kinetic rate constants and correlation coefficients ($R^2$) for ZnAl LDH, 0.5:1 SPI/ZnAl LDH, and 2:1 SPI/ZnAl LDH with corresponding linear graphs as shown in **Fig. 4.14**, providing visual confirmation of model fitting. There was a significant difference ($p = 0.001$).

PSO kinetic model demonstrated better agreement with the experimental adsorption data as evidenced by correlation coefficients ($R^2$) which approached to unity **(Fig. 4.14a)**. A noteworthy trend in the PSO rate constant ($K_2$) at higher SPI concentrations indicated increased electrostatic interactions between Tr molecules and the adsorbent surface. The experimentally determined equilibrium adsorption capacities ($q_{eexp}$) for ZnAl LDH, 0.5:1 SPI/ZnAl LDH, and 2:1 SPI/ZnAl LDH were 0.5899 mg/g, 0.8881 mg/g, and 1.1974 mg/g, which closely corresponded to the values calculated from the model ($q_{ecal}$) of 0.6265 mg/g, 0.9573 mg/g, and 1.2430 mg/g, respectively. This close agreement validated the applicability of PSO model in describing the adsorption kinetics. Adsorption process involves a combination of external mass transfer and intraparticle diffusion mechanisms with chemisorption acting as the rate-limiting step [74]. Such insights are critical for optimizing the adsorption system for practical wastewater treatment applications.

The Elovich kinetic model was employed to characterize the adsorption behavior particularly focusing on heterogeneous adsorbent surfaces and chemisorption kinetics. Plots of $q_t$ vs ln t were utilized for Elovich model determination **(Fig. 4.14b)**. The initial adsorption rate constant α (mg $g^{-1}$ $min^{-1}$) and desorption constant β (g $mg^{-1}$) represented extent of surface coverage and activation energy barriers. This model was based on assumption that adsorption rate decreases exponentially with increasing surface coverage due to the heterogeneous nature of active sites. The correlation coefficients ($R^2$ = 0.9782–0.9910) supported activated chemical adsorption with minimal product desorption. 2:1 biocomposite provided highest α value (1.2806 mg $g^{-1}$ $min^{-1}$), suggesting higher affinity for Tr dye molecules. The optimal proportion of SPI and ZnAl LDH in biocomposite structure could be responsible for increased adsorption tendency. IPD model was used to investigate that the adsorption process was controlled by diffusion of

dye molecules into the porous structure of the adsorbent. Linear plots of $q_t$ vs $\sqrt{t}$ were shown in **Fig. 4.14c**. The lower $R^2$ values (0.9011–0.9430) indicated that IPD was not the sole rate-limited step for dye removal. This result suggested that surface-based interactions could be more important in regulating the total adsorption kinetics than interior diffusion.

**Table 4.7** Calculated parameters of Pseudo Second Order, Elovich adsorption kinetic models and Intraparticle diffusion model for tartrazine dye adsorption onto ZnAl LDH, 0.5:1 SPI/ZnAl LDH and 2:1 SPI/ZnAl LDH based biocomposites

| | **Pseudo Second Order** | | | | **Elovich kinetic model** | | | **Intra particle diffusion** | |
|---|---|---|---|---|---|---|---|---|---|
| **Samples** | **$q_{eexp}$ (mg/g)** | **$q_{ecal}$ (mg/g)** | **$K_2$ (g mg$^{-1}$min$^{-1}$)** | **$R^2$** | **β (g mg$^{-1}$)** | **α (mg g$^{-1}$ min$^{-1}$)** | **$R^2$** | **$K_{id}$ (mg g$^{-1}$ min$^{1/2}$** | **$R^2$** |
| **ZnAl LDH** | 0.5899 | 0.6265 | 0.119 | 0.9813 | 0.0214 | 0.0668 | 0.9802 | 0.06233 | 0.9430 |
| **0.5:1 SPI/ZnAl LDH** | 0.8881 | 0.9573 | 0.145 | 0.9845 | 0.0632 | 0.2414 | 0.9910 | 0.06123 | 0.9011 |
| **2:1 SPI/ZnAl LDH** | 1.1974 | 1.2430 | 0.162 | 0.9951 | 0.1436 | 1.2806 | 0.9782 | 0.07468 | 0.9155 |

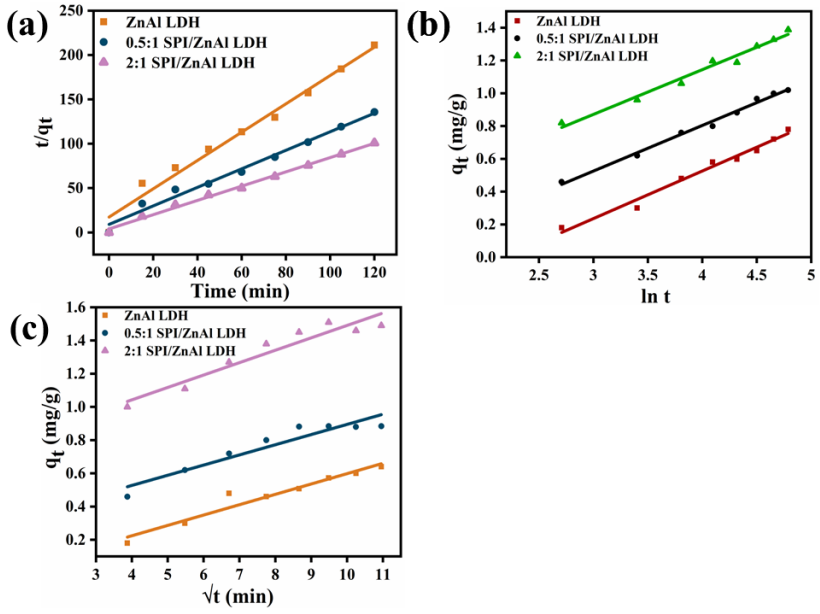


**Fig. 4.14** Linearlized fitting of **(a)** Pseudo Second Order, **(b)** Elovich adsorption kinetic models, and **(c)** Intraparctile diffusion model for tartrazine dye onto ZnAl LDH, 0.5:1 SPI/ZnAl LDH, and 2:1 SPI/ZnAl LDH biocomposites

### 4.3.4 Antibacterial activity

The antibacterial efficacy of ZnAl LDH and 2:1 SPI/ZnAl LDH biocomposite was assessed by agar diffusion method at various concentrations (2, 6, and 10 mg/mL), as presented in **Fig. 15**. At an intermediate concentration of 6 mg/mL, ZnAl LDH exhibited inhibition zones of 7 ± 0.57 mm and 5±0.26 mm against *L.* species and *A. calcoaceticus,* respectively. In contrast, 2:1SPI/ZnAl LDH biocomposite demonstrated enhanced antibacterial activity with 10 ± 0.28 mm and 9 ± 0.47 mm inhibition zones. Increasing the concentration to 10 mg/mL resulted in further increase of inhibition zones to 9 ± 0.12 mm and 10 ± 0.35 mm for ZnAl LDH and significantly larger zones of 12 ± 0.36 mm and 16 ± 0.17 mm for the biocomposite. No inhibition zones were observed at 2 mg/mL for either of the material, indicating a concentration-dependent antibacterial effect. Both the bacterial strains were sensitive to ampicillin which was used as a positive control to validate the antibacterial efficacy. Inherent basicity from –OH groups and the unique characteristics of constituent metal cations provide LDH several advantages over other antibacterial agents. Zn-based LDHs could undergo partial dissolution/ion exchange in aqueous media (and more strongly under slightly acidic environments near bacterial surfaces) releasing $Zn^{2+}$. The $Zn^{2+}$ interfered with membrane proteins and transport systems affecting metal homeostasis due to competition with essential ions, and led to cell death. Surface hydroxyl groups on LDH can catalyze the formation of reactive oxygen species (ROS) such as hydroxyl radicals (•OH) and superoxide ions ($O_2^-$). In the presence of molecular oxygen, the inducing oxidative stress led to disruption of cellular components and DNA of bacterial cells. Consequently, lipid peroxidation and protein oxidation caused membrane rupturing and enzyme inactivation [75,76,77]. For SPI, it was reported that glycinin, one of its main constituents has demonstrated more potent antibacterial action than β-conglycinin against various microbial species [78]. The electrostatic interactions between positively charged amino acid residues of glycinin and negatively charged bacterial cell membranes lead to destabilization of membrane structure which causes eventual cell lysis [79]. Synergistic integration of SPI with ZnAl LDH in the biocomposite likely enhanced the dispersion of active sites and increased the effective surface area available for bacterial contact. This synergy potentially facilitated a more controlled and efficient release of antibacterial $Zn^{2+}$ ions and ROS resulting in a significantly improved antimicrobial effect relative to the individual components. The plausible antibacterial mechanism of SPI/ZnAl LDH-based biocomposites is presented in **Scheme 4.2**.

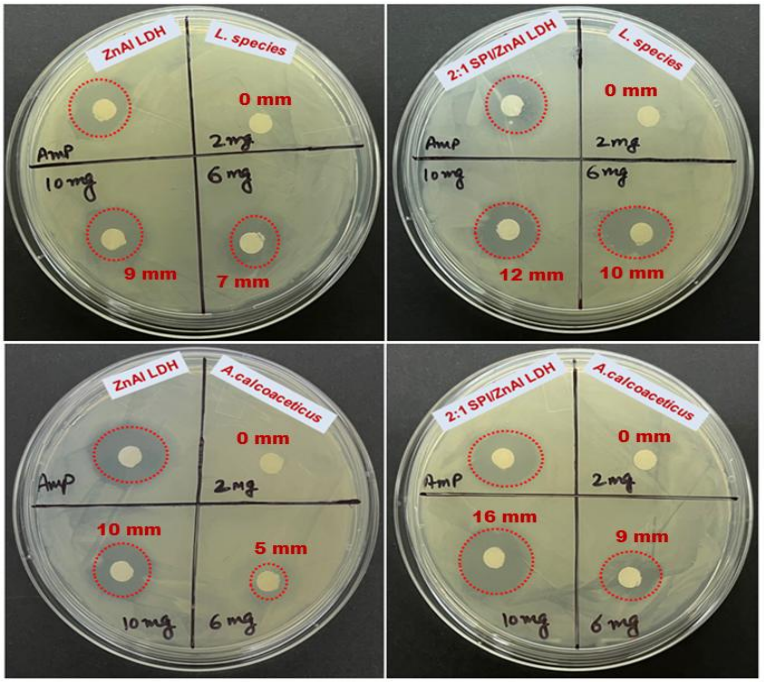


**Fig. 4.15** Antibacterial effect of ZnAl LDH and 2:1 SPI/ZnAl LDH biocomposites against (a) *Listeria* species and (b) *Acinetobacter calcoaceticus* (ampicillin used as a positive control)

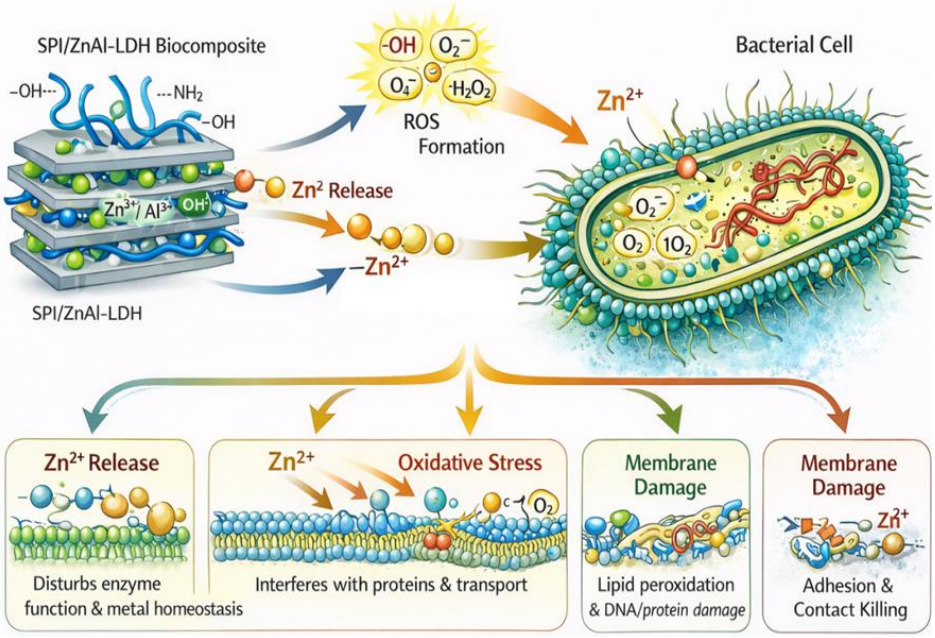


**Scheme 4.2.** Plausible antibacterial mechanism of SPI/ZnAl LDH biocomposites

### 4.3.5 Proposed mechanism for adsorption of tartrazine

Adsorbent–adsorbate interactions in the SPI/Zn-Al LDH biocomposite are governed by a combination of physicochemical forces making the adsorption mechanism inherently complex, as illustrated in **Scheme 4.3**. The functional groups from SPI such as amino (—$NH_2$), carbonyl (C=O), and hydroxyl (—OH) groups played crucial role in forming hydrogen bonds with the dye molecules. The shifts of these groups presented by FTIR spectra after adsorption also provided their involvement in binding. Hydrogen bonding occurred between the hydroxyl and amino groups on the biocomposite surface and the sulfonate and nitro groups of dye, hence, stabilizing the dye molecules on the surface [80]. Partial unfolding of SPI during biocomposite synthesis facilitated the accessibility of these functional groups, enhancing the density of available binding sites for dye molecules. The layered structure of ZnAl LDH provided an interlayer space that can accommodate the anionic dye by anion exchange mechanisms. Partial exfoliation observed at higher SPI loadings increased the exposure of interlayer sites which can facilitate the exchange of interlayer carbonate or hydroxyl ions with dye's sulfonate groups ($-SO_3^-$). This exchange further enhances the dye uptake by providing additional binding sites beyond surface interactions [31,32]. Such partial exfoliation also reduced diffusion resistance allowing dye molecules to access both surface and interlayer regions more efficiently. The pH-dependent studies revealed that electrostatic attractions played a dominant role in the adsorption process at acidic pH. Under these conditions, LDH surface becomes positively charged due to protonation of surface hydroxyl groups which enhanced its interaction with the negatively charged sulfonate groups. This electrostatic complementarity facilitates initial adsorption and molecular orientation at the solid–liquid interface [81]. Simultaneously, protonation of SPI functional groups under acidic conditions contributed to an overall increase in positive surface charge further reinforcing electrostatic attraction toward anionic dye species.

D–R isotherm model was employed to describe the nature of adsorption process, revealing a Gaussian distribution of energy over a heterogeneous surface. The calculated mean free energy ($E<8$ kJ/mol) suggests that physisorption is the predominant mechanism, rather than chemisorption. This is consistent with the involvement of non-covalent interactions such as hydrogen bonding, van der Waals forces, and π-interactions. Cationic–π interactions were proposed between the $Zn^{2+}/Al^{3+}$ ions in the LDH structure and the π-electron system of the aromatic rings in Tr. These interactions promote dye stabilization through non-covalent association, especially in biocomposites with extended conjugated systems. These cation–π interactions might further assist in anchoring dye molecules at the LDH surface, thereby

limiting desorption during subsequent treatment or regeneration cycles. Van der Waals forces contributed to the overall adsorption process, particularly in facilitating close contact between the adsorbent surface and the planar aromatic regions of the dye molecules. These weak yet cumulative forces played a critical role in the stabilization of adsorbed species. Multiple factors such as hydrogen bonding, electrostatic attraction, anion exchange, cation–π interactions, and van der Waals forces contributed the adsorption process via heterogeneous and multi-site interactions. These findings confirmed that dye was effectively adsorbed onto the SPI/Zn-Al LDH biocomposite through a synergistic interplay of multiple interactions. The presence of SPI not only enhances surface functionality but also improves structural stability of the LDH under acidic conditions, thereby accounting for the high adsorption efficiency, pH responsiveness, and favorable regeneration behavior of the biocomposites [46,82].

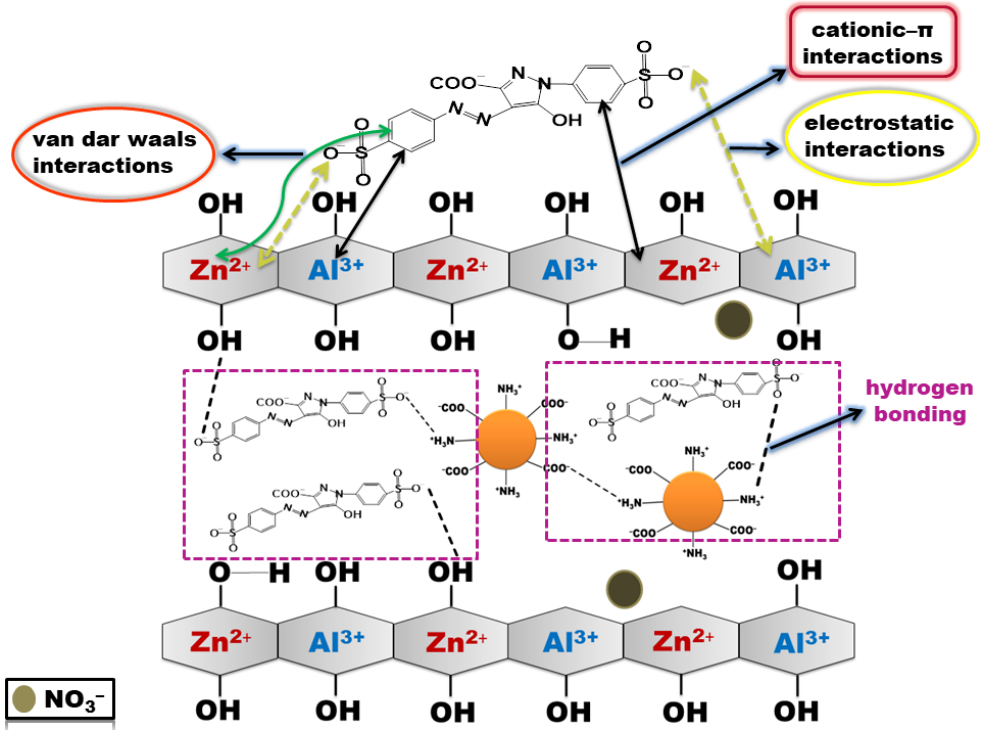


**Scheme 4.3** Proposed mechanism for adsorption of tartrazine dye on SPI/ZnAl LDH biocomposites

### 4.3.6 Practical application of prepared SPI/ZnAl LDH biocomposite

The removal of dye from both food products and food dye contaminated wastewater was evaluated using the adsorption capability of the 2:1 SPI/ZnAl LDH biocomposite under dark conditions. In separate test tubes, 5 mg of the biocomposite was dispersed in 10 mL of each food sample solution and wastewater with pH adjusted to 2 using 0.1 M $H_2SO_4$. The initial

concentrations of dye in wastewater, custard powder, yellow candy and mountain dew were 22 mg/L, 21 mg/L, 20 mg/L, and 12 mg/L. The samples were stirred at 250 for 60 minutes to facilitate adsorption. Following agitation, the mixtures were centrifuged at 9000 rcf (g) for 12 min to remove absorbent from the solutions.

The UV-Visible spectra for food samples were shown in **Fig. 4.16(a–c)**. After one hour, the adsorption percentage on 2:1 biocomposite was: Mountain Dew (81.43%) > yellow candy (79.21%) > custard powder (77.85%), as depicted in **Fig. 4.16d**. For food dye wastewater it achieved 75% adsorption in 1 hr **(Fig. 4.17)**. A slight decrease in removal percentage from food samples compared to commercial dye solution could be attributed to matrix effects along with the presence of interfering compounds and inherent competing ions in the complex food systems. Despite these minor variations, the considerable adsorption performance demonstrated by the biocomposite across both food samples and dye wastewater validated the effectiveness and applicability of this proposed method for real-world scenarios. These findings highlighted the practical potential of 2:1 SPI/ZnAl LDH biocomposite for efficient dye removal from complex effluents typical of the food industry.

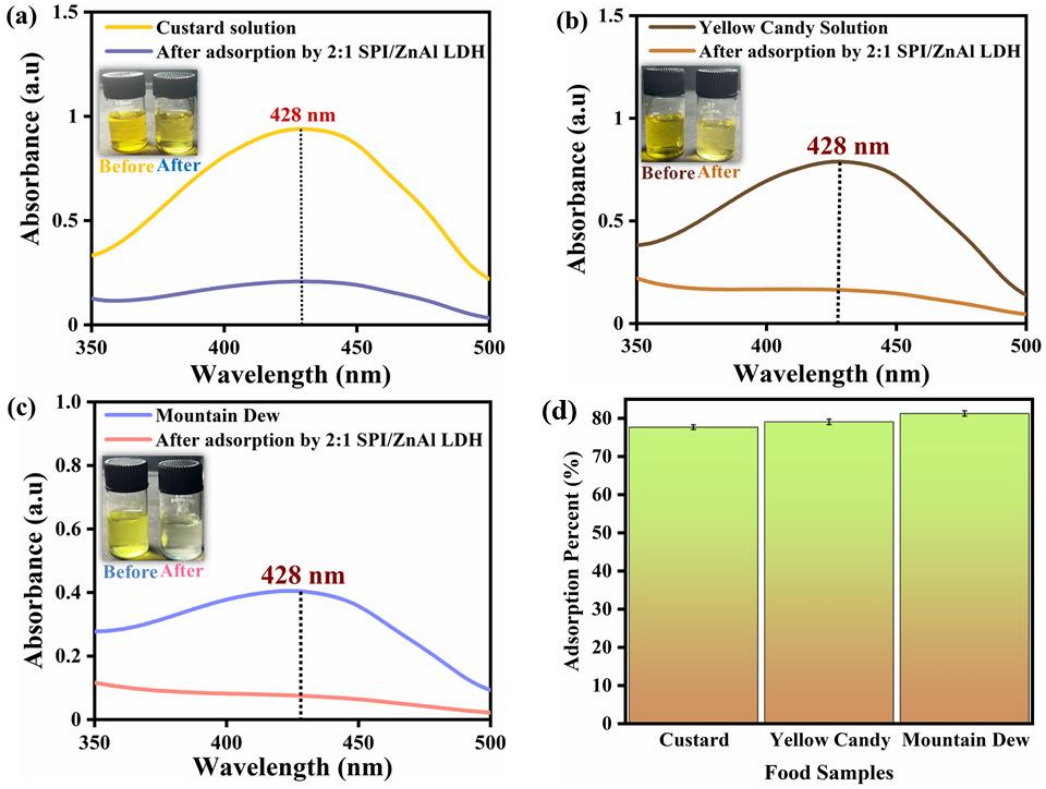


**Fig. 4.16 (a–c)** UV-visible spectra of food samples, and **(d)** Adsorption Percentage of tartrazine from custard, yellow candy and mountain dew on 2:1 SPI/ZnAl LDH biocomposite. Experimental conditions: pH = 2, initial concentration of tartrazine = 21 mg/L (custard), 20 mg/L (yellow candy), 12 mg/L

(mountain dew), 2:1 SPI/ZnAl LDH biocomposite dosage = 5 mg, contact time = 60 min and temperature = 30° ± 2° C

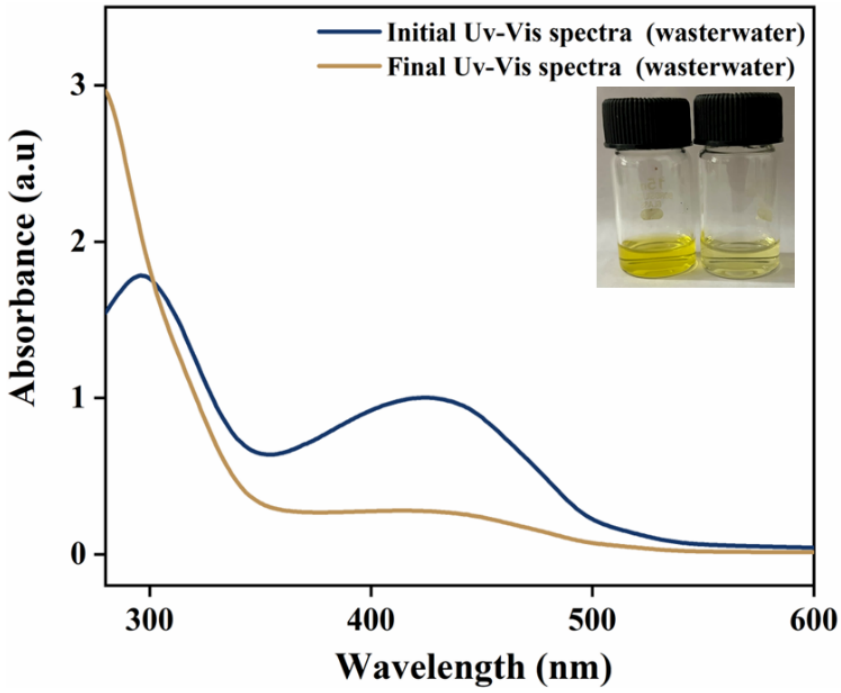


**Fig. 4.17** Uv-vis spectrum of food dye wastewater solution over 2:1 SPI/ZnAl LDH biocomposite across 60 min dark environment

### 4.3.7 Desorption and reusability test

Desorption experiments were conducted to evaluate the release of Tr dye from the 2:1 SPI/ZnAl LDH biocomposite using three different eluents: 0.1 M NaCl, $H_2SO_4$, and NaOH, as presented in **Fig. 4.18a**. NaOH achieved the highest desorption efficiency of (81.2%), followed by $H_2SO_4$ (37.1%) and NaCl (12.5%). It was likely due to increased negative charge density on the adsorbent surface under alkaline conditions which enhanced the electrostatic repulsion and promoted dye release. Influence of pH on desorption highlighted the reversibility of adsorption process which promotes adsorbent regeneration. Under alkaline conditions, the disruption of electrostatic and hydrogen bonding interactions between the dye and biocomposite facilitates dye's detachment.

The stability and recyclability of the biocomposite were assessed over five adsorption-desorption cycles using 0.1 M NaOH for desorption **(Fig. 4.18b)**. A desorption efficiency of ~82% was attained in the first cycle. Removal percent was maintained between 75% and 82% for three cycles. A slight decline to 73% was observed in the fourth cycle, after which the performance stabilized. This decrease could be due to gradual degradation of SPI polymer

chains by repeated acidic and alkaline treatments which affected the material's structural integrity and reduce the availability of active sites [83]. Overall, the biocomposite exhibited excellent regeneration capability and maintained substantial adsorption performance throughout multiple cycles. These results demonstrate the material's potential for effective dye removal applications in acidic environments alongside its ability to be efficiently regenerated making it suitable for commercial and industrial use. The gradual decline in adsorption capacity upon repeated use (~73 % retention by the fifth cycle) was mainly due to chemical swelling and partial hydrolysis of SPI rather than thermal effects. During adsorption and regeneration under ambient conditions, thermal stress was avoided and extended reuse was possible as pH-controlled regeneration methods were employed.

The structural integrity of 2:1 SPI/ZnAl LDH biocomposites was also evaluated to confirm this finding. **Fig. 4.18c** showed that the XRD spectra of recycled 2:1 SPI/ZnAl LDH biocomposites, both before as well as after five recycling experiments, demonstrated no change in peak positions, or overall crystallinity. This signified that the crystal structure of the biocomposite remained unaltered throughout adsorption-desorption process. This stability underscores the material's regeneration capacity. The consistent XRD pattern over cycles further corroborates the durability and efficacy of this material in real applications.

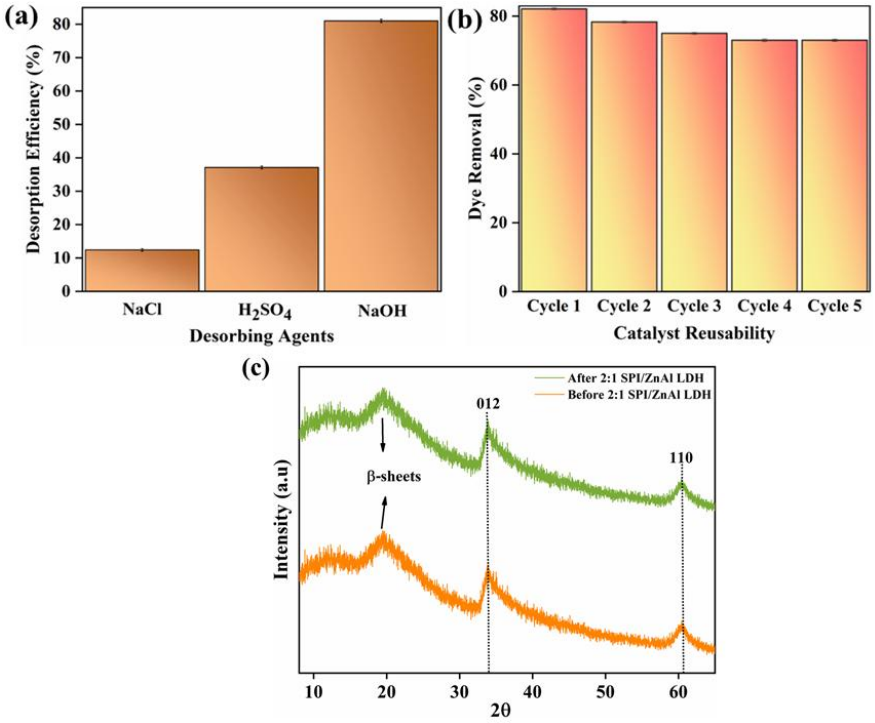


**Fig. 4.18 (a)** Desorption, and **(b)** 2:1 SPI/ZnAl LDH adsorbent reusability for dye adsorption, and **(c)** XRD spectra of before and after 2:1 SPI/ZnAl LDH biocomposite

### 4.3.8 Advantages and limitations of the SPI/ZnAl LDH biocomposite as an adsorbent

The SPI/ZnAl-LDH biocomposite exhibited several advantages as an adsorbent. The combination of SPI functional groups with positively charged LDH layers enabled synergistic adsorption via electrostatic attraction and hydrogen bonding, resulting in higher dye uptake than the individual components. The composite having improved LDH dispersion and stability due to the protein matrix effectively worked under acidic conditions suitable for food-dye-containing effluents. In addition, the hybrid material was biodegradable, food-compatible, regenerable, and also exhibited antibacterial activity, enhancing its applicability in water treatment. However, there were some limitations too. Adsorption efficiency was decreased at neutral to alkaline pH possibly due to weakened electrostatic interactions. Controlled $Zn^{2+}$ release, while beneficial for antibacterial action, might require monitoring to see contamination of other metals. As it was a protein-based material, the composite showed moderate mechanical and thermal stability, which could restrict long-term use in harsh or high-temperature environments.

## 4.4 Conclusion

This study reported the successful synthesis of a novel SPI/ZnAl-LDH biocomposite for efficient tartrazine removal. The hybrid material also showed antibacterial activity. Under optimized condition (pH 2.0, 60 min, 5 mg dosage), the 2:1 SPI/ZnAl-LDH achieved a high adsorption efficiency of ~99.85% showing a maximum capacity of 49.01 mg $g^{-1}$ with spontaneous physisorption behavior. The biocomposite demonstrated effective dye removal from real food products and wastewater (75–81%) and maintained ~73% adsorption efficiency even after five regeneration cycles using mild alkaline desorption process. Additionally, enhanced antibacterial activity against Listeria species and *Acinetobacter calcoaceticus* demonstrated its multifunctionality. In conclusion, the protein–LDH hybrid appeared to be a sustainable, regenerable, and eco-friendly material suitable with regard to food-safety aspects and wastewater treatments.

### References


1. Hussain S, Khan N, Gul S, Khan S (2020) By Food Dyes and Its Removal Technologies, Water Chemistry 113.
2. Dey S, Nagababu BH (2022) Applications of food color and bio-preservatives in the food and its Effect on the human health. Food Chem Adv 1:100019. https://doi.org/10.1016/-j.focha.2022.100019.

3. Greluk M, Hubicki Z (2011) Efficient Removal of Acid Orange 7 dye from water using the strongly basic anion exchange resin Amberlite IRA-95. Desalination 278:219. https://doi.org/10.1016-j.desal.2011.05.024.
4. Shankarling GS, Deshmukh PP, Joglekar AR (2017) Process intensification in azo dyes. J Environ Chem Eng 5:3302–3308. https://doi.org/10.1016/j.jece.2017.05.057.
5. Chequer FMD, Lizier TM, de Felicio R, Zanoni MVB, Debonsi HM, Lopes NP, Marcos R, de Oliveira DP (2011) Analyses of the genotoxic and mutagenic potential of the products formed after the biotransformation of the azo dye. Disperse Red Toxicol in Vitro 25:2054–2063. https://doi.org/10.1016/j.tiv.2011.05.033.
6. Atterbury RJ, Connerton PL, Dodd CE, Rees CE, Connerton IF (2003) Application of host-specific bacteriophages to the surface of chicken skin leads to a reduction in recovery of Campylobacter jejuni. Appl Environ Microbiol 69:6302–6306. https://doi.org/10.1128/AEM.69.10.6302-6306.2003.
7. Wu L, Xu Y, Lv X, Chang X, Ma X, Tian X, Shi X, Li X, Kong X (2021) Impacts of an azo food dye tartrazine uptake on intestinal barrier, oxidative stress, inflammatory response and intestinal microbiome in crucian carp (Carassius auratus) Ecotoxicol Environ Saf 223(112551):1–8. https://doi.org/10.1016/j.ecoenv.2021.112551.
8. Sahnoun S, Boutahala M (2018) Adsorption removal of tartrazine by chitosan/polyaniline composite: Kinetics and equilibrium studies. Inter J Biol Macromol 114:1345–1353. https://doi.org/10.1016/j.ijbiomac.2018.02.146.
9. Villabona-Ortiz A, Figueroa-Lopez KJ, Ortega-Toro R (2022) Kinetics and adsorption equilibrium in the removal of azo-anionic dyes by modified cellulose. Sustain 14:3640. https://doi.org/10.3390/-su14063640
10. Singh S, Arputharaj E, Dahms HU, AK Patel, YL Huang (2022) Chitosan-based nanocomposites for removal of Cr (VI) and synthetic food colorants from wastewater. Biores Technol 351:127018. https://doi.org/10.1016/j.biortech.2022.127018
11. Amaku JF, Taziwa R (2023) Thermodynamics, kinetics and isothermal studies of tartrazine adsorption onto microcline/MWCNTs nanocomposite and the regeneration potentials. Sci Rep 13(1):9872. https://doi.org/10.1038/s41598-023-37181-2
12. Balayeva OO, Azizov AA, Muradov MB, Alosmanov RM (2023) Removal of tartrazine, ponceau 4R and patent blue V hazardous food dyes from aqueous solutions with ZnAl-LDH/PVA nanocomposite. J Disp Sci Technol 44(7):1133-1146. https://doi.org/10.1080/01932691.2021.2006688
13. Shahveh S, Motakef-Kazemi N, Hallajian S (2024) Preparation and evaluation of alginate nanocomposite containing clay and zein to remove tartrazine dye from aqueous solution. J Theoretical Appl Phy 18(1). https://doi.org/10.57647/J.JTAP.2024.1801.06

14. Gomez M, Arancibia V, Rojas C, Nagles E (2012) Adsorptive stripping voltammetric determination of tartrazine and sunset yellow in gelatins and soft drink powder in the presence of cetylpyridinium bromide. Inter J Electrochem Sci 7:7493–502. https://doi.org/10.1016/S1452-3981(23)15799-3.
15. Hajimahmoodi M, Afsharimanesh M, Moghaddam G, Sadeghi N, Oveisi MR, Jannat B, Pirhadi E, Zamani MF, Kanan H (2013) Determination of eight synthetic dyes in foodstuffs by green liquid chromatography. Food Add Contam Part A 30(5):780–785. https://doi.org/10.1080/-19440049.2013.774465.
16. Tsai CF, Kuo CH, Shih DYC (2015) Determination of 20 synthetic dyes in chili powders and syrup-preserved fruits by liquid chromatography/tandem mass spectrometry. J Food Drug Anal 23:453–462. https://doi.org/10.1016/j.jfda.2014.09.003.
17. Yi J, Zeng L, Wu Q, Yang L, Xie T (2018) Sensitive simultaneous determination of synthetic food colorants in preserved fruit samples by capillary electrophoresis with contactless conductivity detection. Food Anal Methods 11:1608–1618. https://doi.org/10.1007/s12161-017-1141-6.
18. Crini G, Badot PM (2008) Application of Chitosan, a Natural Aminopolysaccharide, for Dye Removal from Aqueous Solutions by Adsorption Processes Using Batch Studies: A Review of Recent Literature. Prog Polym Sci 33:399. https://doi.org/10.1016/j.progpolymsci.2007.11.001.
19. Kandisa RV, Saibaba KVN, Shaik KB, Gopinath R (2016) Dye removal by adsorption: a review, J. Bioremed. Biodegrad. 7(6):1–4.
20. Meretoudi AD, Kalampogias I, Koumentakou I, Kalavrouziotis IK, Tolkou AK, Kyzas GZ (2025) Chitosan/montmorillonite/graphene oxide composites for the adsorption of dyes from single-component solutions, binary mixtures, and real textile wastewaters: on understanding the adsorption interactions. Langmuir 41(34):23198–23213. https://doi.org/10.1021/acs.langmuir.5c03148
21. Chaudhary G, Jasrotia A, Raj P, Kaur R, Kumari A, Rajput VD, Minkina T, Mandzhieva S, Kaur R (2023) Contamination of water and sediments of Harike wetland with phthalate esters and associated risk assessment. Water 15(6):1009. https://doi.org/10.3390/w15061009
22. Rzig B, Kojok R, Khalifa EB, Magnacca G, Lahssini T, Hamrouni B, Bellakhal N (2024) Adsorption performance of tartrazine dye from wastewater by raw and modified biomaterial: Equilibrium, isotherms, kinetics and regeneration studies. Biomass Conver Bioref 14(15):18313–18330. https://doi.org/10.1007/s13399-023-03982-8.
23. Rabeie B, Mahmoodi NM (2024) Green and environmentally friendly architecture of starch-based ternary magnetic biocomposite (Starch/MIL100/CoFe2O4): Synthesis and photocatalytic degradation of tetracycline and dye. Inter J Biol Macromol 274:133318. https://doi.org/10.1016/-j.ijbiomac.2024.133318
24. Rabeie B, Mahmood NM (2025) Green synthesis of biopolymer-driven dual functional carboxymethyl cellulose composite (CMC/MIL100 (Fe)/MIL88A (Al)) as a Z-scheme photocatalyst and an adsorbent for water pollutants. Inter J Biol Macromol 147358. https://doi.org/10.1016/j.ijbiomac.2025.147358

25. Rahman MM, Shaikh MAA, Yeasmin MS, Gafur MA, Hossain MI, Alam MA, Khan MS, Paul T, Quddus MS (2024) Simultaneous removal of $Ni^{2+}$ and Congo red from wastewater by crystalline nanocellulose-Modified coal bionanocomposites: Continuous adsorption study with mathematical modeling. Groundwater Sustain Develop 26:101244. https://doi.org/10.1016/j.gsd.2024.101244
26. Liu F, Yang Q, Tang Q, Peng Q, Chen Y, Huo Y, Huang Q, Zuo Q, Gao N, Chen L (2023) Adsorption of RhB dye on soy protein isolate-based double network spheres: compromise between the removal efficiency and the mechanical strength. Chem Eng Res Des 193:268–280. https://doi.org/10.1016/j.cherd.2023.03.039.
27. Qin Z, Mo L, Liao M, He H, Sun J (2019) Preparation and characterization of soy protein isolate-based nanocomposite films with cellulose nanofibers and nano-silica via silane grafting. Polym 11(11):1835. https://doi.org/10.3390/polym11111835
28. Luo LH, Zhang YF, Wang XM, Wan Y, Chang PR, Anderson DP, Chen Y (2010) Preparation, characterization, and in vitro and in vivo evaluation of cellulose/soy protein isolate composite sponges. J Biomater Appl 24(6):503-526. https://doi.org/10.1177/0885328208099337
29. G Mishra, B Dash, S Pandey (2018c) Layered double hydroxides: a brief review from fundamentals to application as evolving biomaterials. Appl Clay Sci 153:172–186. https://doi.org-/10.1016/j.clay.2017.12.021.
30. Rashed SH, Abd-Elhamid AI, Abdalkarim SYH, El-Sayed RH, El-Bardan AA, Soliman HMA (2022) Preparation and characterization of layered-double hydroxides decorated on graphene oxide for dye removal from aqueous solution. J Mater Res Technol 17:2782–2795. https://doi.org/10.1016/-j.jmrt.2022.02.040.
31. Nait-Merzoug A, Guellati O, Djaber S, Habib N, Harat A, El-Haskouri J, Begin D, Guerioune M (2021) Ni/Zn layered double hydroxide (LDH) micro/nanosystems and their azorubine adsorption performance. Appl Sci 11(19):8899. https://doi.org/10.3390/app11198899
32. J Lin, Y Zhang, Q Zhang, J Shang, F Deng (2021) Enhanced adsorption properties of organic ZnCr-LDH synthesized by soft template method for anionic dyes. Environ Sci Poll Res 28(35):48236–48252. https://doi.org/10.1007/s11356-021-14035-w
33. CC Revadekar, CB Godiya, BJ Park (2024) Novel soy protein isolate/sodium alginate-based functional aerogel for efficient uptake of organic dye from effluents. J Environ Manage 352:120011. https://doi.org/10.1016/j.jenvman.2023.120011
34. Olivera S, Hu C, Nagananda GS, Reddy N, Venkatesh K, Muralidhara HB (2019) Multipurpose composite for heavy metal sorption, antimicrobial, and antioxidant applications. Inter J Environ Sci Technol 16(4):2017-2030. https://doi.org/10.1007/s13762-018-1774-z
35. Bugatti V, Gorrasi G, Montanari F, Nocchetti M, Tammaro L, Vittoria V (2011) Modified layered double hydroxides in poly caprolactone as a tunable delivery system: in vitro release of antimicrobial benzoate derivatives. Appl Clay Sci 52:34–40. https://doi.org/10.1016/j.clay.2011.01.025.

36. Onaizi SA, Leong SSJ (2011) Tethering antimicrobial peptides: current status and potential challenges. Biotechnol Adv 29:67–74. https://doi.org/10.1016/j.biotechadv.2010.08.012.

37. Lan Y, Wang Y, Qi X, Cai E, Xiang Y, Ge X, Xu H, Chen X, Li Y, Shi Y, Shen J, Liao Z (2024) A modified hyaluronic acid hydrogel with strong bacterial capture and killing capabilities for drug-resistant bacteria-infected diabetic wound healing. Inter J Biol Macromol 279:135301. https://doi.org/10.1016/j.ijbiomac.2024.135301

38. Cheng S, Wang H, Pan X, Zhang C, Zhang K, Chen Z, Dong W, Qi X (2022) Dendritic hydrogels with robust inherent antibacterial properties for promoting bacteria-infected wound healing. ACS Appl Mater Inter 14(9):11144–11155. https://doi.org/10.1021/acsami.1c25014.

39. Sharma S, Das N, Pal B (2025) Biodegradable wheat gluten/nanoclay-based bionanocomposite films for assessing the potential as a packaging material. Bio Conv Bioref 1-18. https://doi.org/10.1007/-s13399-025-06846-5

40. Alahe AM, Liza SA, Raha RK, Abdulla-Al-Mamun M (2025) Protein-Based Polymeric Metal–Nanocomposite Derived From Egg Albumin: A Highly Effective Antimicrobial Agent Against Bacteria. Appl Organometal Chem 39(1):e7780. https://doi.org/10.1002/aoc.7780

41. Sitohy M, Al-Mohammadi AR, Osman A, Abdel-Shafi S, El-Gazzar N, Hamdi S, Ismail SH, Enan G (2021) Silver-protein nanocomposites as antimicrobial agents. Nanomater 11(11):3006. https://doi.org/10.3390/nano11113006

42. Boucif F, Bessaha F, Bendahma F, Bessaha G, Mahrez N, Sillanpaa M, Khelifa A (2025) Facile synthesis and modification of layered double hydroxides (LDH) for adsorption of Orange I and Acid Red 114 dyes from aqueous solution: Performance and mechanism study. Inorg Chem Comm 114673. https://doi.org/10.1016/j.inoche.2025.114673.

43. Dutta G, Borgohain X, Kalita B, Bharali P, Rashid MH (2025) Facile Synthesis of MgFe-Layered Double Hydroxides (LDHs) for Adsorptive Removal of Malachite Green Dye from Water Surf Inter 106930. https://doi.org/10.1016/j.surfin.2025.106930.

44. Senol ZM, Arslanoglu H, Keskin ZS, Mehmeti V, El Messaoudi N (2025) Biosorption of rhodamine B and sunset yellow dyes on cross-linked chitosan-alginate biocomposite beads: Experimental and theoretical studies. Inter J Biol Macromol 298:139264. https://doi.org/10.1016/-j.ijbiomac.2024.139264.

45. Devi K, Bharti S, Saini I, Shukla S, Kumar R (2025) Starch-functionalized graphene oxide-polyethyleneimine composite for the adsorption of methylene blue. J Mol Str 142468. https://doi.org/10.1016/j.molstruc.2025.142468.

46. Bansal M, Pal B (2023) Starch modified NiFe layered double hydroxide composites for better adsorption and photocatalytic Removal of reactive dye and piroxicam-20 drug. Environ Sci Pol Res 30(29):73825–73848. https://doi.org/10.1007/s11356-023-27592-z.

47. Carvalheira A, Silva J, Teixeira, P (2021) Acinetobacter spp. in food and drinking water–A review. Food Microbiol 95:103675. https://doi.org/10.1016/j.fm.2020.103675.

48. Thevenot D, Dernburg A, Vernozy-Rozand C (2006) An updated review of Listeria monocytogenes in the pork meat industry and its products. J Appl Microbiol 101(1):7–17. https://doi.org/10.1111/j.1365-2672.2006.02962.x.

49. Zeng X, Yang Z, Liu F, Long J, Feng Z, Fan M (2017) An in situ recovery method to prepare carbon-coated Zn–Al–hydrotalcite as the anode material for nickel–zinc secondary batteries. RSC Adv 7:44514–44522. https://doi.org/10.1039/C7RA08622A

50. Chen J, Chen X, Zhu Q, Chen F, Zhao X, Ao Q (2013) Determination of the domain structure of the 7S and 11S globulins from soy proteins by XRD and FTIR. J Sci Food Agri 93(7):1687–91. https://doi.org/10.1002/jsfa.5950.

51. Sahnoun S, Boutahala M (2018) Adsorption removal of tartrazine by chitosan/polyaniline composite: Kinetics and equilibrium studies. Inter J Biol Macromol 114:1345–1353. https://doi.org/10.1016/-j.ijbiomac.2018.02.146.

52. Tansaz S, Singh R, Cicha I, Boccaccini AR (2018) Soy protein-based composite hydrogels: physico-chemical characterization and in vitro cytocompatibility. Polym 10(10):1159. https://doi.org/10.3390/polym10101159

53. Liu X, Kang H, Wang Z, Zhang W, Li J, Zhang S (2017) Simultaneously toughening and strengthening soy protein isolate-based composites via carboxymethylated chitosan and halloysite nanotube hybridization. Mater 10(6):653. https://doi.org/10.3390/ma10060653

54. Sharma S, Das N, Pal B (2023) Preparation, characterization, and application of soy protein isolate/Mg–Al layered double hydroxide-based bionanocomposite films. Chem Pap 77(6):3265–3275. https://doi.org/10.1007/s11696-023-02702-w

55. R Ahmad, R Kumar (2010) Adsorptive Removal of congo red dye from aqueous solution using bael shell carbon. Appl Surf Sci 257(5):1628–1633, https://doi.org/10.1016/j.apsusc.2010.08.111.

56. S Xu, Z Han, R Wu, J Cheng, G Xu (2018) Correlating micro/meso pore evolution and chemical structure variation in a mild thermal treatment of a subbituminite. RSC Adv 8(18):9754-9761. https://doi.org/10.1039/C7RA13215H.

57. F Gomri, M Boutahala, H Zaghouane-Boudiaf, SA Korili, A Gil (2016) Removal of acid blue 80 from aqueous solutions by adsorption on chemical modified bentonites. Desalination Water Treat 57(54):26240–26249. https://doi.org/10.1080/19443994.2016.1162208.

58. S Sahnoun, M Boutahala, C Tiar, A Kahoul (2018) Adsorption of tartrazine from an aqueous solution by octadecyltrimethylammonium bromide-modified bentonite: Kinetics and isotherm modeling, Comptes Rendus Chimie 21(3–4):391–398. https://doi.org/10.1016/j.crci.2018.01.008.

59. Silva Neto LD, Anchieta CG, Duarte JL, Meili L, Freire JT (2021) Effect of drying on the fabrication of MgAl layered double hydroxides. ACS omega 6(33):21819-21829. https://doi.org/10.1021/-acsomega.1c03581

60. Zubair M, Jarrah N, Khalid A, Manzar MS, Kazeem TS, Al-Harthi MA (2018) Starch-NiFe-layered double hydroxide composites: efficient Removal of methyl orange from aqueous phase. J Mol Liq 249:254–264. https://doi.org/10.1016/j.molliq.2017.11.022.
61. Tang CH, Choi SM, Ma CY (2007) Study of thermal properties and heat-induced denaturation and aggregation of soy proteins by modulated differential scanning calorimetry. Inter J Biol Macromol 40(2):96-104. https://doi.org/10.1016/j.ijbiomac.2006.06.013
62. Sawasdee S, Watcharabundit P (2019) Adsorption of Fe (II) solution by sugarcane bagasse and activated carbon prepared from sugarcane bagasse. https://doi.org/10.12982/CMUJNS.2019.0015
63. Yang F, Sun S, Chen X, Chan g Y, Zha F, Lei Z (2016) Mg -Al layere d double hydroxides modified clay adsorbents for efficient Removal of $Pb^{2+}$, $Cu^{2+}$ and $Ni^{2+}$ from water. Appl Clay Sci 123:134–14. https://doi.org/10.1016/j.clay.2016.01.026.
64. Mosaffa E, Banerjee A, Ghafuri H (2023) Sustainable high-efficiency removal of cationic and anionic dyes using new super adsorbent biochar: performance, isotherm, kinetic and thermodynamic evaluation. Environmental Science: Water Res Technol 9(10):2643-2663.
65. Tan X, Liu S, Liu Y, Gu Y, Zeng G, Cai X, Yan Z, Yang C, Hu X, Chen B (2016) One-pot synthesis of carbon supported calcined-Mg/Al layered double hydroxides for antibiotic removal by slow pyrolysis of biomass waste. Sci Rep 6(1):39691. https://doi.org/10.1038/srep39691.
66. Ahmad A, Rafatullah M, Sulaiman O, Ibrahim MH, Hashim R (2009) Scavenging behaviour of meranti sawdust in the Removal of methylene blue from aqueous solution. J Hazard Mater 170(1):357–365.https://doi.org/10.1016/j.jhazmat.2009.04.087.
67. Abugu HO, Ikwelle CE, Odewole OA, Lawal A, Olaleye AM, Ucheana IA, Okenwa JC, Egbueri JC (2025) Thermal and chemical pretreatment of Ebenaeae Diospyros preusii seed for enhanced adsorptive removal of aqueous-bound Cr (VI). Discover Water 5(1):2.
68. Banerjee S, Chattopadhyaya MC (2017) Adsorption characteristics for the Removal of a toxic dye, tartrazine from aqueous solutions by a low cost agricultural byproduct Arab J Chem 10:S1629–S163. https://doi.org/10.1016/j.arabjc.2013.06.005
69. Mittal A, Mittal J, Kurup L (2006) Adsorption isotherms, kinetics and column operations for the removal of hazardous dye, Tartrazine from aqueous solutions using waste materials—Bottom Ash and De-Oiled Soya, as adsorbents. J Hazard Mater 136(3):567–578. https://doi.org/10.1016-/j.jhazmat.2005.12.037.
70. Ansari R, Banimahd Keivani M, Fallah Delavar A (2011) Application of polyaniline nanolayer composite for removal of tartrazine dye from aqueous solutions. J Polym Res 18:1931–1939. https://doi.org/10.1007/s10965-011-9600-z.
71. Goscianska J, Pietrzak R (2015) Removal of tartrazine from aqueous solution by carbon nanotubes decorated with silver nanoparticles. Catal Today 249:259–264. https://doi.org-/10.1016/j.cattod.2014.11.017.

72. Grover A, Mohiuddin I, Malik AK, Aulakh JS, Vikrant K, Kim KH, Brown RJ (2022) Magnesium/aluminum layered double hydroxides intercalated with starch for effective adsorptive removal of anionic dyes. J Hazard Mater 424:127454
73. Ouassif H, Moujahid EM, Lahkale R, Sadik R, Bouragba FZ, Sabbar EM, Diouri M (2020) Zinc Aluminum layered double hydroxide: high efficient removal by adsorption of tartrazine dye from aqueous solution. Surfaces Interfaces 18:100401.
74. Mohamed Nasser S, Abbas M, Trari M (2024) Understanding the rate-limiting step adsorption kinetics onto biomaterials for mechanism adsorption control. Prog React Kinetic Mech 49:14686783241226858.
75. Fetter G, Velazquez-Herrera FD (2025) Intrinsic antimicrobial properties of LDH clays: a brief review. Emergent Mater 1–16.
76. Huang Z, Zheng X, Yan D, Yin G, Liao X, Kang Y, Yao Y, Huang D, Hao B (2008) Toxicological effect of ZnO nanoparticles based on bacteria, Langmuir 24:4140–4144. https://doi.org/-10.1021/la7035949.
77. Malachova K, vPraus P, Rybkova Z, Kozak O (2011) Antibacterial and antifungal activities of silver, copper and zinc montmorillonites. Appl Clay Sci 53:642–645. https://doi.org/-10.1016/j.clay.2011.05.016.
78. Vasconcellos FCS, Woiciechowski AL, Soccol VT, Mantovani D, Soccol CR (2014) Antimicrobial and antioxidant properties of-conglycinin and glycinin from soy protein isolate, Inter J Current Microbiol Appl Sci 3(8):144e157.
79. Matsuzaki K (2009) Control of cell selectivity of antimicrobial peptides. BBA Biomembr 1788(8):1687–1692, https://doi.org/10.1016/j.bbamem.2008.09.013
80. Shafqat SS, Zafar B, Masood SA, Shafqat SR, Khan HU, Syed A, Bahkali AH, Mutahi S, Khan MA, Xu G, Zafar MN (2024) Nitrophenylfurfural grafted amino functionalized silica nanoparticles for adsorptive removal of tartrazine dye from water. Mater Adv 5(18):7296-7311. https://doi.org/10.1039/D4MA00618F
81. H Starukh, S Levytska (2019) The simultaneous anionic and cationic dyes removal with ZnAl layered double hydroxides. Appl Clay Sci 180:105183. https://doi.org/10.1016/j.clay.2019.105183.
82. Ihsanullah I, Bilal M, Jamal A (2022) Recent developments in the Removal of dyes from water by starch-based adsorbents. Chem Rec 22(7). https://doi.org/10.1002/tcr.202100312.
83. Bhaumik M, McCrindle RI, Maity A, Agarwal S, Gupta VK (2016) Polyaniline nanofibers as highly effective re-usable adsorbent for Removal of reactive black 5 from aqueous solutions. J Colloid Inter Sci 466:442–451.https://doi.org/10.1016/j.jcis.2015.12.056.

# Conclusion and Future Aspects

This thesis demonstrated the development of protein-based bionanocomposites with applications in sustainable packaging and environmental remediation. Three systems, namely SPI/Mg–Al LDH, WG–C30B, and SPI/ZnAl LDH, were successfully synthesized using solution casting and co-precipitation methods and comprehensively characterized to establish their structural, thermal, mechanical, antimicrobial, biodegradation, and adsorption behaviour. The SPI/Mg–Al LDH films showed improved thermal resistance and maintained acceptable mechanical performance at moderate LDH incorporation. Structural analyses confirmed intercalation and partial exfoliation of LDH within the SPI matrix, whereas higher filler loading resulted in particle aggregation and a decline in tensile strength. The developed films also exhibited biodegradation under natural conditions. WG–C30B BNC films demonstrated improved thermal stability, enhanced tensile strength, lower water sensitivity, and antibacterial activity. Among the prepared formulations, 10% (w/w) C30B loading provided the most balanced performance and was effective in extending the shelf life of green grapes under storage conditions while retaining biodegradability. SPI/ZnAl LDH biocomposite exhibited high adsorption efficiency for tartrazine under optimized conditions, followed adsorption isotherm and kinetic models, and maintained appreciable performance during regeneration cycles. In addition, antibacterial activity and successful dye removal from commercial samples highlighted its multifunctional applicability for wastewater treatment.

Overall, the study established that controlled integration of proteins with LDH and nanoclay fillers can improve targeted functional properties while preserving sustainability attributes. These findings support the potential of protein-based bionanocomposites as alternatives for selected packaging and adsorption applications. Nevertheless, further studies on migration behaviour, cytotoxicity, long-term stability, and scale-up feasibility are required before industrial implementation.

# List of Publications

1. **Shreya Sharma**, Niranjan Das, Bonamali Pal **(2023)**, "Preparation, characterization, and application of soy protein isolate/Mg–Al layered double hydroxide-based bionanocomposite films", **Chemical Papers**, 77 (6), 3265–3275. **(IF = 2.5)** https://doi.org/10.1007/s11696-023-02702-w.

2. **Shreya Sharma**, Niranjan Das, Bonamali Pal **(2025)**, "Biodegradable Wheat Gluten/Nanoclay-based Bionanocomposite Films for Assessing the Potential as a Packaging Material", **Biomass Conversion and Biorefinery**, 15, 25045–25062 **(IF = 4.1)** https://doi.org/10.1007/s13399-025-06846-5.

3. **Shreya Sharma**, Niranjan Das, Bonamali Pal **(2026)**, "Zn-Al layered double hydroxide-soy protein isolate biocomposite exhibits superior adsorption of tartrazine food dye and antimicrobial properties", **Microporous and Mesoporous Materials**, 404, 114055 **(IF = 4.7)**. https://doi.org/10.1016/j.micromeso.2026.114055

# Conferences

1. **Second-Best Oral Presentation Award** in the Thematic Area of Biomanufacturing in BIO3 conference organized by the Department of Biotechnology, TIET, Patiala (20-22$^{nd}$ March 2025).
2. **Poster presentation** at 24$^{th}$ National Symposium on Catalysis (CSCME-2025) organized by the Department of Chemistry and Biochemistry, TIET, Patiala (24-26$^{th}$ February 2025).
3. **Paper presentation** at "International Conference on Multidisciplinary Approaches to Chemical Sciences" organized by the Department of Chemistry National PG College Lucknow (24-26$^{th}$ October 2024)
4. **Paper presentation** at 26$^{th}$ Punjab Science Congress-2023 National Conference on "Environement Food Security and Health with Reference to Climate Change". Organized by: Shri Guru Granth Sahib World University Fategarh Sahib, Punjab.

Chemical Papers (2023) 77:3265–3275
https://doi.org/10.1007/s11696-023-02702-w

ORIGINAL PAPER

# Preparation, characterization, and application of soy protein isolate/Mg–Al layered double hydroxide-based bionanocomposite films

Shreya Sharma[1] · Niranjan Das[2] · Bonamali Pal[1]

Received: 3 October 2022 / Accepted: 25 January 2023 / Published online: 10 February 2023


## Abstract

Soy protein isolate has received much attention in recent decades due to its abundance, eco-friendliness, low cost, film-forming capacity, and processability. In this study, novel soy protein isolate (SPI)-based bionanocomposite films were prepared by integrating Mg–Allayered double hydroxide (LDH) at different loadings (0%, 2%, 5%, and 9% w/w) using a simple solution casting process. The Mg–Al LDH was synthesized in a 2:1 molar ratio via a co-precipitation method. Fourier transform infrared spectroscopy (FTIR), X-ray diffraction (XRD), field-emission scanning electron microscopy, and thermogravimetric analysis (TGA) revealed intercalation/exfoliation of Mg–Al LDH sheets in the SPI matrix of bionanocomposite films. Agglomeration of Mg–Al LDH was distinctly noticed as its concentration increased from 0 to 9% (w/w). The bionanocomposite films showed considerable thermal stability. Mechanical and biodegradation qualities were also investigated. The tensile strength values of the prepared films with 0%, 2%, 5%, and 9% w/w LDH loadings were found to be $2.12 \pm 0.25$, $1.60 \pm 0.15$, $1.64 \pm 0.08$ and $1.58 \pm 0.06$ KNm/g, respectively. The SPI-Mg/Al LDH 5% film showed a substantial increase in tensile strength and efficiently degraded in non-sterile soil.

**Keywords** Soy protein isolate · Layered double hydroxide · Bionanocomposite films · Thermal stability · Biodegradability · Mg–Al

## Introduction

Bionanocomposites (BNCs) are rapidly emerging as eco-friendly bioplastics during the recent decades in order to minimize hydrocarbon-based plastic wastes. BNCs are also referred to as 'biocomposites', 'green composites', and 'biohybrids' as these are derived from renewable bioresources. Bionanocomposites are regarded as the new generation nanocomposites (NCs). Basically, BNCs are a group of nanostructured hybrid materials developed mainly by the applied aspects of nano, material and life sciences (Ozin and Arsenault 2015). Biopolymers such as starch materials along with other homo and heteropolysaccharides, proteins, chitosan, lipids are being frequently used in making various bioplastics which potentially offer a better and cost-effective solution for both packaging and waste disposal. Biopolymer-based materials are significantly gaining importance due to their biodegradability, and compatibility with the pharmaceuticals, processed food products and diverse agricultural produce (Shameli et al. 2011). As reported in the literature, bio-based packaging materials find multiple applications with regard to containment, food safety, maintaining sensory quality, and displaying product details for consumers. A number of different proteins having distinct biochemical properties namely serum albumin, egg white, collagen, gelatin, myofibrils, casein, whey protein, wheat gluten, corn zein and some other proteins from plant sources such as soybean, sesame, peanut, cottonseed, sunflower and rice bran were used in preparing the BNCs as potential film-forming materials (Hua et al. 2005; Ojijo and Ray 2013).

Proteins are linear hetero-biopolymers, and extremely diverse with regard to three dimensional (3-D) structures and biological activities. The presence of different functional groups in the constituent amino acid residues of the individual polypeptide chains can form bonds at different positions

✉ Bonamali Pal
bpal@thapar.edu

[1] School of Chemistry and Biochemistry, Thapar Institute of Engineering and Technology, Patiala, Punjab 147004, India

[2] Department of Biotechnology, Thapar Institute of Engineering and Technology, Patiala, Punjab 147004, India

Biomass Conversion and Biorefinery
https://doi.org/10.1007/s13399-025-06846-5

ORIGINAL ARTICLE

# Biodegradable wheat gluten/nanoclay-based bionanocomposite films for assessing the potential as a packaging material

**Shreya Sharma**[1] · **Niranjan Das**[2] · **Bonamali Pal**[1]

Received: 10 January 2025 / Revised: 29 March 2025 / Accepted: 6 April 2025


## Abstract

Preparation and characterization of biopolymer-based packaging materials have significantly gained importance because of sustainability, biodegradability, and eco-friendly nature. In this study, novel wheat gluten (WG)/cloisite 30B (C30B) organoclay–based bionanocomposite (BNC) films were prepared by solution casting method at various C30B concentrations (5%, 10%, and 15%). X-ray diffraction and field emission scanning electron microscopy revealed intercalation/exfoliation of C30B sheets into the WG matrix. WG-C30B 10% film was thermostable. It showed low surface roughness along with higher water barrier properties and surface hydrophobicity. The tensile strength values of WG and WG-C30B 10% films were found to be $0.7 \pm 0.02$ and $1.11 \pm 0.01$, respectively, indicating improvement in mechanical properties. WG-C30B 10% film demonstrated antibacterial activity against both *Staphylococcus aureus* and *Salmonella enterica*. Shelf life of green grapes was monitored under different conditions: 4 °C, ambient conditions, and 42 °C. WG-C30B 10% film proved effective in extending shelf life up to 18 days under ambient conditions. More than 50% of the bionanocomposite films were degraded in agricultural soil within 2 weeks, while completely degraded in sewage sludge soil after a few days. WG-C30B 10% film appeared to be promising regarding the demonstrated physico-chemical and antibacterial properties. This report would be useful in preparing biodegradable biopolymer-based packaging materials.

**Keywords** Bionanocomposite films · Water sensitivity · Thermal stability · Antibacterial activity · Shelf-life extension · Biodegradability

## 1 Introduction

Currently, the development of biopolymer-based packaging materials has become an emerging trend in bionanotechnology. Potentially, they could serve as viable alternatives to petroleum-based, non-biodegradable materials due to their biodegradability and eco-friendly nature. For example, effective and safe packaging materials remain crucial in food processing industries for safety, stability, quality, and overall shelf life of food products. Proper packaging can protect them from damages due to physical, chemical, and biological changes during transportation, distribution, and storage. Conventionally, several synthetic polymers like polylactic acid, polybutylene succinate, and polyvinyl chloride were used in developing packaging materials [1]. Biodegradable packaging materials with antimicrobial properties are gaining importance as they could prevent spoilage of food products due to pathogenic microbes [2–6]. Among various biopolymers, proteins are relatively more preferred nowadays because of their characteristic physico-chemical properties [7]. Various physical, chemical, and enzymatic treatments are possible due to their amphiphilic nature, electrostatic charges, and conformational changes like partial/complete unfolding which were exploited in making various coatings/films [8, 9].

Gluten is a storage protein found in the endosperm of wheat, rye, and barley grains. Wheat gluten is widely available, having a protein content of more than 75%. Gliadin and glutenin are the major components of gluten that influence the physico-chemical characteristics of cereal-based food products. Gliadins are soluble in aqueous 70% alcohol whereas glutenin remains insoluble primarily in common solvents because of its size and complex

✉ Bonamali Pal
bpal@thapar.edu

[1] Department of Chemistry and Biochemistry, Thapar Institute of Engineering & Technology, Patiala 147004, Punjab, India

[2] Department of Biotechnology, Thapar Institute of Engineering & Technology, Patiala 147004, Punjab, India

Published online: 15 April 2025

Microporous and Mesoporous Materials 404 (2026) 114055

Contents lists available at ScienceDirect

Microporous and Mesoporous Materials

journal homepage: www.elsevier.com/locate/micromeso

# Zn-Al layered double hydroxide-soy protein isolate biocomposite exhibits superior adsorption of tartrazine food dye and antimicrobial properties

Shreya Sharma [a], Niranjan Das [b], Bonamali Pal [a,*]

[a] Department of Chemistry and Biochemistry, India
[b] Department of Biotechnology, Thapar Institute of Engineering and Technology, Patiala, 147004, Punjab, India

ARTICLE INFO

*Keywords:*
Antibacterial activity
Dye adsorption
Food products

ABSTRACT

A novel soy protein isolate (SPI)/ZnAl layered double hydroxide (LDH) biocomposite was developed as an efficient and sustainable adsorbent for the removal of azo food dye tartrazine from aqueous systems and commercial food products. The biocomposite was synthesized via a simple co-precipitation method and characterized to confirm successful integration of SPI with LDH, resulting in a functional, porous hybrid material. The optimized SPI/ZnAl LDH composition exhibited rapid and highly efficient dye adsorption under acidic conditions, driven by electrostatic interactions, hydrogen bonding, and interlayer anion exchange. Adsorption behavior followed both Langmuir and Freundlich isotherm models, indicating favorable and spontaneous dye uptake dominated by physisorption. The biocomposite demonstrated effective dye removal from real food matrices and food dye wastewater, highlighting its practical applicability. In addition, the material showed notable antibacterial activity against both Gram-positive and Gram-negative bacteria and retained good adsorption performance over multiple regeneration cycles. These results establish SPI/ZnAl LDH biocomposites as promising eco-friendly materials for simultaneous dye removal and antimicrobial applications in food safety and wastewater treatment.

List of abbreviations

| | |
|---|---|
| LDH | Layered double hydroxides |
| SPI | Soy protein isolate |
| Tr | Tartrazine |
| FDs | Food dyes |
| LB | Luria Broth |
| LA | Luria-Agar |
| XRD | X rays diffraction |
| FTIR | Fourier transform infrared spectroscopy |
| SEM | Scanning electron microscopy |
| TGA | Thermogravimetric analysis |
| BET | Brunauer-Emmett-Teller analysis |
| PZC | Point of zero charge |
| ZnAl LDH | Zinc Aluminium layered double hydroxide |
| SPI/ZnAl LDH | Soy protein isolate/zinc aluminium layered double hydroxide |
| $H_2SO_4$ | Sulphuric acid |
| NaOH | Sodium hydroxide |
| $\lambda_{max}$ | Maximum absorption wavelength |
| $C_0$ | Initial concentration |
| $C_e$ | Concentration at equilibrium |
| V | Volume |
| W | Weight |
| $q_{max}$ | Maximum adsorption capacity |
| $K_L$ | Langmuir constant |
| $K_f$ | Freundlich constant |
| $R_L$ | Dimensionless constant |
| D−R | Dubinin Raushkevich isotherm model |
| B | D−R activity constant |
| $\varepsilon$ | Polanyi potential |
| E | Mean free adsorption energy |
| A | Temkin equilibrium binding constant |
| B | Heat of adsorption constant |
| $\Delta G$ | Gibbs free energy |
| R | Gas constant |
| T | Absolute temperature |
| k | Equilibrium constant |
| $q_t$ | adsorption capacity at time t |
| $q_e$ | adsorption capacity at equilibrium |
| $C_t$ | Concentration at time t |
| PSO | Pseudo second order model |
| IPD | Intraparticle diffusion |
| $K_2$ | Pseudo second order rate constant |
| α | Initial rate constant |
| β | Desorption process constant |
| $K_{di}$ | Intraparticle rate constant |
| $C_i$ | Resistance to diffusion constant |

* Corresponding author. Thapar Institute of Engineering and Technology, Patiala, 147004, India.
*E-mail address:* bpal@thapar.edu (B. Pal).

https://doi.org/10.1016/j.micromeso.2026.114055
Received 19 October 2025; Received in revised form 13 January 2026; Accepted 27 January 2026
Available online 29 January 2026

thesis plag

ORIGINALITY REPORT

| 15% | % | 15% | % |
|---|---|---|---|
| SIMILARITY INDEX | INTERNET SOURCES | PUBLICATIONS | STUDENT PAPERS |

PRIMARY SOURCES

| | | |
|---|---|---|
| 1 | "Polymers for Food Applications", Springer Science and Business Media LLC, 2018<br>Publication | <1% |
| 2 | Manjushree Nagaraj Gunaki, Saraswati P. Masti, Oshin Jacintha D'souza, Manjunath P. Eelager et al. "Fabrication of CuO nanoparticles embedded novel chitosan/hydroxypropyl cellulose bio-nanocomposites for active packaging of jamun fruit", Food Hydrocolloids, 2024<br>Publication | <1% |
| 3 | Mahmoud H. Abu Elella, Nema Aamer, Heba M. Abdallah, Eduardo A. López-Maldonado et al. "Novel high-efficient adsorbent based on modified gelatin/montmorillonite nanocomposite for removal of malachite green dye", Scientific Reports, 2024<br>Publication | <1% |
| 4 | Roy, Abhinandan Singha. "Development of Sustainable Slow Release Fertilizers Based on Layered Double Hydroxides for Soil Conditioning", University of Johannesburg (South Africa), 2025<br>Publication | <1% |
| 5 | "Advances in Nanocomposite Materials for Environmental and Energy Harvesting Applications", Springer Science and Business Media LLC, 2022<br>Publication | <1% |